STUDIES ON DC PLANAR MAGNETRON GLOW DISCHARGE PLASMA

A THESIS

SUBMITTED TO GAUHATI UNIVERSITY FOR THE DEGREE OF DOCTOR OF PHILOSOPHY IN PHYSICS IN THE FACULTY OF SCIENCE

SUBMITTED BY

PARTHA SAIKIA

2014

Dedicated
to
my parents

DECLARATION BY THE CANDIDATE

I hereby declare that the thesis entitled **“Studies on DC planar magnetron glow discharge plasma”** is my own work conducted under the supervision of **Dr. Bipul Kumar Saikia** (supervisor).

I further declare that to the best of my knowledge the thesis does not contain any part of any work which has been submitted for the award of any degree either in this University or any other University/Deemed University without proper citation.

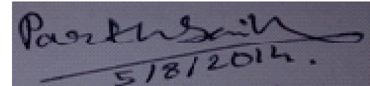

(Partha Saikia)

Centre of Plasma Physics
Institute for Plasma Research
Nazirakhat-782402
Sonapur, Kamrup (M)
Assam

CERTIFICATE BY SUPERVISOR

This is to certify that the work entitled "**Studies on DC planar magnetron glow discharge plasma"**is a piece of research work done by Mr. Partha Saikia under my guidance and supervision for the degree of Doctor of Philosophy in Physics of Gauhati University.

To the best of my knowledge and belief the thesis:

1. embodies the work of the candidate himself;

2. fulfills all the requirements prescribed under the rules and regulations of Gauhati University.

3. has incorporated , if any, suggestions/recommendations made at the pre-submission seminar.

4. is up to the standard both in respect of contents and language for being referred to the examiner.

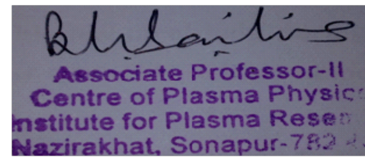

Date: 05/08/2014

Place: Guwahati

(Signature of the supervisor)

Dr. B. K. Saikia

Associate Prof. II

Centre of Plasma Physics
Institute for Plasma Research
Nazirakhat-782402
Sonapur, Kamrup (M)
Assam

ACKNOWLEDGEMENT

First of all, I would like to express my gratitude to Dr. B. K. Saikia for his guidance to complete this thesis work. I have enjoyed an atmosphere of complete freedom to imagine and carry out the experiments under his supervision.

I would also like to thank Prof. K. S. Goswami for his keen interest in my work and critical response to various topics that helped me to develop better understanding of the subject.

I am thankful to my parents and my two brothers for their constant support and encouragement during the tenure of my PhD work.

The critical evaluation provided by the Academic committee of CPP-IPR certainly helped me to shape my PhD work and I express my thanks to Dr. B. J. Saikia, Dr. M. Kakati, Dr. S. R. Mohanti, Dr. T. K. Borthakur and Dr. M. Chakravborty for their valuable suggestions.

Throughout my stay at CPP-IPR, I have received helped from a number of people from various section of CPP-IPR. I thank Mr. N. Kathar for his technical help during various stages of my experiments and the administrative stuff of CPP-IPR, which helped me in procuring the experimental components.

My tenure at CPP-IPR have been memorable for which I owe my gratitude to my seniors Kaushik Da, Neog Da, Pranjal Sir, Arindam Da, Minal Da, Biswa Da, Hemen Da, Manas Da, and Kamal Da. I have enjoyed the company of my friend Bharat Da, Bidyut Da, Amoa, Nayan, Mousumi, Basanti, Rakesh, Akshay, Angshuman, Nayan-jyoti a lot for the whole duration of my stay at the hostel. The weekend's parties at the hostel revitalized me and provided the necessary fuel to carry out work with more energy. I have learnt a lot from them. During the later part of my PhD years, arrival of my juniors Trinayan, Nilanjan,

Neelam, Narayan, Sayan, Sudamoni, Deiji, Porismita, Annanya and Achyana have made it a truly wonderful experience at CPP-IPR.

I would also like to thanks my friends outside CPP-IPR Campus specially Arundhoti, Arnab, Subrat, Sunny who all encouraged me at various stages of my life.

The helped received from Alphonsa Madam and Rane Sir in FCIPT for the XRD characterization of some samples and the valuable advices of Dr. S. Mukherjee is highly appreciated.

I owe a lot to Swapna for the fruitful discussions, and the rigorous proof reading of the thesis.

Partha

ABSTRACT

The direct-current (DC) planar magnetron glow discharge plasma is widely used to deposit thin films of different conducting metals. The studies on DC planar magnetron glow discharge plasma are aimed to understand the modulation of plasma parameters as a function of thin film deposition conditions. To optimize the quality growth of the deposited thin film, knowledge of the plasma parameters of the magnetron set-up is very essential. The anomalous behavior of plasma parameters in unbalanced DC magnetron discharge is still a topic of for many researchers. In reactive sputtering in addition to the sputtering gas (generally argon) reactive molecular gas such as nitrogen, oxygen etc are added. The complex discharge behavior of the molecular gases and the complexities generated by the various plasma species in reactive sputtering makes the basic study of physical mechanism of the discharge much more challenging for the researchers. Study of such multi-component magnetron discharge is undoubtedly a subject for investigation. Many important results of the magnetron discharge have been achieved from the Langmuir probe study. However, as the magnetron discharge plasma contains sputtered material species also, the tip of the probe used to get coated by material deposition and thus, can lead to erroneous results.

In this regard, other diagnostic tools such as ion acoustic wave diagnostic, laser-induced fluorescence could be used to probe magnetron discharge. As the plasma parameters solely influence the growth of deposited thin film in magnetron sputtering, a good control over the properties of the thin film could be achieved if one can correlates the measured plasma parameters with its growth. Taking all this facts into consideration, the thesis attempts to address the following interesting concerns regarding the plasma and the material aspects.

1. The effect of addition of the molecular gases such as hydrogen, oxygen and nitrogen on the modulation of the plasma parameters that eventually determines the sputtering performance of the discharge.

2. As the planar target of the magnetron is used as the cathode of the deposition set-up and plays the important role in sustaining the discharge, therefore, its influence on the bulk plasma parameters of the magnetron discharge.

3. Correlating the plasma parameters with the growth (orientation) of the depositing coatings (titanium nitride).

4. Probing magnetron discharge plasma with novel diagnostics like ion acoustic wave (IAW).

5. A theoretical investigation of the propagation of the non-linear ion acoustic wave in DC magnetron discharge.

The Chapter 1 of the thesis deals with the basic introduction to the magnetron discharge plasma, its characteristics, application in different fields and importance of the study of the plasma parameters of the magnetron discharge. This chapter also contains a detailed literature survey of magnetron discharge, in material as well as the plasma aspects.

In this thesis, the design and the fabrication of the experimental set-up as well as the characterization of the system in terms of the plasma and deposition parameters are described in the Chapter 2. Various plasma diagnostic tools like the Langmuir probe, Optical emission spectroscopy (OES), and ion acoustic wave have been employed to study the magnetron discharge. Chapter 2 also contains details about the mentioned diagnostics tools.

The ion induced secondary electron coefficient (ISEE) of the target determines the plasma parameters of the magnetron discharge. The ISEE coefficients affect on the plasma parameters are achieved by mounting the magnetron with different targets (Cr and Cu) and scanning the magnetron discharge plasma with the above mentioned diagnostics and is explained in the Chapter 3 of the thesis.

Ion acoustic wave as an alternative to the Langmuir probe diagnostics are excited in the substrate vicinity of the magnetron set-up and the precise determination of the plasma parameters such as the relative ion concentration is obtained from the measured phase velocity of the propagating wave and it is explained in the Chapter 4.

In the molecular gas (hydrogen and nitrogen) addition to argon discharge experiments, the effect of two most important experimental parameters: working pressure and input power are addressed respectively partly in the Chapter 3 and Chapter 5.

The coatings of titanium nitrides are deposited on bare as well as plasma nitrided high speed steel and are characterized using X-ray diffraction study to evaluate the structural properties (columnar orientation). The orientation of the deposited coatings is correlated with the plasma parameters of reactive gas added argon plasma partly in the Chapter 5 and Chapter 6.

During the course of the IAW excitation experiment to determine relative ion density of ions, it turns out that the excited wave transform into a soliton as it propagates in argon magnetron discharge. But, a little amount of hydrogen addition to argon magnetron discharge can inhibit its formation. This affect has been explained in details using Sagdeevs pseudo potential method in the Chapter 7.

Chapter 8 contains the conclusion of the thesis. All the major results obtained during the experimental investigations done in the present research work are briefly discussed and some scopes for future studies are outlined.

Some of the novel observations from the study are,

1. Higher ISEE coefficient value of Cr target compared to Cu target is responsible for the enhanced density of electron and ions in the bulk region of the magnetron discharge.

2. With addition of molecular gases like hydrogen and nitrogen, a gradual decrease of electron and ion density is noticed and it affects the deposition rate on the substrate.

3. Working pressure influences the degree of ion bombardment during the growth of the TiN thin film on bare AISI M2 high speed steel. The growth of TiN film expressed as texture coefficient of the diffraction plane tends to orient towards more open direction with increase of working pressure.

4. Along with the working pressure, the nature of the substrate also plays an important role in the texture growth of TiN film.

5. The relative concentration of negative ions in oxygen added argon plasma is probed with ion acoustic wave and it shows an increasing trend with gradual addition of oxygen. The measurements of ion acoustic wave are benchmarked with the Langmuir probe analysis and it shows good correspondence.

6. The introduction of the light ions such as hydrogen-related ions ($H^{+,}$ H_2^+, H_3^+) decreases the amplitude of the ion acoustic solitary wave in hydrogen added argon magnetron plasma. Using Sagdeevs pseudo-potential method, the properties of soliton are studied as a function of hydrogen addition in argon magnetron discharge.

List of Publications in Refereed Journal

1) Study on the effect of target on plasma parameters of magnetron sputtering discharge plasma, **P. Saikia,** B. Kakati, and B. K. Saikia, **Phys. Plasmas. 20,** 103505 (2013); doi: 10.1063/1.4825235.

2) Theoretical investigation of the effect of hydrogen addition on the formation and properties of soliton in direct current argon plasma**,** **P. Saikia,** K. S. Goswami, and B. K. Saikia, **Phys. plasmas. 21,** 033501 (2014); doi: 10. 1063/1.4867182.

3) Argon-oxygen DC magnetron discharge plasma probed with ion acoustic waves, **P. Saikia,** B. K. Saikia, K. S. Goswami, and A. Phukan, **J. Vac. Sci. Technol**. **A 32**, 031303 (2014); doi: 10.1116/1.4871081.

4) P. Saikia, and B. Kakati, J. Vac. Sci. Technol. **31,** 061307 (2013), Erratum: "Effect of process parameters on properties of argon–nitrogen plasma for titanium nitride film deposition, **P. Saikia,** B. Kakati, and B. K. Saikia, J. Vac. Sci. Technol. **A 32,** 043401 (2014) doi: http://dx.doi.org/10.1116/1.4884595.

5) Role of substrate and deposition conditions on the texture evolution of titanium nitride thin film on bare and plasma-nitrided high-speed steel**, P. Saikia,** A. Joseph, R. Rane, B. K. Saikia and S. Mukherjee, **Journal of Theoretical and Applied Physics 7,** 66 (2013); doi:10.1186/2251-7235-7-66.

List of Publication in Conference Proceedings

1) The effect of substrate biasing on the growth of TiN thin film on pre-nitrided AISI M2 high speed steel, **P. Saikia,** A. Joseph, R. Rane, B. K. Saikia and S. Mukherjee, PLASMA-2012 (27th PSSI annual national symposium) 10-13 December, 2012.

Presentations in conference and symposiums

1. The effect of substrate biasing on the growth of TiN thin film on pre-nitrided AISI M2 high speed steel, **P. Saikia,** A. Joseph, R. Rane, B. K. Saikia and S. Mukherjee, 27th National Symposium on PLASMA SCIENCE AND TECHNOLOGY, “PLASMA2012”, Department of Physics, Pondicherry University, Puducherry.

2. Probing argon-hydrogen magnetron discharge plasma with ion acoustic wave, **P. Saikia**, and B. K. Saikia. 28th National Symposium on PLASMA SCIENCE AND TECHNOLOGY, “PLASMA2013”, Department of Physics, K. I. I. T, Bhubaneswar.

3. The structural and mechanical properties of TiN thin film deposited on plasma nitrided substrate, P. Saikia and B. K. Saikia, UGC Sponsored National Seminar on “ Plasma Science and Techonology”, Department of Physics, Nabajyoti College, Kalgachia, 2013.

Content

Page number

Declaration
Certificate from Guide
Acknowledgements
Abstract
List of Publications
Content

CHAPTER 1
Introduction
1.1 Physical Vapor Deposition: An Introduction…………………………….. 1
1.2 Different Physical vapor deposition treatments…………………………... 2
1.2.1 Evaporation Method ……………………………………………….. 2
1.2.2 Sputtering …………………….. 3
1.2 3 Reactive Sputtering………………………………………………... 6
1.2.3(a) Hysteresis effect in Reactive Sputtering………………….. 7
1.2.3(b) Model of Reactive Sputtering……………………………... 8
1.3 Different sputter deposition techniques………………………………….. 10
1.3.1 Ion Beam Sputtering (IBD)………………………………………… 10
1.3.2 Ion Beam Assisted Deposition (IAD)……………………………… 10
1.3.3 Gas Flow Sputtering (GFS)…………………….......................... 11
1.3.4 Magnetron Sputtering…………………….................................. 11
1.4 DC Planar Magnetron Sputtering………………………………………… 12
1.4.1 Design and working principle……………………………………… 13
1.4.2 Types of Planar magnetron………………………………………… 15
1.4.3 Qualitative model of DC Planar magnetron sputtering……………. 17
1.4.3(a) Ring width (w).. 17
1.4.3(b) The Sheath thickness (s) …………………………………... 18
1.4.3(c) Electric field (E) through the sheath ……………………..…... 19
1.5 Low pressure plasma………………………….......................... 20
1.6 The Cathode sheath………………………………………………………. 22
1.7 Duplex Process: An introduction……………………………………….. 24
1.8 Motivation of the Thesis …………………………………………………. 25
1.9 Review of the previous works…………………………………………… 28

1.9.1 The effect of the targets on the properties of the magnetron………. discharge 28
1.9.2 The use of the plasma diagnostics in the magnetron discharge…….. 31
1.9.3 Study of plasma properties as a function of the input parameters….. 32
1.9.4 The effect of the substrate on the orientation of the deposited film... 34
1.9.5 Theoretical study on the propagation of ion acoustic soliton in low temperature plasma………………………………………………………. 36
1.10 Summary of chapters………………………………………………… 36
1.11 Scope of the Thesis…………………………………………………….. 40
References………………………………………………………………… 40

CHAPTER 2

Experimental set up

2.1 Basic consideration for magnetron operation…..…………………........... 47
2.1.1 Choosing the sputtering gas……………………………………… 47
2.1.2 Choosing the pressure range…………………………………...... 48
2.1.3 Choosing the electrical conditions for the glow discharge…………. 49
2.2 DC planar magnetron set up …………………………………………... 50
2.2.1 Vacuum chamber and accessories……………………………….. 51
2.2.2 The planar magnetron and substrates……………………………. 53
2.2.3 Calculating the pumping speed and flow rate of gas flow controller. 55
2.3 Plasma diagnostic tools and techniques………………………………. 56
2.3.1 Langmuir probe……………………………………………………….. 56
2.3.1(a) The electron saturation current…………………………….. 59
2.3.1(b) The ion saturation current…………………………………. 59
2.3.1(c) Floating potential…………………………………………….. 60
2.3.1(d) Mean ion mass (M_i) and ion density measurement in……. multi-component plasma 60
2.3.2 Ion acoustic wave (IAW) diagnostic……………………………….. 62
2.3.1(a) Method of wave excitation………………………………… 62
2.3.1(b) The Wave-launcher……………………………………... 64
2.3.3 Optical emission spectroscopy (OES) …………………………….. 66
2.3.4 Experimental set-up for optical emission intensity measurement…. 67
2.3.5 Measurement of deposition rate: Quartz Crystal Thickness Monitor. 68
2.4 Initial plasma characterization experiments………………………………
2.4.1 I/V characteristics acquired at various operating conditions………. 69

2.4.2 Measurement of optical emission line intensity…………………… 72
2.5 Plasma nitriding experimental set-up…………………………………….. 75
2.6 Summary…………………………………………………………………. 78
References……………………………………………………………………… 78

CHAPTER 3
Study on the effect of target on the plasma parameters of hydrogen added argon DC planar magnetron plasma

3.1 Introduction………………………………………………………………... 82
3.2 Experimental set up and diagnostic procedure…………………………… 84
3.3 Results and discussions…………………………………………………... 85
3.3.1 Variation of secondary electron density in the ring region………… of the magnetron discharge 85
3.3.2 Description of ionic processes in H_2 containing argon plasma……... 87
3.3.3 Plasma parameters as a function of working pressure……………… 89
3.3.3(a) Langmuir probe measurement……………………………… 89
3.3.3(b) Optical emission spectroscopy study………………………. 95
3.4 Influence of target material on V-I characteristics of magnetron……….. discharge 98
3.5 Hydrogen effect on the film deposition rate……………………………… 100
3.6 Conclusion……………………………………………………………….. 101
References……………………………………………………………………. 102

CHAPTER 4
Probing magnetron discharge plasma with ion acoustic wave

4.1 Introduction……………………………………………………………. 105
4.2 Experimental set up and diagnostic procedure…………………………… 107
4.3 Theory of ion acoustic wave in multi-component plasma……………….. 109
4.4 Description of ionic processes in oxygen containing argon plasma……… 112
4.5 Results and discussions…………………………………………………... 116
4.5.1 Measurement of the relative concentration of ion using ion………. acoustic wave diagnostics 116
4.5.2 Langmuir probe and optical emission spectroscopy measurement… 119
4.6 Conclusion……………………………………………………………….. 125
References…………………………………………………………………… 126

CHAPTER 5

Effect of process parameters on the properties of argon–nitrogen plasma for titanium nitride film deposition

5.1 Introduction………………………………………………………………. 129

5.2 Experimental set-up and diagnostic procedure…………………………… 131

5.3 Description of ionic processes in the N_2 containing argon plasma……….. 132

5.4 Results and Discussions…………………………………………………... 133

5.4.1 Langmuir probe study……………………………………………… 133

5.4.2 Optical emission spectroscopy study………………………………. 136

5.4.3 Effect of discharge conditions on the V-I characteristic of magnetron discharge……….. 139

5.4.4 XRD analysis of the deposited thin films…………………………..... 140

5.5 Conclusion……………………………………………………………….... 142

References……………………………………………………………………. 143

CHAPTER 6

Role of the substrate on the growth of titanium nitride thin film

6.1 Introduction………………………………………………………………. 145

6.2 Experimental set up and diagnostic procedure…………………………… 146

6.3 Results and discussions…………………………………………………... 148

6.3.1 Langmuir probe study of the magnetron plasma…………………… 148

6.3.2 XRD studies of the plasma nitrided AISI M2 high speed steel……. 149

6.3.3 XRD studies of the deposited titanium nitride thin films…………... 150

6.3.4 Effect of substrate on the texture growth of the TiN films…………. 153

6.4 Conclusion……………………………………………………………….. 154

References……………………………………………………………………. 155

CHAPTER 7

Theoretical investigation of the ion acoustic soliton in hydrogen added argon plasma

7.1 Introduction……………………………………………………………… 157

7.2 Theoretical formulation………………………………………………….. 159

7.3 Numerical results and discussions……………………………………….. 168

7.3.1 Parametric Variation…………………………………………………... 168

7.3.2 Width variation and potential profile……………………………….. 173

7.4 Conclusion……………………………………………………………….. 175

References……………………………………………………………………. 176

CHAPTER 8

Summary and Future Scope

8.1 Summary of the Investigation……………………………………………. 178

8.2 Future scopes……………………………………………………………….. 181

Chapter 1

Introduction

The modification of physical, chemical or optical properties to suit industrial functions is the basis of material processing techniques. In many material processing techniques, the modification is done on the surface of the material as it acts as the interface with the external environment. The process of depositing thin layer of different materials on the surface to obtain specific material properties is known as surface coating. Physical vapor deposition (PVD) and Chemical vapor deposition (CVD) are widely used methods for depositing coatings. This chapter contains discussions on various PVD processes with emphasis given on surface coating by magnetron sputtering device.

1.1 Physical vapor deposition: An introduction

Physical vapor deposition processes are atomistic deposition process in which the material is vaporized from solid or liquid source in the form of atoms or molecules, transported in the form of a vapor through a low pressure gaseous (or plasma) environment to the substrate where it condenses [1]. Ion implantation, vacuum evaporation and sputter deposition are various forms of PVD processes. All of these PVD processes are conducted in a vacuum or low pressure gaseous environment [1]. Low pressure environment ensures the control and minimization of contaminants in a given system as well as provides a long mean free path between original source of material and the location upon which the particles are deposited.

PVD processes are often credited with capable of coating anything on anything. Some of the advantages [2] of the PVD based deposition techniques are

1. High deposition rates

2. Ease of sputtering any metal, alloy or compound

3. High-purity films

4. Extremely high adhesion of films

5. Excellent coverage of steps and small features

6. Ability to coat heat-sensitive substrates

7. Ease of automation

8. Excellent uniformity on large-area substrates

1.2 Different Physical vapor deposition treatments

Various Physical vapor deposition processes have been developed to match the requirement of industrial applications regarding thin film coatings. In the followings, an overview of these processes is given.

1.2.1 Evaporation method

Evaporation method is the simplest way to coat substrate with another material. Due to the simplicity in its application, this method is widely used upon its introduction. The underlying principle of this method is to evaporate the material in the vicinity of the substrate and it is the basis for various techniques like Thermal evaporation, Electron beam evaporation and Cathodic arc evaporation. In thermal evaporation, low melting materials are heated to the point of evaporation directly or by ohmically heated containers in low pressure. The low pressure ensures the long mean free path for the evaporated atoms such that they can transit to the substrate without being scattered by ambient gas molecules. In Electron beam evaporation, a directed electron beam is used to cause localized melting of the material and the evaporated material leave in the same direction as the incident electron

beam. This method is particularly suitable for evaporation of high melting point material. Cathodic arc evaporation utilizes an electric arc to generate a localized region of extremely high temperature. The target material is vaporized as a result, and material is ejected as high velocity jet. It is then deposited at the substrate. However lack of uniformity and inability to deposit over large area substrate is the common drawback of such deposition process.

1.2.2 Sputtering

Sputtering is a process whereby atoms of a solid target (in vaporized form) are ejected due to the momentum transfer from an atomic-sized energetic bombarding particle impinging on the target surface [3]. Typically gaseous ions (inert gases like argon, xenon etc.) from plasma are accelerated and directed towards the target in sputtering. The accelerated ions can therefore displace the target atoms either through direct collisions or can induce a 'collision cascade' resulting in emission of atoms. **Fig. 1.1** represents the process of ion bombardment on the target surface. Various experimental [4] and simulation [5] studies have been conducted to explain the physical nature of sputtering. For example, the TRIM.SP [4] is a well known simulation code used to calculate the sputtering of various materials. These vaporized particles will then condense upon and coat a substrate material.

In the energy range most relevant to sputter deposition, the interaction between the impinging ion and the target surface are sufficiently short range in nature and as such, can be treated as a series of binary collisions between them. A binary collision is characterized by the energy transfer function and is given by [6]

$$E_{transferred} = \frac{4m_i m_t}{(m_i + m_t)^2} \tag{1.1}$$

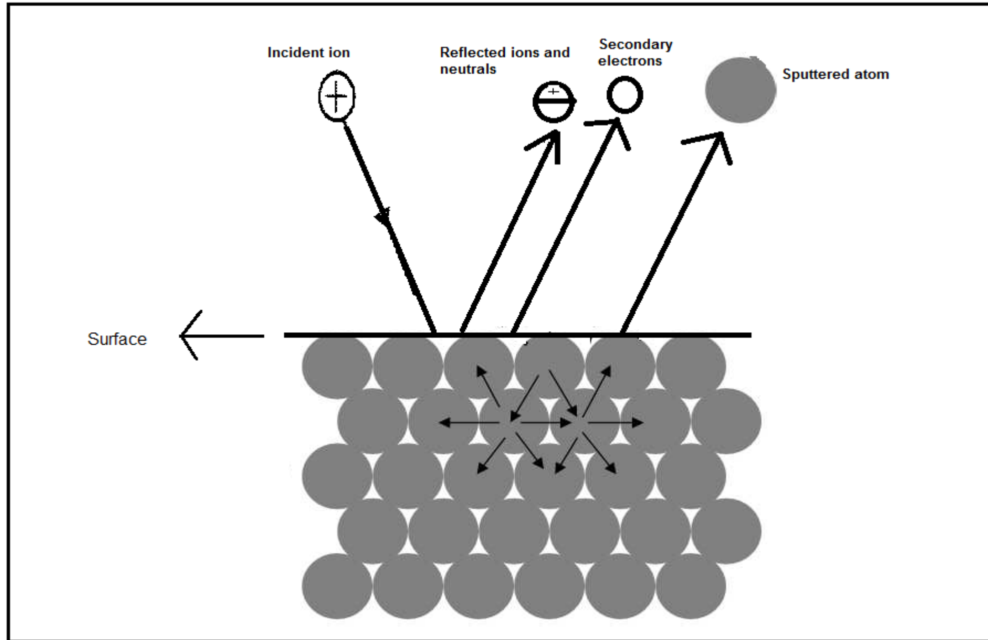

Figure 1.1 Interaction of the incident ions with surface. Other than sputtering of the target atoms, associated processes which may happen due to ion interaction with the material surface are secondary electron emission, reflection of the incident particles etc.

where m_i and m_t are the mass of the incident and target atoms. This shows that incident atoms need to have at least comparable mass as the target atoms for effective energy transfer. Another useful parameter is the Sputtering yield (Λ_{sput}) defined as the number of target atoms (or molecules) ejected per incident ion. Since the sputtered atoms can come only from the surface layers of the target, we would therefore expect the sputtering yield (Λ_{sput}) to be proportional to the energy available in the vicinity of the target surface and this is determined by the nuclear stopping power [7]. For low bombardment of energies up to 1 keV, the sputtering yield is given as [6]

$$\Lambda_{sput} = \frac{3\alpha}{4\pi^2} \frac{4m_i m_t}{(m_i + m_t)^2} \frac{E}{U_o} \qquad (1.2)$$

where, U_o is the surface binding energy of the material being sputtered and α is a monotonically increasing function of $\frac{m_t}{m_i}$. The expression of Λ_{sput} predicts that the sputtering yield should increase linearly with E which is a case up to energy 1 keV and above which, Λ_{sput} becomes relatively constant. At very high energies Λ_{sput} even decreases as ion implantation becomes dominant. Above 1 keV, a modified sputtering yield expression is given by [6],

$$\Lambda_{sput} = 3.56\alpha \frac{Z_i Z_t}{Z_i^{2/3} + Z_t^{2/3}} \frac{m_i}{m_i + m_t} \frac{\Lambda_{sputn}(E)}{U_o} \tag{1.3}$$

where, $\Lambda_{sputn}(E)$ is the reduced stopping power and is a function of the reduced energy based on the actual energy, Z_i and Z_t are the atomic numbers of the incident and target atom (molecules).The angular distribution of sputtered flux from the target for the cascade regime under normal ion incidence has a cosine like features and can be given as [8],

$$\Phi(E,\phi).dE.d\Omega = C.\cos\phi.\frac{1-\sqrt{\frac{U_s - E}{\Gamma E_i}}}{E^2(1+U_s/E)^3} dE.d\Omega \tag{1.4}$$

where ϕ is the ejection angle, E is the energy of the sputtered flux and Γ is the energy transfer factor and for elastic collision

$$\Gamma = \frac{4M_1 M_2}{(M_1 + M_2)^2} \tag{1.5}$$

The constant C depends on the combination of incident ions and the target material, mainly on atomic density, mass and inter-atomic potential and ion influx. For normal ejection,

$$\Phi(E,\phi) = C\frac{1-\sqrt{\dfrac{U_s - E}{\Gamma E_i}}}{E^2(1+U_s/E)^3} \tag{1.6}$$

In sputter deposition of the thin film, the sputtered atoms striking the substrate with these energies can produce some mixing and diffusion between the incoming atoms and the substrate materials leading to enhanced bonding and adhesion. Assuming all the sputtered material is deposited on the substrate, the deposition rate for physical sputtering is [8],

$$D_{sput} = \Lambda_{sput}\frac{\Gamma_i A_t}{n_f A_s} cm/s \tag{1.7}$$

where Γ_i is the incident flux ($cm^{-2}s^{-1}$), n_f is the density of the deposited film (cm^{-3}), A_t is the target area sputtered (cm^2), A_s is the substrate area on which film is deposited (cm^2) and Λ_{sput} is the sputtering yield.

1.2.3 Reactive Sputtering

In addition to the bombarding ions (from non reactive gases), if a feedstock gas whose dissociation products chemically reacts with the target is present in the sputtering process, then it is known as 'Reactive Sputtering'[9]. The deposited film is a compound formed from the sputtered target materials and reactive gas. It is widely used to deposit dielectrics such as oxides and nitrides as well as carbides and silicides. Common reactive gases used for a wide variety of application are O_2 and H_2O for O atoms, N_2 and NH_3 for N atoms, CH_4 and C_2H_2 for C atoms and SiH_4 for Si atoms. In reactive sputtering, chemical reactions occur at both the target and the substrate, in addition to the sputtering of the target and deposition at the substrate. There are two modes of operation for reactive sputtering of metal target to deposit a compound film. For low bombarding ion flux and high reactive gas

flux, the target is covered by the compound. For high bombarding ion flux and low reactive gas flux, the target remains metallic. Higher deposition rates are achieved in the 'metallic mode' than in the 'covered/compound mode' for mainly of two reasons. As the compounds have higher secondary electron coefficients than metals, most of the energy of the incident ions is utilized in breaking bonds with the resultant creation and acceleration of the secondary ions. The other reason is that the sputtering yield of metal atoms from a compound on the target is less than from the pure metallic target. In reactive sputtering, if the flow of reactive gas is varied, the non linear and complex nature of sputtering process can be easily observed. A very well known and important non linear feature of reactive sputtering is the hysteresis effect.

1.2.3 (a) Hysteresis effect in Reactive Sputtering

If at a constant partial pressure of non reactive bombarding gas and sputtering power, the flow rate of the reactive gas is varied, a hysteresis curve (**Fig. 1.2**) of the reactive gas partial pressure (P_r) as a function of the reactive gas flow rate (f_r) is obtained [10]. At low values of f_r, almost all the available reactive gas is gettered at condensation sites and no essential change in P_r is observed from the background level and the deposited film is metal rich. This situation prevails up to a critical point P_{r_1} [up to a point B in **Fig. 1.2(a)**]. If we further increase f_r, the flow rate of reactive gas into the chamber becomes higher than the getting rate of the sputtered metal. The reactive gas then reacts with the target surface to form a layer of gas metal compound. As the sputtering rate is less in 'compound mode', less reactive gas is consumed in the reaction and a sudden and sharp rise in reactive gas partial pressure to a new value P_{r_2} occurs [Point C in **Fig. 1.2(a)**].

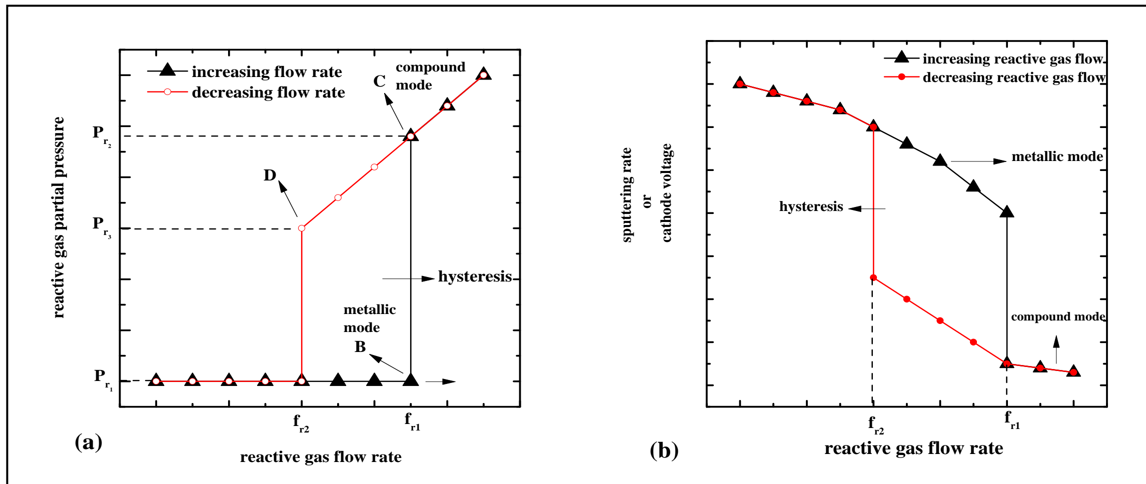

Figure 1.2 Hysteresis effect in reactive sputtering

The deposited film is then gas rich. It is then followed by linear increase in P_r with f_r. However if f_r is reduced, P_r will not decrease following the same trajectory as it is increased. With further decrease of the reactive gas flow rate, the reactive gas pressure starts to decrease to background pressure [point D in **Fig. 1.2(a)**], thus forming a hysteresis. The dependence of the deposition rate and cathode voltage on the reactive gas flow rate shows the same sort of hysteresis effect [**Fig. 1.2(b)**]. When f_r is in the region of hysteresis, there lies a possibility of existence of two stable operating states corresponding to an individual value of f_r and therefore it is very likely to deposit compound film of different stoicheometries and physical properties even at a particular value of f_r. This effect is very undesirable and has to be eliminated for stable process operation. It is clear from the above discussion that for the deposition of stoicheometric compound thin film, the deposition should be performed in the 'compound mode'.

1.2.3 (b) Model of Reactive Sputtering

Berg et *al.* [11] had given a detail theoretical model of reactive sputtering (shown in **Fig.**

1.3). If the reactive gas flow introduced in the chamber is q_o we can divide it into three different gas flows: (i) the reactive gas flow to the target q_t (ii) the reactive gas flow to the substrate q_s and, (iii) the reactive gas flow to the pump q_p.

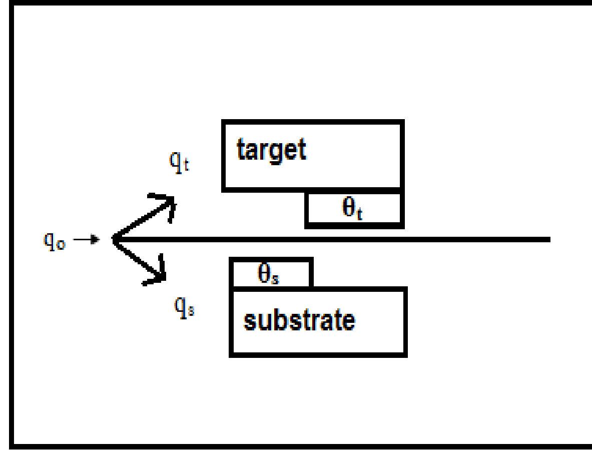

Figure 1.3 Overview of the Berg model for reactive sputtering

The total of these flows is equal to the reactive gas flow introduced in the chamber. The reactive gas molecules can form compound film on the substrate (and chamber walls), resulting in a given fraction θ_s of the substrate which has reacted. Let θ_t be the fractions of the target covered by the compound film and Λ_m and Λ_c are the yields for sputtering for the metal (1- θ_t) and the compound (θ_t) from the target. Let Γ_i and Γ_r be the incident sputtering ion and reactive gas molecules flux and let S_r be the sticking coefficient of a reactive molecule. With such definition, the target sputtering rate is

$$\Gamma_{sput} = \Gamma_i [\Lambda_m (1-\theta_t) + \Lambda_c \theta_t] \tag{1.8}$$

The total number of reactive gas molecules per second that are consumed to form the compound that are deposited on the substrate is,

$$\frac{dN_r}{dt} = \Gamma_r S_r [(1-\theta_t)A_t + (1-\theta_s)A_s] \tag{1.9}$$

where, A_t and A_s are the target and surface area. Once the compound coverage's θ_t and θ_s on the target as a function of the ion fluxes, rate constants and areas are known, $\frac{dN_r}{dt}$ and Γ_{sput} can be evaluated. The hysteresis behavior can be easily obtained once Γ_{sput} is plotted against $\frac{dN_r}{dt}$. As such, this model is helpful to understand the hysteresis and other related properties of the reactive sputtering deposition.

1.3. Different sputter deposition techniques

1.3.1. Ion Beam Sputtering (IBD)

Ion beam sputtering utilizes a Kaufman ion source [12]. The ions generated in the Kaufman ion source are accelerated by the electric field emanating from a grid toward a target. As the ions leave the source they are neutralized by electrons from a second external filament. Since the flux that strikes the target is composed of neutral atoms, either insulating or conducting targets can be sputtered. Materials sputtered from the target deposit on a nearby substrate to create a film. The advantage of IBD is the independent control over kinetic energy and current density of ions. Another advantage of this method is that there is no need for substrate heating. However, large amount of maintenance requirement to keep the ion source operating is the major drawback of this technique.

1.3.2. Ion Beam Assisted Deposition (IAD)

In IAD, the substrate is exposed to a secondary ion beam operating at lower power than ion gun. Generally a Kauffman source supplies secondary beam of energetic noble or reactive

ions at the surface of the growing film. The IAD is particularly desirable when growing metal oxides and metal nitrides films. Sputter deposition by IAD is highly directional and more energetic. In combination with a substrate fixture that rotates and changes angles, IAD sputtering can deliver a broad range of control over the sidewall coating.

1.3.3. Gas Flow Sputtering (GFS)

Gas flow sputtering utilizes a hollow cathode effect. A working gas like argon is led through an opening in a metal subjected to a negative electric potential. Enhanced plasma densities occur in a hollow cathode if pressure P and characterization length L of the hollow cathode obeys the condition $0.5 Pa.m < P.L < 5.0\ Pa.m$ where Pa is the unit of pressure and m is the unit of length. This causes high flux of ions on the surrounding surfaces and a large sputter effect. Usually the target is kept at a pressure of $1.33 \times 10^{2} Pa$. Under such high pressure condition, the sputtered atoms will lose their initial kinetic energy by collision with argon atom and become thermalized to the temperature of the surrounding gas in a very short distance. They are carried from the target to substrate by high speed argon flow from back of the sputtering target which also serves as the sputtering gas. As the effective deposition is due to the presence of argon gas flow, so the method is known as the gas flow sputtering (GFS). One of the main advantages of GFS is that it lowers the kinetic energy of the depositing atom and decreases damage to the growing film.

1.3.4 Magnetron Sputtering

The term magnetron generally refers to the device which utilizes crossed electric and magnetic field for particle confinement. Magnetron sputtering is a plasma based deposition method proven to be versatile technique for deposition of coatings used to modify the

functional properties of material like hardness, optical reflectivity etc. In magnetron sputtering permanent magnets are placed beneath the target which is used as the cathode. The magnetic lines of force enter and leave through the cathode plate. The role of the magnetic field is to trap the secondary electrons generated by the bombarding ions when very high voltage (~ 800V) is applied to the cathode. In general argon is used as the sputtering gas. The discharge appears in the form of a high density brightly glowing circular plasma ring of width w and mean radius R that hovers below the cathode. The ring is embedded by lower density bulk plasma. The sputtered atoms get condensed on the substrate and form thin film of the target material. Based on the target geometry and the magnetic field configuration, there exists many types of magnetron designs. In planar magnetron, the target used is in the shape of disc and the magnetic field configuration consists of central pole piece of magnet surrounded by annular ring of magnets of opposite polarity [13]. In cylindrical magnetron, the target is rod shaped and Helmholtz coil-type of arrangement is used to generate the magnetic field in a direction parallel to the target axis. The electric field is always kept perpendicular to the magnetic field and often extends radially out of the target [13]. For deposition over large area, rectangular planar magnetron is also used. Depending upon the type of target to be sputtered, different biasing can be applied to magnetron cathode. For sputter deposition of conducting target the DC bias is used and for sputter deposition of dielectric material the radio frequency (RF) biasing is applied.

1.4 DC planar magnetron sputtering

In a conventional sputtering source if a magnetic field parallel to the target surface is used, the efficiency of sputtering is increased [14]. It is due to the fact that by applying magnetic

field of suitable strength, the secondary electrons generated due to the bombardment of ions can be easily trapped. For secondary electrons of energy of a few tens of eV [15, 16], the magnetic field requires to confine the electrons in a radius of 0.5 mm can be calculated by using the equation,

$$r_L = \frac{mv}{eB} \tag{1.10}$$

where r_L is Lamoure radius and is found to be 240 G. This magnetic field could be easily attained by using conventional magnets. Since electrons are the source of creation of ions which in turn induce the sputtering, confining the electrons near the target plane will increase the ionization rate and as a result the deposition rate of target material will enhance greatly. The initial design of planar magnetron discharge was put forward by Chapin [13] and is considered widely as the standard configuration of planar magnetron.

1.4.1 Design and working principle

The design consists of a central pole piece magnet of suitable strength and the annular ring of magnets having opposite polarity that surrounds the central pole piece. Disc shaped target with thickness of few millimeter placed above the magnet assembly is used as the cathode. The ejected secondary electrons are energized in the cathode sheath and they try to follow the magnetic field lines. The configuration of the magnetic field lines within the cathode dimension is given in the **Fig. 1.4**. The magnetic lines of force curve back towards the target while the electric field lines are parallel to each other and perpendicular to the target plane. With this direction of electric and magnetic lines of force it can be easily seen that near the centre and the periphery of the target, the electric and magnetic lines of force runs parallel to each other. Also, there exists a region surrounding the entire cathode plane

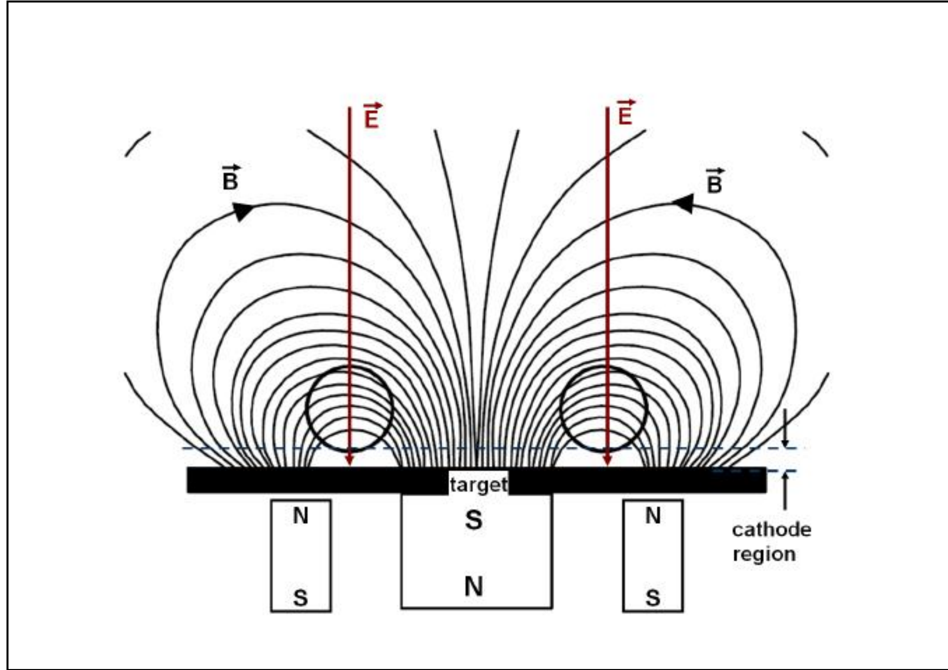

Figure 1.4 Cross sectional view of the magnetic lines of force configuration of the planar magnetron. The circle represents the cross section of the torus shaped electron drift [18].

where the magnetic field is perpendicular to the electric field which is denoted by a circle in the figure. As the electric field is perpendicular to the magnetic field, the drift of the electron which is given by

$$\overrightarrow{v_d} = (\vec{E} \times \vec{B}) / B^2 \tag{1.11}$$

is the maximum in this portion. This region appears as a brightly glowing ring of high intensity that runs parallel to the cathode surface as the maximum ionization of neutral atoms takes place here. The magnetic field lines end again on the cathode surface and the secondary electrons that try to follow these lines are reflected by the magnetic mirror force [17] and the sheath electric field. Thus in a DC planar magnetron device the secondary electrons are trapped in front of the target by suitable orientation of magnetic field and is

responsible for enhancement of ion density in the cathode ring region. Along its motion the secondary electrons will cause further ionization and the ions produced in the trap are accelerated by the cathode field towards the target and bombard it. The cathode field region is in between the torus and the target surface and of the order of 10^6 V/m. The degree of ion bombardment on the target is the maximum below the torus resulting maximum erosion of the target. The eroded region of the target has the same shape as that of the torus and known as the race track region.

1.4.2 Types of Planar magnetron

DC planar magnetron can be classified on the basis of the nature of magnetic field produced or the magnetic arrangement into two types: (1) The 'balanced type' and, (2) The 'unbalanced type'. In the 'balanced magnetron' the magnetic lines of force closes within the target dimension as the pole strength of the central magnet and annular magnets are equal. Thus, the plasma is strongly confined to the target region. A region of dense plasma typically extends some 60mm distances from the target surface. Substrate placed outside this region will not expose itself to the concurrent ion bombardment. Consequently, the ion current drawn at the substrate is very small (typically, < 1 mA cm^{-2}). In the 'unbalanced magnetron' the pole strength of the central magnet and the annular rings of magnets are not equivalent. In the 'type 1' unbalanced magnetron the central pole is strengthened relative to the annular rings of magnets. In this case, the field lines are directed towards the chamber walls and the plasma density in the substrate region is low. In the 'type 2' unbalanced magnetron the outer annular ring of magnets is strengthened relative to the central pole. In this case, some of the field lines are directed towards the substrate. Consequently, the plasma is no longer strongly confined to the target region but is allowed to flow out towards

the substrate. By applying this arrangement of magnets Windows and Savvides [19-20] have shown that substrate current densities of 5 mA cm^{-2} and greater can be routinely generated. A comparison of plasma confinement obtained in different magnetron modes is shown in the **Fig. 1.5.**

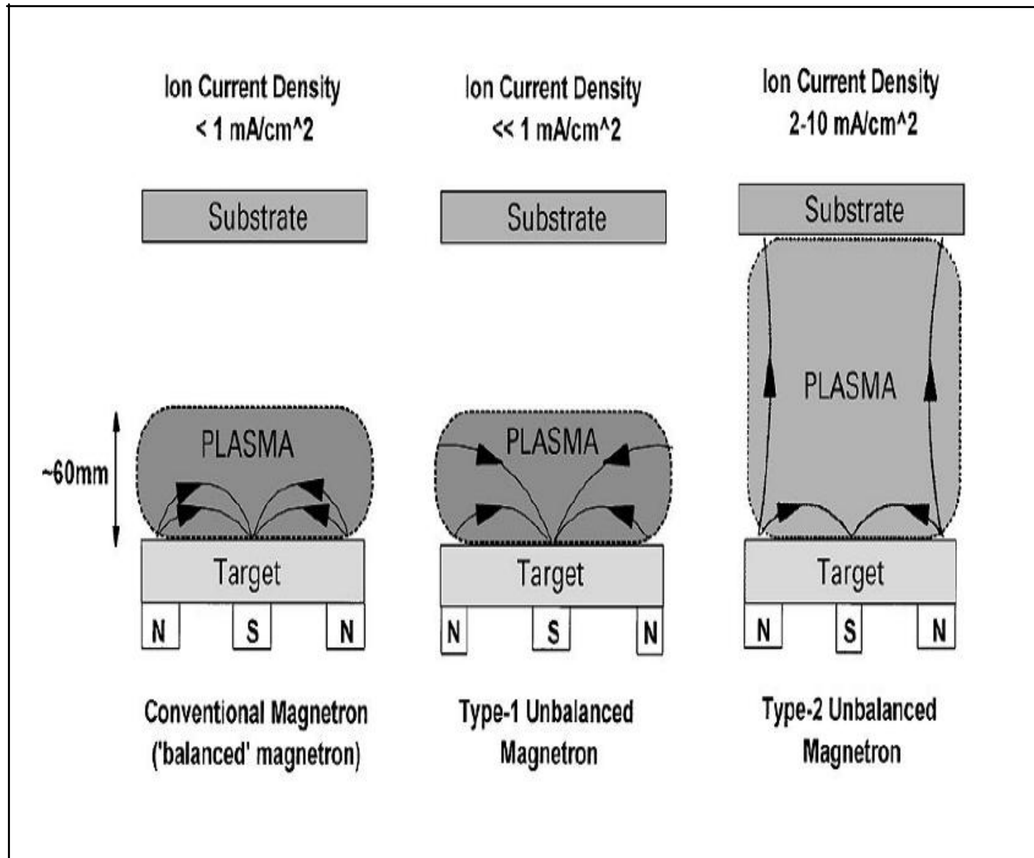

Figure 1.5 Schematic representations of the balanced and unbalanced magnetron [21]

In order to commercially exploit the magnetron sputtering technology, multiple magnetron systems have been introduced. In multiple magnetron system, the magnetic arrays in the adjacentt magnetrons can be configured with either identical or opposite polarities. In the former case, the configuration is known as 'mirrored' and in the later case the configuration is called cross field and both of them are shown in the **Fig. 1.6**.

1.4.3 Qualitative model of DC Planar magnetron sputtering

Magnetron sputtering appears in the form of a high density brightly glowing circular plasma ring of width *w* and mean radius *R* that hovers below the cathode and the ring is embedded in a lower density bulk plasma. The equilibrium properties of the discharge can be explained qualitatively as a function of control parameters such as the discharge current

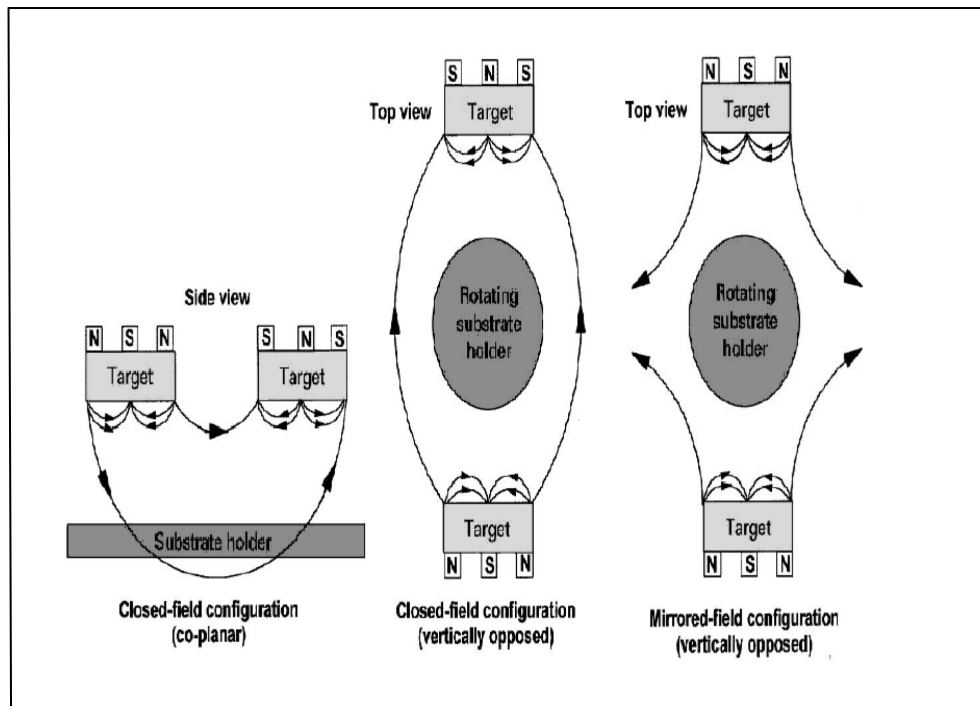

Figure 1.6 Schematic representations of dual unbalanced magnetron configurations [21]

(I_{dc}), working pressure (P), magnetic field strength (B_0) and radius of curvature of magnetic lines of force (R_c). A planar magnetron with a target diameter 75mm typically has a racetrack diameter (R) of 50mm and width (w) of 40mm [8].

1.4.3 (a) Ring width (*w*)

Let the ring has mean height (from the cathode) equal to the gyration radius (r_{ce}).The energetic secondary electrons are trapped on a magnetic field line and can oscillate back

and forth between radii r_1 and r_2. Now, as shown in **Fig. 1.7** for a field line having a radius of curvature R_c at height r_{ce} from the cathode, we have

$$w \approx r_2 - r_1 \tag{1.12}$$

Also from the figure,

$$\frac{w/2}{R_c} = \sin\theta, \; r_{ce} + R_c \cos\theta = R_c \tag{1.13}$$

For small angle approximation and assuming $\frac{w}{2} << R_c$, we obtain from the Eq. (1.13)

$$w = 2 \times (2r_{ce}R_c)^{1/2} \tag{1.14}$$

From the Eq. (1.14) the value of w can be evaluated once r_{ce} and R_c are known.

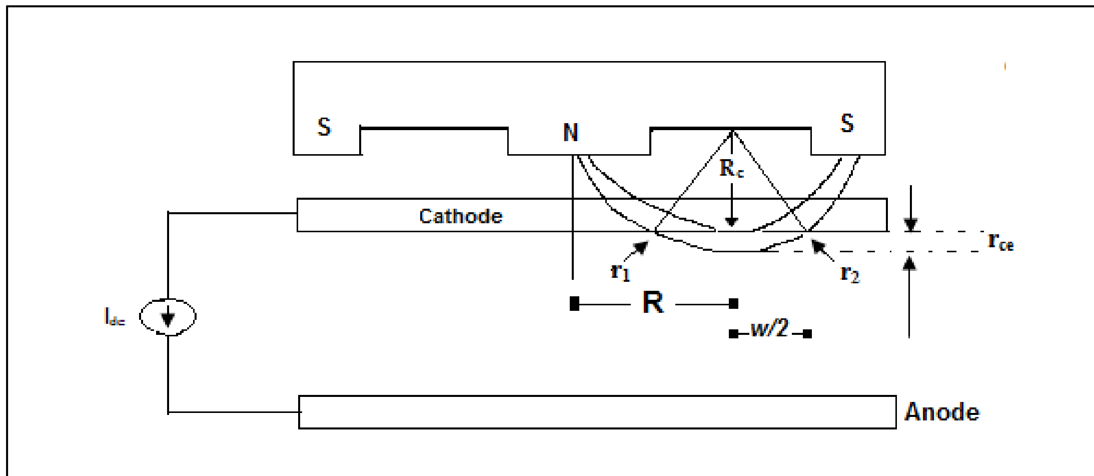

Figure 1.7 Model of dc discharge used for sputtering in planar magnetron. r_{ce} refers electron gyration radius.

1.4.3 (b) The sheath thickness (*S*)

The acceleration of ions from the surface of the ring to the cathode surface through the cathode fall region can be estimated using a collision less Childs Law. In low pressure, the

ion current density can be written as

$$J_i = \frac{4}{9}\varepsilon_0 (\frac{2e}{M})^{1/2} \frac{V_d^{3/2}}{S} \tag{1.15}$$

Now for a thin ring we have

$$J_i = \frac{I_{dc}}{2\pi R w} \tag{1.16}$$

Taking typical magnetron discharge parameters such as I_{dc} = 1A, R = 50mm, w = 40mm, and V_d = 600 V it gives, S = 1.22mm.

1.4.3(c) Electric field (E) through the sheath

Almost all of the applied voltage is dropped across the cathode sheath in the planar magnetron discharge. If ε_c be the energy lost per electron for production of the ion-electron pair, N be the number of ion-electron pairs and V_{dc} is the voltage dropped across the sheath then,

$$N = \frac{V_{dc}}{\varepsilon_c} \tag{1.17}$$

Some of the secondary electrons are reabsorbed by the cathode surface. This leads to an effective secondary emission coefficient γ_{eff} that is less than γ_{se}. Kelly and Arnell [21] estimated that,

$$\gamma_{eff} = \frac{1}{2}\gamma_{se} \tag{1.18}$$

For particle balance in steady state we have,

$$\gamma_{eff} N = 1 \tag{1.19}$$

and therefore we obtain,

$$V_{dc} \approx \frac{2\varepsilon_c}{\gamma_{se}} \tag{1.20}$$

For $\varepsilon_c = 30V$ and $\gamma_{se} = 0.1$, we find $V_{dc} = 600V$.

The potential can be assumed to fall uniformly through the sheath of thickness 1.22 mm and therefore the electric field is given by,

$$E = \frac{V_{dc}}{s} \tag{1.21}$$

The calculated electric field is 4.918×10^5 V/m. It is worthwhile to mention that when the plasma is produced the potential will not fall uniformly and the above calculation is an estimate only for magnetron design.

1.5 Low pressure plasma

The plasma in the DC planar magnetron sputtering device is low pressure collision-less glow discharge plasma [8]. When sufficiently high voltage is applied between the two electrodes kept in low pressure environment, the gas transformed into the state of plasma and a discharge is ignited. The weak electric fields present in the plasma results drift of electrons to the anode and positive ions to the cathode. In plasma the total number of positive charges is equal to number of negative charges as any macroscopic deviation from this condition otherwise were generating high electric fields which would prevent the charges of opposite sigh to leave the plasma volume. Thus although consisting of free charges, the plasma is neutral macroscopically and this condition is called quasi-neutrality and often represented as [22],

$$n_e + \sum_z z_- n_- = \sum_z z_+ n_+ \tag{1.22}$$

where n_e – electron density, n_- – density of negative ions, n_+ – density of positive ions, z – charge number. The separation between the cathode and the anode and the operating gas pressure plays an important role in determining the initiation of the discharge (the breakdown) in the system. After attaining the breakdown, uniformity of the ion bombardment on the cathode surface is lost and is more confined to the surface irregularities in the cathode. The current density on the cathode surface rises in magnitude for negligible rise in applied bias.

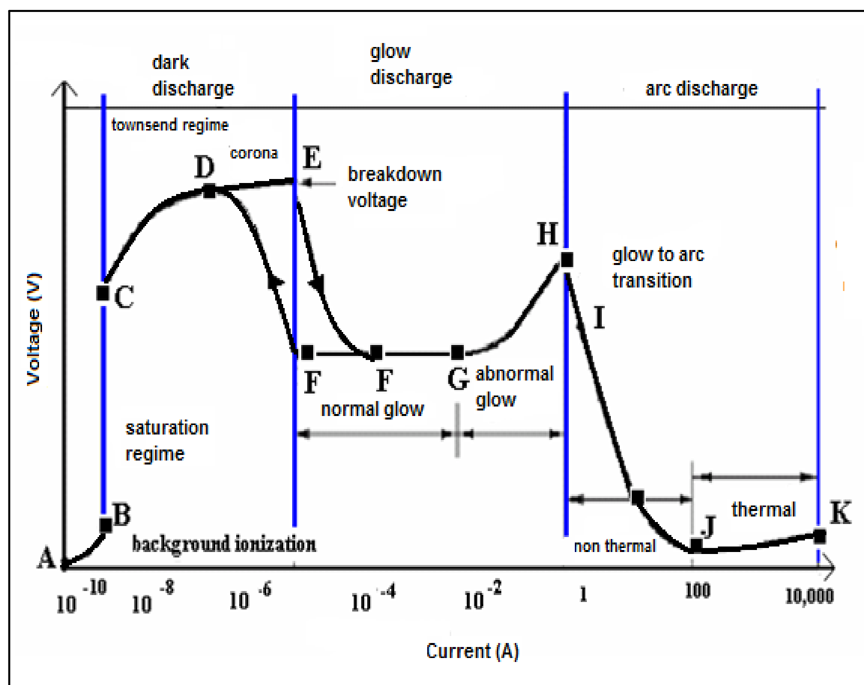

Figure 1.8 Voltage-current characteristics of the dc discharge

This region is termed as the normal glow discharge. Further increase in power causes the discharge to enter into the normal ohm regime i.e., rise in both voltage and the current, the abnormal glow discharge [23]. In this regime, uniform bombardment of the cathode by energetic ions is possible and the current density becomes high. Therefore, this regime is

suitable for sputter deposition [24]. The regime of the *V-I* characteristics of the DC discharge is shown in the **Fig. 1.8**. For a stationary discharge to become self-sustained, the losses of charges to the electrode must be compensated by generation of new charges. The balance is achieved by the generation of the secondary electron emission from the cathode region. In the cathode sheath the secondary electrons gain their full energy. The energetic electrons stepwise transfer their energy to the ionization in the regions adjacent to the sheath. For too low operating gas pressure, the secondary electrons cannot cause enough number of ionizing collisions before striking the chamber walls and are lost. Thus the discharges will not sustain. The selection of suitable operating pressure is very crucial to sustain the discharge.

1.6 The Cathode sheath

When a negative object is brought into contact with the plasma, the spatial violation of quasi-neutrality can occur because of the ability of the charge carriers to electrically shield a perturbation. The negative object will repel electrons from its vicinity leaving a positive space charge around it, thus shielding the negative charge against plasma. The potential distribution in front of an infinite sheet with negative charge can be obtained by solving the Poisons equation and it is given as,

$$V(x) = V_0 \exp(-x/\lambda_D) \quad (1.23)$$

where x is the distance from the sheet, V_0 is the sheet potential and the potential at infinity is taken to be zero. A negative electrode which is fixed in plasma implies a perturbation to the plasma and a sheath is formed in front of it. The potential drops from that of the plasma potential (V_{pl}) to that of the electrode within this layer where quasi-neutrality is strongly-

violated. Matrix sheath presents the simplest model of the high voltage sheath in which the ion density is uniform and electron density drops exponentially according to the Boltzmann law. The thickness of a matrix sheath is given as [8],

$$S_M = \lambda_D \sqrt{\frac{2eU_m}{k_B T_e}} \tag{1.24}$$

with U_m is the voltage drop between the sheath edge and the electrode. The model is suited in case of rapid changes of the electrode potential to the negative values. The approximation used in matrix sheath model is that the attraction of ions to the negative electrode is not considered.

When the movement of ions to the electrode and their density variation is considered the ion matrix sheath is replaced by a Child Langmuir sheath with thickness [8],

$$S_{CL} = \frac{\sqrt{2}}{3} \lambda_D (\frac{2eU_{CL}}{k_B T_e})^{3/4} \tag{1.25}$$

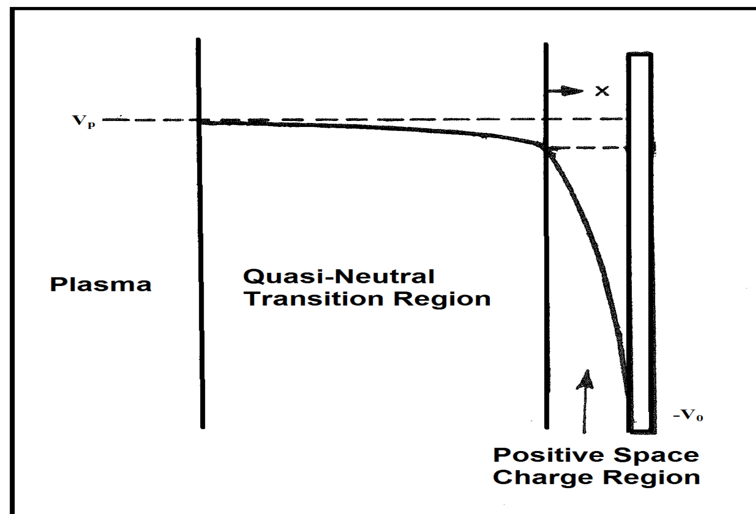

Figure 1.9 Potential variations in front of a negative electrode in contact with plasma. The positive space charge region in front of the negative electrode is the cathode sheath.

The two major drawbacks in this model is the assumption of ions starting from the sheath edge with zero velocity leads to an infinite charge density at the sheath edge and currents measured at the cathode are higher than the prediction of Child Langmuir law. Bohm [25] predicted that a sheath region is actually preceded by a typically much wider region of small potential drop known as the pre-sheath region. The pre-sheath region is a quasi-neutral region having a potential drop of $\frac{k_B T_e}{2e}$. The ions are accelerated in this region to enter the sheath region with a velocity $v_B = \sqrt{\frac{k_B T_e}{M_i}}$ known as Bohm velocity [25].

1.7 Duplex Process: An Introduction

The recent developments in magnetron sputtering allow very high performance coatings to be produced. Indeed, in many applications, magnetron sputtered coatings now outperform the coatings produced by the other techniques. PVD coated tool can offer an increase in life over an uncoated tool of up to 32 times, compared to the 1.5 - 4.5 times increase in life offered by the other techniques [26]. A factor which has limited the exploitation of advanced PVD processes is their unsuitability for use with many substrate materials such as low alloy steel and titanium alloys. In the case of hard coatings, this is due to the lack of load-bearing support provided by the substrate; whereas in the case of corrosion resistant coatings, the pinhole defects have compromised the performance of the coating [27]. To address these problems, and to extend the commercial viability of advanced PVD processes, duplex surface engineering processes have been developed recently. Duplex surface engineering as the sequential application of two (or more) established surface technologies to produce a surface composite with combined properties which are

unobtainable through any individual surface technology [26]. Two general groups are identified; those in which the individual processes complement each other and the combined effects result from the both processes (group 1), and those where one process supplements, or reinforces the other, acting as a pre-, or post-treatment, and the resultant properties are mainly related to one process (group 2). PVD treatment of pre-nitrided steel is a good example of a group 1 process. Plasma nitriding produces a relatively thick (~500 μm), hardened (~10 GPa) subsurface. A 1-5 μm thick titanium nitride (TiN) layer can then be deposited onto the nitrided surface using various PVD techniques, including magnetron sputtering [26]. Components treated in this way exhibit the low wear characteristics of the ceramic coating, combined with the high load-bearing capacity and high fatigue strength characteristics of the nitrided layer. A similar example of duplex surface engineering is the Diamond-like Carbon (DLC) coating-oxygen diffusion process for titanium alloys. Titanium alloys combine high strength to weight ratios and exceptional corrosion resistance, but are also characterized by poor tribological properties and poor load bearing capacity. Again, the tribological properties of the titanium alloy could be significantly improved through the use of a PVD coating. Considering the above factors and the need for improved surface modification process, a duplex composite multilayer process technique with a combination of the well-established Plasma nitriding and Sputtering techniques is developed. For this purpose a variable frequency pulse Plasma nitriding system and the DC Magnetron sputter system is developed.

1.8 Motivation of the Thesis

Reactive sputtering has become one of the most popular methods to deposit compound

thin film. Although reactive sputtering may look simple, however in reality it is a very complex process. Addition of reactive gas will produce a variety of reactive species in otherwise inert plasma. These reactive species in addition of sputtering the target and deposition at the substrate take part in various chemical reactions that occur both at the target and the substrate. The strong interaction of reactive gas species with the cathode surface in magnetron discharge can lead to the poisoning of the target material due to which the stoichiometry of the deposited film and the deposition rate will be affected. A strong non-linearity between the experimentally controllable quantities and the plasma parameters exists [21, 28]. The reactive species are transported to the substrate and the cathode from the plasma medium. The metallurgical properties of the deposited thin films have been intensively investigated in literature [29-32] but the plasma parameters such as the electron density, ion density, and electron temperature of the magnetron discharge are yet to be investigated thoroughly. The mentioned plasma parameters eventually determined the growth and properties of the deposited thin film. Thus, a detailed investigation of the reactive gas added argon plasma is a prime aspect of investigation. Keeping these facts into mind, the present investigation focuses on the following key areas of the planar magnetron sputtering.

1. As the magnetron discharge is self-sustained, the ion induced secondary electron emission coefficient (ISEE) of the target surface plays a crucial role in maintaining the discharge. As the ISEE coefficient values are different for various targets thus the plasma parameters will vary with the types of target. A detailed investigation of the effect of the magnetron targets on the properties of magnetron discharge should deserve the attention of the researchers.

2. The conventional plasma diagnostics like the Langmuir probe, the optical emission spectroscopy have their limitations while using in DC planar magnetron discharge. The probe tip of the Langmuir probe is used to get coated by the material sputtered from the magnetron target during the prolonged deposition. It will increase the charge collection area of the Langmuir probe and it may lead to erroneous results. In order to overcome such limitation, the ion acoustic wave can be used as a suitable alternative diagnostic tool. A major part of this thesis work is focused on the use of the ion acoustic wave as a diagnostic tool in the magnetron discharge plasma. Also a theoretical investigation of the propagation of the linear ion acoustic wave in the background of multi-component plasma is addressed.

3. The glow discharge plasma used for the deposition of the compound thin films by magnetron sputtering is multi-component plasma consisting of positive ions, negative ions and electrons. Such multi-component plasma is formed by gradually adding reactive gases such as nitrogen, oxygen and non reactive gases such as hydrogen in the argon plasma. The behavior of the plasma parameters in the background of the multi-component plasma is completely different from the normal single component plasma. It is due to the complex discharge behavior of the molecular gases and complexity generated by the various plasma species under the influence of crossed magnetic and electric fields. Plasma collective behavior plays an important role in the magnetron discharge, and therefore the dependence of the plasma parameters (density profile, temperature and energy distributions) on the sputtering efficiency as well as on the physio-chemical processes leading to quality film growth in reactive sputtering is undoubtedly a subject for investigation.

4. It is a well known fact that the deposition technique as well as the substrate determines the growth and orientation of the compound thin film. A part of this thesis work is focused on the effect of substrate on the orientation of polycrystalline titanium nitride thin film deposited by the magnetron sputtering technique. It is to be noted that the nitrogen added argon plasma is used for deposition of titanium nitride thin film.
5. While using ion acoustic wave as a diagnostic tool in the oxygen added argon plasma, it was found that with increasing value of the applied voltage, the ion acoustic wave had transformed into soliton. However as done in the previous case, when we try to excite ion acoustic solitary wave in the hydrogen added argon plasma by increasing the amplitude of the applied sinusoidal signal, it seems as the presence of the lighter hydrogen-like ions inhibit the formation of the soliton. This important experimental fact leads to a detail theoretical investigation of the propagation of soliton in such plasma.

1.9 Review of the previous works

1.9.1 The effect of the targets on the properties of the magnetron discharge

The most significant aspect of magnetron sputtering is the presence of plasma medium. The plasma parameters such as electron temperature, electron density, etc. influence the micro structural and mechanical properties of the deposited coating. The behavior of the plasma discharge during the planar magnetron sputtering can mostly be attributed to the target materials, which have different ion induced secondary electron coefficient values. Thornton [33] proposed that the minimum voltage required to sustain the magnetron discharge is

$$V_{\min} = \frac{W_0}{\gamma \varepsilon_i \varepsilon_e} \tag{1.26}$$

with W_0 is the effective ionization energy, ε_i is the ion collection frequency, ε_e is the fraction of the maximum number of ions that is created on the average by primary electrons before it is lost from the system and γ is the effective secondary electron emission coefficient which is the product of ion induced secondary electron emission coefficient γ_{ISEE} and the effective gas ionization probability (Δ) [34]. Assuming a constant Δ at fixed discharge voltage, the inverse of the discharge voltage is proportional to the ISEE coefficient. During the initial stage of the reactive sputtering due to the chemisorptions of the reactive gas molecule on the target surface and the implantation of the reactive gas ions into the target surface, all of the reactive gas will be consumed and the reactive gas partial pressure becomes independent of the reactive gas flow rate up to a critical point. This is the so called 'gettering mechanism' of the magnetron target and is investigated by many authors [35, 36]. The deposited film is metal rich below this critical point. Beyond this critical point, the target will be in the compound mode and the compound thin film takes place on the substrate as well as the target (Poisoning of the target). Deepla et *al.* [37] have studied the details of the compound layer formation on the target surface of the DC planar magnetron discharge. The compound formed on the target of the magnetron sputtering device in general have higher ion induced secondary electron emission coefficient than that of the pure metallic target. It is reported that the compound layer formation on the targets results in the decrease of the absolute value of the target voltage at constant discharge current and thus can modulate the plasma parameters in the bulk region of the discharge [38]. Generally, the influence of the applied electrical power in magnetron sputtering is described using the V-I characteristics of the magnetron target. The total current in a

magnetron increases rapidly with the discharge voltage, which is expressed empirically as [38],

$$I = kV^n \tag{1.27}$$

with I being the discharge current, V is the discharge voltage, and k and n are constants. The latter constant is a measure for the steepness of the V-I characteristic and is generally interpreted as a measure for the magnetron efficiency or the confinement of the electrons by the magnetic field. Its value is in the range of 5 to 15. The constant k and the exponent n depend strongly on the gas-target combination, the design of the magnetron, the magnetic field, and the other experimental parameters. The values of n and k are generally determined by plotting the V-I characteristic on a log–log plot. Westwood et *al.* [39] proposed another equation to describe the V-I characteristic of the magnetron as:

$$I = \beta(V - V_0)^2 \tag{1.28}$$

where V_0 is the minimum voltage required to maintain the discharge, β is a constant which is a measure of steepness of the V-I characteristics. Value of β can be determined by a linear fit to the square root of current (I) as a function of voltage. Based on a PIC/ MC simulation, Kondo et *al.* [40] concluded that the effect of the ISEE coefficient on the magnetron discharge is qualitatively analogous to the DC glow discharge. Their simulations show that at constant discharge voltage, a higher ISEE coefficient results in a higher plasma density. A higher plasma density results in lower plasma impedance, and therefore, a higher value of β is expected with increasing ISEE coefficient. Saikia et *al.* [41-42] reported the modulation of the V-I characteristics of the magnetron due to the addition of the reactive and non-reactive gas for different magnetron targets.

1.9.2 The use of the plasma diagnostics in the magnetron discharge

In the range of magnetron operation, the plasma is weakly ionized and non-collisional. In order to control the deposition process the plasma needs to be characterized. Under such condition, the electrostatic probe such as the Langmuir probe can be used safely. Significant amount of work has been done using the Langmuir probe as a diagnostic tool for the magnetron plasma [43-45]. It is important to mention that for deposition process optimization, the knowledge of the electron energy distribution function (EEDF) is of particular importance. Druyvesteyn [46-47] introduced the idea of determining the EEDF from the second derivative of the *I-V* characteristics obtained by a Langmuir probe in 1940. However, only in the early 1990's with the advent of digital filtering and the progress in digital electronics, the EEDF measurement has become feasible. Since then lots of technique have been used to study the EEDF processes in plasmas. Generally a bi-Maxwellian electron energy distribution functions are reported in low pressure magnetron discharge plasmas by many authors [48-50]. Most of the studies mentioned above used the Langmuir probe for the determination of plasma parameters in the absence of reactive gases in magnetron discharge. But the addition of reactive gas influences the plasma properties significantly [42, 51]. Under such circumstances the use of Langmuir probe is a challenge due to the presence of ions with different masses. Laidani et *al.* [52] developed a procedure of dividing the ions present in the reactive gas added magnetron plasma based upon their masses for determination of electron temperature and density by the Langmuir probe. This procedure enjoys a significant success for determination of plasma parameters for hydrogen added argon magnetron discharge plasma. Addition of electro-negative gas such as oxygen can produce significant amount of negative ions in the plasma itself. Bradley et *al.* [53]

determine the relative concentration of negative ions in such plasma using a Langmuir probe assisted by a laser photo-detachment technique. A certain limitation of the Langmuir probe diagnostic in the magnetron sputtering device is the coating of the probe tip by the sputtered atoms from the target during the prolonged deposition [54]. The charge collection area of the probe increases with further deposition and it can lead to erroneous results. Under such conditions the ion acoustic waves can be used as an alternative diagnostic to probe the magnetron discharge plasma. The use of the ion acoustic waves first recognized by Langmuir as a diagnostic of the plasma parameters in a wide variety of low temperature plasma is extensively reported by many authors [55-57]. Plasma containing both positive and negative ions as well as the magnetron discharge supports ion acoustic waves. Alexeff and Jones [58] excited ion acoustic waves by applying sinusoidal signal to a grid mounted in collision-less rare gas plasmas and detecting them with a small movable cylindrical probe. Using this technique the determination of electron temperature and density for rare gases has been done extensively by many authors [59-60]. For the multi-component plasma such as the reactive gas added magnetron discharge plasma, it is possible to determine the relative concentration of the various species present in the discharge [51] using ion acoustic waves. Another diagnostic technique that is used very frequently to characterize plasma is the Optical Emission Spectroscopy (OES). It is a non-intrusive technique used to quantify and identify the different species present in the magnetron discharge. Various investigations using OES technique in magnetron discharge plasma [61-63] have already been reported in literature.

1.9.3 Study of plasma properties as a function of the input parameters

In the DC magnetron sputtering, the input power and gas pressure are two major parameters to tune the deposition process. For single component plasma, Wu [64] found that with increased power injected into the magnetron discharge, both the discharge current (ion flux) and voltage (ion energy) increase resulting in general, increases of electron density, floating potential, and plasma potential, while electron temperature was relatively insensitive. With the increased discharge pressure, the electron density undergoes an initial increase trend and then starts to decrease, and electron temperature gets reduced. Seo et *al.*[21] have observed the anomalous behaviors of the electron density and the effective electron temperature with changing pressure, and the EEDF transition from a bi-Maxwellian distribution at low pressures to a Druyvesteyn-like distribution at high pressures (above 20 mTorr). With the addition of reactive gases such as nitrogen, oxygen in the reactive sputtering and hydrogen in the non-reactive sputtering the magnetron discharge plasma becomes multi-component consisting of negative ions, positive ions and electrons. As the ionization potential of such gases is different from that of the sputtering gas (argon), the modulation of electron density, electron temperature, ion density, and plasma potential are modified from that of the single component magnetron discharge. It is worthwhile to mention that one of the focuses of the present investigation is to observe the effect of addition of hydrogen, nitrogen and oxygen on the plasma parameters of the argon magnetron discharge plasma.

A number of investigations of the interaction between argon and hydrogen species have been reported [65-66] but these were carried out under different conditions from those that occur in sputtering system. For instances, Knearstubb and Tickner [67] used mass spectroscopy techniques to measure the relative densities of Ar^+ and ArH^+ ions in the glow

discharge at pressures above 100 Pa. Maniv et *al.* [68] first studied the effect of hydrogen addition in DC planar magnetron sputtering system and based on the various reactions they predicted the insensitivity of magnetron deposition rate to hydrogen addition. However, Laidani et *al.* [52] have found that hydrogen exerts a positive effect on the film deposition rate at the lowest end of the hydrogen concentration range, and the enhancing deposition effect is correlated with a high density of Ar^+ ions in the plasma and a high energy flux carried by the ions to the cathode. Nitrogen added argon plasma is used for the deposition of nitride thin film by the magnetron sputtering. Bogaerts [69] have studied the effect of nitrogen addition in the argon glow discharge using a hybrid Monte Carlo — Fluid model on the density variation of electron and different ions. Borah et *al.* [70] reported a careful measurement of the basic plasma parameters and cathode sheath parameters in a post magnetron device with the nitrogen added argon plasma. For such plasma, Debal et *al.* [71] have studied the spatially resolved optical emission spectroscopy of the DC magnetron sputtering device. However, fewer reports of the correlation of the observed plasma properties with the orientation and as such the metallurgical properties of the nitride thin film are available in literature [42]. Boagearts et *al.* [72] studied the effects of oxygen addition to the argon glow discharge using a hybrid Monte Carlo-fluid model. Maniv and Westwood [73] studied the reactive sputtering of Al target in the Ar/O_2 mixture plasma. Windows et *al.* [74] designed the argon added oxygen magnetron as sources of the high ion flux. The material aspects of the argon-oxygen magnetron discharge have been extensively studied for the last two decades by several authors [75-78].

1.9.4 The effect of the substrate on the orientation of the deposited film

Planar magnetron reactive sputtering is generally done in order to deposit dielectric coatings like the nitrides and oxides as well as carbides and silicides [79-80]. In the industry, surface modification by the nitride coatings such as TiN, AlN, CrN and the oxide coatings such as TiO_2, Cr_2O_3 enjoy a prominent role. Owing to its high hardness [81], low friction coefficient [82], high degree of bio-compatibility [83], and lustrous golden yellow appearance [84], the TiN coatings have attracted a great deal of attention of the researchers. TiN has the face centered cubic (fcc) structure generally represented as TiN_x with $x = 1$ being the stoichiometric compound and the other compounds with $0.5 < x < 1$ are also possible. In the reactive sputtering the plasma properties influence the microstructure such as the grain size, texture, density etc. and the mechanical properties such as the hardness, internal stress, resistivity of the deposited thin film [85-86]. The presence of residual stress developed in the coatings during the deposition is responsible for most of the observed mechanical behaviors. The variation of energetic ion bombardment by tuning the plasma properties of the discharge has been established to be an effective method for controlling the residual stress formation in the TiN coatings [87]. The micro-structure of the deposited coatings is found to be functions of the various plasma dependent process parameters such as the deposition rate, discharge power-voltage, substrate temperature etc. Along with the plasma parameters, the substrate can also influence the orientation and therefore, the metallurgical and stoichiometry of the deposited thin film. Pelleg et *al.* [88] reported the texture growth of the TiN coatings deposited on the glass substrate and plasma nitrided substrate, respectively. Jones et *al.* [89] investigated the effect of substrate preparation on the preferred orientation of the TiN coatings deposited by the reactive sputtering. It is to be

mentioned that very little is known about the preferred orientation of the polycrystalline TiN on the plasma nitrided substrate [90].

1.9.5 Theoretical study on the propagation of ion acoustic soliton in low temperature plasma

Theory of ion acoustic compressive solitary wave has been developed due to the pioneering work of Korteweg-de Vries [91], Zabusky-Kruskal [92], Washimi-Taniuti [93], and many others [94-95]. Tappert [96] and Tagare [97] introduced the ion temperature effect to the otherwise cold ion theory. With introduction of ion temperature, an adequate theory to explain experimental results thus formed. Using the Sagdeev Pseudo-potential technique [98], Sakamaka [99] has solved the warm ions fluid equation to obtain electron and ion density. Since then, this technique has been followed by many researchers. Presence of low mass ion can significantly affect the propagation of the ion acoustic soliton. Tran [100] has shown that adding a small percentage of light ions such as the hydrogen and helium ions can inhibit the formation of soliton in argon plasma. Saikia et *al.* [54] made a detailed investigation of this effect in the background of a DC planar magnetron discharge.

1.10 Summary of chapters

The chapter wise summary of the thesis is given below:

<u>Chapter 2. Experimental set up</u>

Design and fabrication of the experimental setup is given in Chapter 2. For a single planar magnetron, the process parameters like base vacuum, required pumping speed, gas flow rate and operating pressure are calculated. The magnetron is mounted with Titanium, Chromium, and Copper targets and is operated in the DC mode. Argon is used as the sputtering gas while oxygen and nitrogen are used as the reactive gas. One set of

experiments is performed with adding hydrogen to the argon magnetron discharge. The characterization of the magnetron plasma is done with using the Langmuir probe with its design explained in details. The deposition rate is monitored using a quartz crystal thickness monitor. Optical emission spectroscopy is also done in order to characterize the magnetron discharge. Ion acoustic waves (IAW) are used as an alternative diagnostic in the bulk region of magnetron discharge. The phase velocities of the IAW are used to measure the relative concentration of ions in such plasma.

Chapter 3. Study on the effect of target on the plasma parameters of hydrogen added argon DC planar magnetron plasma

The effect of magnetron target on the different plasma parameters of the argon-hydrogen (Ar/H_2) DC magnetron discharge is examined in this chapter. Here, Copper (Cu) and Chromium (Cr) are used as the magnetron targets. The value of the plasma parameters such as electron temperature ($k_B T_e$) electron density (n_e), ion density (n_i), degree of ionization of Ar, and degree of dissociation of H_2 for both the target are studied as a function of the hydrogen content in the discharge. The plasma parameters are determined by using the Langmuir probe and Optical emission spectroscopy. On the basis of the different reactions in the gas phase, the variation of the plasma parameters and sputtering rate are explained. The enhanced value of the electron density, ion density, degree of ionization of Ar, and degree of dissociation of H_2 for Cr compared to Cu target is explained on the basis of its higher ion induced secondary electron emission coefficient (ISEE) value.

Chapter 4. Probing magnetron discharge plasma with ion acoustic wave

This chapter discusses the utility of the ion acoustic waves (IAW) as a diagnostic tool in

the magnetron discharge plasma. Owing to the several limitation of the Langmuir probe, the IAW is used as an alternative probe for oxygen added argon magnetron plasma. The temporal behavior of the ion acoustic waves excited from a stainless steel grid inside the plasma chamber is used to determine the relative negative ion concentration in the magnetron discharge plasma. Optical emission spectroscopy further confirms the modulation of the negative ion density as a function of discharge conditions. The values of the relative negative ion concentration as measured by ion acoustic waves have been compared with that measured by a single Langmuir probe and a similarity in results has been observed in both the techniques.

Chapter 5. Effect of the process parameters on the properties of argon–nitrogen plasma for titanium nitride film deposition

The effect of working pressure on the physical properties and sputtering efficiencies of the argon–nitrogen (Ar/N_2) plasma in the DC magnetron discharge is investigated. The Ar/N_2 discharge is used to deposit the titanium nitride thin (TiN) films on the high speed steel substrate. The physical plasma parameters are determined by using the Langmuir probe and Optical emission spectroscopy. On the basis of the different reactions in the gas phase, the variations of plasma parameters and sputtering rate are explained. A prominent change of the electron temperature, electron density, ion density, and degree of ionization of Ar is found as a function of working pressure. The deposited coatings are characterized using X Ray Diffractometer (XRD) and the effect of the plasma parameters on the growth of the TiN deposited high speed steel is established.

Chapter 6. Role of the substrate on the growth of the titanium nitride thin film

This chapter investigates the role of the plasma nitrided substrate on the preferential growth

of TiN which is expressed in the form of texture coefficients of the deposited film. Titanium nitride (TiN) films are prepared by DC magnetron sputtering of a titanium (Ti) target in an argon- nitrogen atmosphere on bare and pulsed DC plasma-nitrided high-speed steel (AISI M2) substrate. The detailed structure of the coatings is analyzed by the X-ray diffraction study. The texture coefficient (T_c) determined from the X-ray diffraction studies at various deposition conditions gives information about the crystallographic orientation. It is found that the same deposition condition leads to different orientation of TiN coatings on trhe bare AISI M2 and plasma-nitrided AISI M2 substrate. The results are discussed in terms of energy minimization and substrate-induced preferred orientation.

Chapter 7. Theoretical investigation of the ion acoustic soliton in hydrogen added argon plasma

In this chapter the effect of hydrogen addition on the formation and properties of the ion acoustic solitary wave in the DC argon plasma is theoretically investigated. In general it was known from the earlier studies that the addition of hydrogen reduces the amplitude and increase the width of the solitary wave in the argon glow discharge. In Chapter 7, this fact is experimentally obtained and it is followed by a detailed theoretical investigation on the modulation of solitons amplitude and width as a function of the hydrogen addition. By coupling fluid equations with Poisons equation for such multi-component plasma, the Mach number and amplitude of the solitary wave are determined following pseudo potential method.

Chapter 8. Summary and Future Scope

The final chapter highlights the results and describes the conclusions of the study. The scope for future investigations is also briefly described.

1.11 Scope of the Thesis

The thesis "Studies on DC planar magnetron glow discharge plasma" encompasses the studies on the addition of molecular gases such as hydrogen, nitrogen and oxygen to argon magnetron discharge and different magnetron targets for various purposes. For simplicity, the scope of the thesis is tabulated as follows:

Studies on the DC magnetron glow discharge plasma		
Non-reactive sputtering of Cr, Cu	Reactive sputtering of Ti	
H_2 added argon plasma	N_2 added argon plasma	O_2 added argon plasma
1. Target effect on plasma parameters. 2. Hydrogen addition effect on plasma parameters. 3. Hydrogen addition effect on the non linear propagation of IAW (Soliton).	1. Working pressure effect on plasma parameters. 2. Role of plasma parameters on orientation of TiN thin film. 3.Influence of substrate on preferential growth of TiN.	1. Modulation of plasma parameters with oxygen addition. 2. Probing negative oxygen ion density with IAW diagnostics.

References

[1] J. E. Mahan, *Physical Vapor Deposition of Thin films*, pp 336, Wiley-VCH, New York January 2000.

[2] S. Swann, Phys. Technol. **19,** 67 (1988).

[3] M. W. Thompson, Phys. Rep. **69,** 335 (1981).

[4] ed R. Behrisch and W. Eckstein, editors. *Sputtering by Particle Bombardment* (Topics Appl. Physics vol 110). Springer Verlag, Berlin, 2007.

[5] R. Smith, D. E. Harrison, and B. J. Garrison, Phys. Rev. B **40,** 93 (1989).

[6] B. C. Chapman. *Glow Discharge Processes*, pp 180, John Wiley and Sons, Inc., 1980.

[7] P. Sigmund, *Stooping of the heavy ions*, Springer Tracts in Modern Physics, Vol. 204 (2004).

[8] M. A. Libermann and A. J. Lichtenberg, *Principles of Plasma Discharges and materials Processing,* Wiley Interscience, New Jersey, 2005.

[9] I. Safi, Surf. Coat. Technol. **127,** 203 (2000).

[10] S. Kadlec, J. Musil, and H. Vyskocil, J. Phys. D: Appl. Phys. **19,** 190 (1986).

[11]S. Berg, H.-O. Blom, T. Larsson, and C. Nender, J. Vac. Sci. Technol. A **5 (2),** 202 (1987).

[12] H. R. Haufman, J. Vac. Sci. Technol. A **21,** 725 (1982)**.**

[13] W. Kern. *Thin Film Processes*, chapter II-4 - Planar Magnetron Sputetring, page 135. Academic Press, 1979.

[14] H.G. Dehmelt, Advances in Atomic and Molecular Physics **3,** 53 (1968).

[15] M. Chodorow et al. *Reference Data for Engineers - Radio, Electronics, Computer, and Communications*, Elsevier Science, The Netherlands, 2002.

[16] G. F. Amelio, J. Vac. Sci. Technol. **7,** 593 (1970).

[17] S-H. Seo, and H-Y. Chung, J. Appl. Phys. **96,** 1310 (2004).

[18] K. K. Kishor, Thesis: Plasma Assisted Physical Vapor Deposition of Nano-Structured Coatings. Institute for Plasma Research, India (2011).

[19] B. Window, N. Savvides, J. Vac. Sci. Technol. A **4(2),** 453 (1986).

[20] N. Savvides , B. Window, J. Vac. Sci. Technol. A **4(2),** 504 (1986).

[21] P. G. Kelly, and R. D. Arnell**,** Vacuum **56,** 159 (2000).

[22] F. F. Chen, Introduction to Plasma Physics and Controlled Fusion, Plenum Press, 2nd edition, 1984.

[23] Yu. P. Raizer, *Gas Discharge Physics*, Springer Verlag, Berlin, 1997.

[24] J. L. Vossen and J. J. Cuomo, *Thin film processes*, chapter II-1, Glow discharge sputter deposition, Academic Press, Orlando, 1978.

[25] D. Bohm, In the Characteristics of Electrical Discharges in Magnetic Field, ed. A. Guthrie, and R. K. Wakerlling, McGraw Hill, New York and London (1949).

[26] Y. Sun, and T. Bell, Mat. Sci. Eng. A **140,** 419 (1991).

[27] J. E. Sundgren, Thin Solid Films, **128,** 21 (1985)**.**

[28] C.D. Tsiogas, and J.N. Avaritsiotis J. Appl. Phys. **71,** 5173 (1992).

[29] Y. H. Lu et *al.,* J. Vac. Sci.Technol. A **25,** 1539 (2007).

[30] S. Veprek. J. Vac. Sci. Technol. **17,** (2401) 1999.

[31] R. W. Siegel and G. E. Fougere, *Nanophase Materials,* Kluwer academic Publishers, 1994.

[32] H. Oettel and R. Wiedemann, Surf. and Coat. Technol. **76-77,** 265 (1995).

[33] J. A. Thornton, J. Vac. Sci. Technol. **15,** 171 (1978).

[34] G. Buyle, W. De Bosscher, D. Depla, K. Eufinger, J. Haemers, R. De Gryse, Vacuum **70,** 29(2003).

[35] S. Berg, H.-O. Blom, T. Larsson, and C. Nender, J. Vac. Sci. Technol. A **5 (2)**, 202 (1987).

[36] D. Depla, and R De. Gryse, Plasma Sources Sci. Technol. **10,** 547 (2001).

[37] D. Deepla, and R De. Gryse, Surf. Coat. Technol. **183,** 190 (2004).

[38] D. Deepla, G. Buyle, J. Haemers and R De. Gryse, Surf. Coat. Technol. **200,** 4329 (2006).

[39] W.D. Westwood, S. Maniv, P.J. Scanlon, J. Appl. Phys. **54,** 6841 (1983).

[40] S. Kondo, K. Nanbu, J. Phys. D: Appl. Phys. **32,** 1142 (1999).

[41] P. Saikia, B. Kakati, and B. K. Saikia, Phys. Plasmas. **20,** 103505 (2013).

[42] P. Saikia, and B. Kakati, J. Vac. Sci. Technol. **31,** 061307 (2013), Erratum: "Effect of process parameters on properties of argon–nitrogen plasma for titanium nitride film deposition, P. Saikia, B. Kakati, and B. K. Saikia, J. Vac. Sci. Technol. **A 32,** 043401 (2014) doi: http://dx.doi.org/10.1116/1.4884595.

[43] S. M. Rossanagel and H. R. Kaufman, J. Vac. Sci. Technol. A **4,** 1822 (1986).

[44] P. Sigurjonsson, and J. T. Gudmundsson, J. Phys. Conf. Ser. **100,** 062018 (2008).

[45] P. Spatenka, J. Ulcek and J. Blazek, Vacuum 55, 165 (1999).

[46] M. J. Druyvestenyn, and F. M. Penning, Rev. Mod. Phys. **2,** 87 (1940).

[47] M. J. Druyvestenyn, Z. Phys. 64, 781 (1930).

[48] S-H. Seo, J-H. In, and H. Y. Chang, Plasma Sources Sci. Technol. **14,** 576 (2005).

[49] J. T. Gudmundsson, P. Sigurjonsson, P. Larsson, D. Lundin, and U. Helmersson, J. Appl. Phys. **105,** 123302 (2009).

[50] C Costin, L Marques, G Popa, and G Gousset, Plasma Sources Sci. Technol. **14,** 168 (2005).

[51] P. Saikia, B. K. Saikia, K. S. Goswami, and A. Phukan, J. Vac. Sci. Technol A **32,** 031303 (2014).

[52] N. Laidani, R. Bartali, P. Tosi and M. Anderle, J. Phys. D: Appl. Phys. **37, 2593** (2004).

[53] J. W. Bradley, R. Dodd, S.-D. You, N. Sirse, and S. K. Karkari, J. Vac. Sci. Technol A **29,** 031305 (2011)**.**

[54] P. Saikia, K. S. Goswami, and B. K. Saikia, Phys. Plasmas. **21,** 033501 (2014)**.**

[55] N. Hershowitz, and Y-C Ghim, Plasma Sources Sci. Technol. **18**, 014018 (2009).

[56] B. Sang, N. D'Angelo, and R. L. Melvino, Phys. Fluids B **3(2)**, 284 (1991).

[57] W. gekelman et *al.,* Am. J. Phys. **75 (2)**, 103 (2007).

[58] I. Allexef , W. D. Jones, and K. E. Lonngren, Phys. Rev. Lett., **21,** 878 (1968).

[59] H. Ikezi ,R. J. Taylor, and D. R. Backer, Phys. Rev. Lett. **25,** 11 (1970).

[60] H. Ikezi, and K. E. Lonngren, Phys. Lett. **42 A,** 29 (1972).

[61] J Lopez, W Zhu, A Freilich, A Belkind, and K Becker J. Phys. D: Appl. Phys. **38,** 1769 (2005).

[62] K. Maca´k, V. Kouznetsov, J. Schneider, U. Helmerssona and I. Petrov, J. Vac. Sci. Technol. A **18 (4),** 1533 (2000).

[63] A. P. Ehiasarian et *al.,* Vacuum **65,** 147 (2002).

[64] S. Z. Wu, J. Appl. Phys. **98,** 083301 (2005).

[65] A. A. Ivanov Jr. et *al.,* Rev. Sci. Instrum. **75,** 1747 (2004).

[66] A. W. DeSiva et *al.,* Phys. Fluids. B **4(2),** 458 (1992).

[67] P. F. Knewstubb, and A. W. Tickner, J. Chem. Phys. **38,** 464 (1963).

[68] S. Maniv, and W. D. Westwood, J. Vac. Sci. Technol. **17,** 403 (1980).

[69] A. Bogaerts, Spectrochim. Acta Part B **64,** 126 (2009).

[70] S. M. Borah et *al.,* J. Phys. D: Appl. Phys. **41,** 195205 (2008).

[71] F. Debal et *al.,* Plasma Sources Sci. Technol. **9,** 152 (1999).

[72] A. Bogaerts, Spectrochim. Acta. Part B **64,** 1266 (2009).

[73] S. Maniv, and W. D. Westwood, J. Vac. Sci. Technol. **17,** 743 (1980).

[74] B. Windows, and N. Savvides, J. Vac. Sci. Technol. **4,** 453 (1998).

[75] A. E. Komlov, V. I. Shapovalov and, N. S. Shutova, Tech. Phys. **57,** 1030 (2012).

[76] J. M. Bennelt et *al.,* Appl. Opt. **28,** 3308 (1989).

[77] G. A. Battinson et *al.,* Thin Solid Films **371**, 126 (2000).

[78] W. Zhou et *al.,* Journal of the Korean Physical Society, **49**, 2168 (2006).

[79] P.J. Kelly, J. Vac. Sci. Technol. A **17 (3)**, 945 (1999).

[80]N. Li, J.P. Allain, and D.N. Ruzic, Surf. Coat. Technol. **149,** 161 (2002).

[81] S. Veprek, J. Vac. Sci. Technol. A **17,** 2401 (1999).

[82] E. Valkonen, C. G. Ribbing, and J. E. Sundgren, Appl. Opt. **25,** 3624 (1986).

[83] P. Engel, G. Schang, and G. K. Wolf, Surf. Coat. Technol. **98,** 1002 (1998).

[84] Y. Chiba, T. Omura, and H. Ichimura, J. Mater. Res. **8,** 1109 (1993).

[85] B. Subramaniam, K. Prabakaran, and M. Jayacandran, Bull. Mater. Sci. **35,** 505 (2012).

[86] Y. S. Jung et *al.,* Thin Solid Films **445,** 63 (2005).

[87] D.S. Rickerby et *al.,* Thin Solid. Films **154,** 125 (1987).

[88] J. Pelleg, L. Z. Zevin, S. Lungo, N. Croitoru, Thin Solid Films **197,** 117 (1991).

[89] M. I. Jones, I. R. McColl, D. M. Grant, Surf. Coat. Technol. **132,** 143 (2000).

[90] P. Saikia et *al.,* Journal of Theoretical and Applied Physics **7,** 66 (2013). doi:10.1186/2251-7235-7-66.

[91] D. J. Kortweg and G. de Vries, Philos. Mag. **39**, 433 (1895).

[92]N. J. Zabusky and M. D. Kruskal, Phys. Rev. Lett. **15**, 240 (1965).

[93] H. Washimi and T. Taniuti, Phys. Rev. Lett. **17**, 996 (1966).

[94] C. S. Gardner, J. M. Greene, M. D. Kruskal, and R. Miura, Phys. Rev. Lett. **19**, 1095 (1967).

[95] N. Asano, T. Taniuti, and N. Yajima, J. Math. Phys. **10**, 2020 (1969).

[96] F. D. Tappert, Phys. Fluids **15**, 2446 (1972).

[97] S. G. Tagare, Plasma Phys. **15**, 1247 (1973).

[98] R. Z. Sagdeev, *Reviews of Plasma Physics*, ed. M. A. Leontovich Consultants Bureau, New York, 1966.

[99] P. H. Sakanaka, Phys. Fluids **15**, 304 (1972).

[100] M. Q. Tran, Physica Scripta **20,** 317 (1979).

CHAPTER 2

Experimental set up

The details of the magnetron setup for depositing the elemental and compound coatings and the deposition parameters chosen for various types of coatings are described in this chapter. Section 2.1 describes the basic considerations in a magnetron discharge, section 2.2 describes the DC planar magnetron set-up used with details of the pumping systems, the arrangement of the magnetron and the substrate, section 2.3 describes various diagnostic tools and techniques, section 2.4 describes the initial plasma characterization experiments done to understand the deposition characteristics of the magnetron for future deposition experiments. As thin film deposition of titanium nitride (TiN) is done on plasma nitrided substrate, a schematic diagram of the experimental setup for plasma nitriding with detailed procedure is given in section 2.5.

2.1 Basic consideration for magnetron operation

The discharge voltage (V) that is required to drive the discharge current (I) through the magnetron system is a function the system pressure (p) [1]. The rate of the thin film formation on the substrate will depend on the amount of sputtering of the target which in turn will depend on the ion flux at the target and on the discharge current. The choice of the sputtering pressure (p) and the implied choice of the V-I characteristics are thus important and following section discusses the criterion in selecting the basic parameters and deciding on the nature of the sputtering gas.

2.1.1 Choosing the sputtering gas

As long as the actual sputtering process is concerned, it does not really matter whether we use neutral atoms or ions, but as it is easy to accelerate the ions to the energies required for

sputtering by an electric field, normally ions are used. It is much easier to ionize atoms when they are in the gaseous state; it is obvious to use gases for ion sources. The inert gas will give the highest sputtering yield compared to the other gases [1]. Among the inert gases argon is almost always used in sputter deposition because it is easily available, cheaper and the sputtering yield is only a factor or two down on xenon at sputter deposition energies [2].

2.1.2 Choosing the pressure range

As mentioned in the Chapter 1, the use of magnetic field in the magnetron sputtering device increases the ionization efficiency and hence, the deposition rate is enhanced. Both the glow discharge and film deposition by the sputtering impose the operating pressure limitation. The upper limit of the operating pressure in the magnetron device is set up by the requirement that the minimum target-substrate separation should be equal to the mean free paths of the sputtered neutral collisions with the neutral gas atoms (λ_{N-Ar}). For sputtered target atoms, the neutral-neutral collision cross-section is observed to be $\sigma_{N-Ar} = 2\times10^{-20} m^2$ [2]. The mean free paths (λ_{N-Ar}) is expressed as,

$$\lambda_{N-Ar} = \frac{1}{n\sigma_{N-Ar}} \quad (2.1)$$

Now, for reasonable value of 10 cm as the target-substrate separation (therefore equal to mean free path) and inserting the value of σ_{N-Ar} in Eq. (2.1), we get $n = 5\times10^{20}$ m^{-3} where n is the neutral argon density and it corresponds to an operating pressure of 2.07×10^{-2} mbar. The glow discharge sets a lower pressure limit. The discharge is sustained by the secondary electrons making ionization collisions with the neutral gas. The number of

ionizing collision decreases with decreasing gas density and hence the gas pressure. Thus a minimum value of the gas pressure exists in order to sustain the glow discharge [3].

2.1.3 Choosing the electrical conditions for the glow discharge

In order to choose electrical condition for planar magnetron sputtering we have to take into account the following factors

(a) Sputtering yield (Λ_{sput}) within the allowed pressure range for sputtering.

(b) Sputtering yield per unit energy input (Λ_{sput}/E).

(c) Safety and economy of the process which means lower operating voltage.

Fig. 2.1 shows the apparent sputtering yield of a magnetron target (Nickel) as a function of the working pressure. It is clear from the figure that within the allowed range of the operating pressure (below 20 mtorr) the sputtering yield is almost independent of the gas pressure.

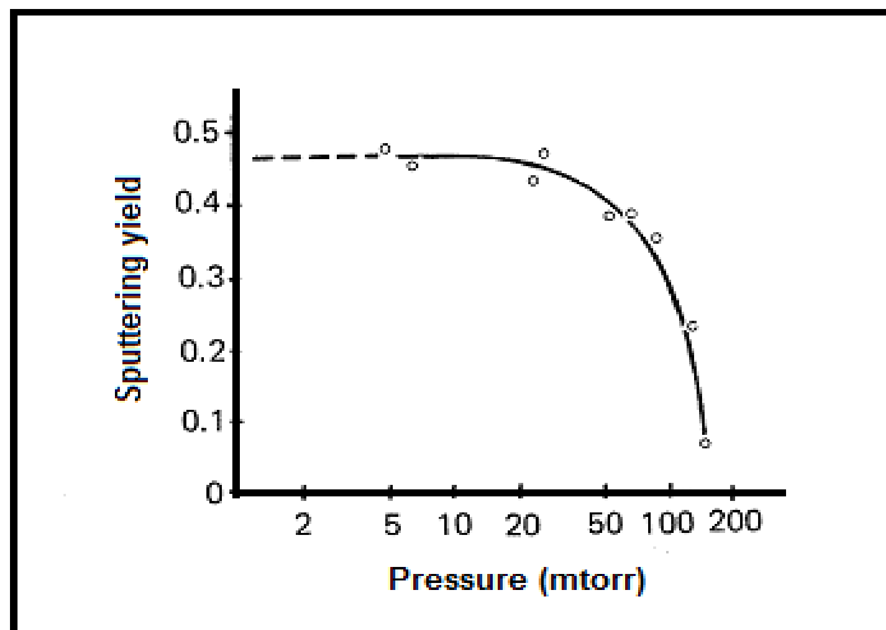

Figure 2.1 Variation of the apparent sputtering yield of the nickel Vs argon gas pressure [4].

The rate of the sputtering also depends on the flux of ions and energetic neutrals. The target current consists of the ion flux as well as secondary electrons reaching the target. **Fig. 2.2** shows the sputtering yield of the target per unit energy input.

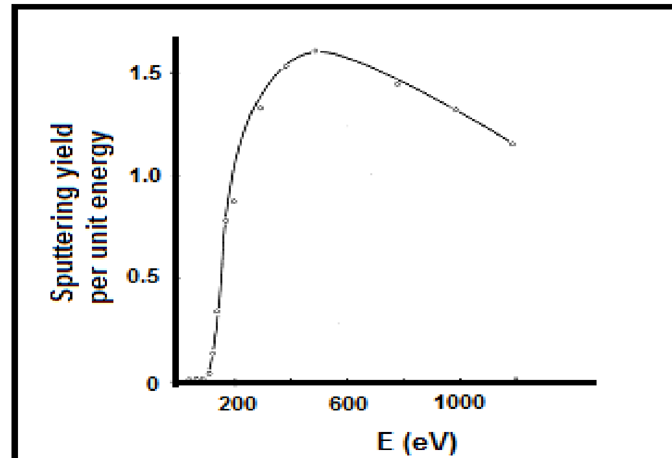

Figure 2.2 Variation of the sputtering yield per unit energy input for argon with ion energy [5].

According to the predictions of the sputtering target kinetics [5] the sputtering yield increases linearly up to 1keV and after that it is fairly constant. If so, then sputtering yield per unit energy should be a constant and this seems to be the case below 100 eV (**Fig. 2.2**) and after 1keV, the ratio falls with increasing energy. It is clear from the **Fig. 2.2** that above 1keV and below 100eV; it is not expected to sputter very rapidly. In practice a lower limit of 500V is used to achieve adequate current density (0.1-2.0 mA cm^{-2}) and the upper limit above 5kV is rarely been used.

2.2 DC planar magnetron set-up

A cylindrical vacuum chamber made of SS 304 mounted with a planar magnetron of target diameter 75 mm is used as the deposition setup. The diameter of the chamber was 350 mm and the length was 400 mm. The photograph of the device with the accessories for the

pumping, pressure measurement, and plasma diagnostics is shown in the **Fig. 2.3** and the schematic diagram of the set up is shown in the **Fig.2.4**.

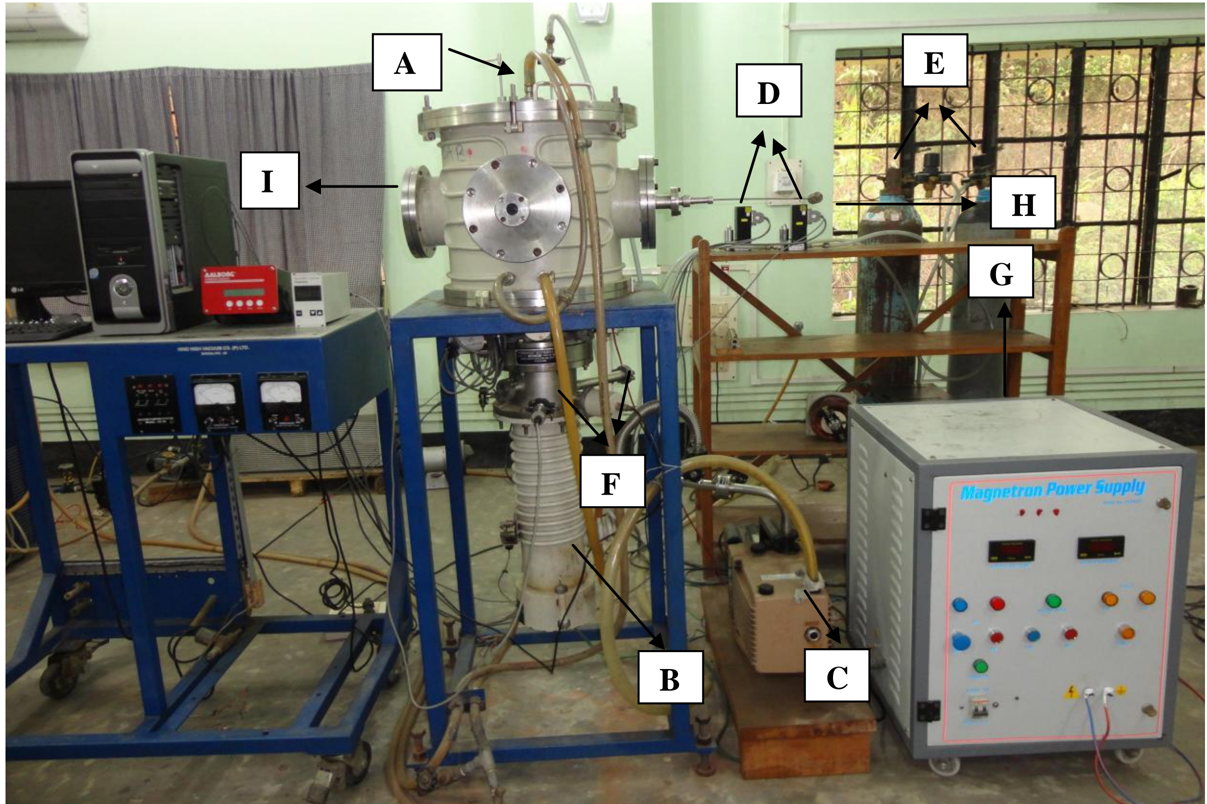

Fig. 2.3: Photograph of the deposition chamber, with the attached display panel of the magnetron bias power supplies. (A) Planar magnetron (B) Diffusion pump (C) Rotary pump (D) DFC (E) Gas cylinder (F) Pressure gauges (G) Planar magnetron power supply (H) Langmuir probe (I) Optical emission spectroscopy port

2.2.1 Vacuum chamber and accessories

The chamber had an approximate volume of 30 liters and is pumped with a combination of diffusion pump (Make: Hind High Vacuum, Banglore, India; Model: ULK-06 1000 lps) backed by a rotary pump (Make: Hind High Vacuum, Banglore, India; Model: ULK-06 585 l/min). A Baffle valve is provided to hinder the entry of oil vapors to the chamber during its

operation. A gate valve is provided on the inlet of the diffusion pump to maintain the low pressure inside the chamber while the chamber was kept idle. The maximum base pressure

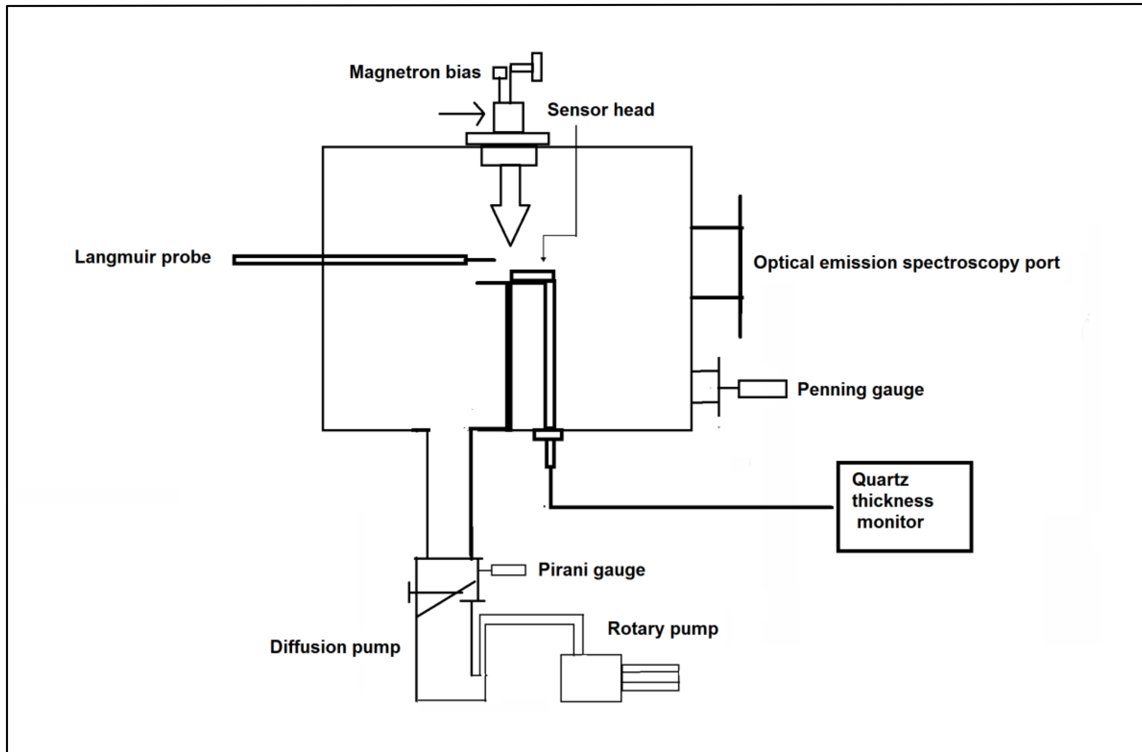

Figure 2.4 Schematic diagram of DC planar magnetron set up used for deposition

attained is 1×10^{-6} mbar. The pressure is measured using Penning and Pirani gauges and a capacitive manometer attached to one of the axial ports. Argon gas of high purity (99.99%) is used as the sputtering gas for the magnetron targets. For the reactive deposition, the reactive gas such as nitrogen and oxygen are introduced from one of the axial ports. It is done in order to minimize the target poisoning effect [6]. All the gases are introduced into the deposition chamber using gas flow controllers at suitable flow rates to maintain the operating pressure. In one set of experiment hydrogen is also used as the sputtering gas along the argon magnetron discharge. A deposition rate cum thickness monitor (DTM 101,

Hind High Vacuum) is mounted on one of the axial ports and could be positioned at various locations below the magnetron at the substrate plane to measure the deposition rate directly as a function of the various operating parameters. The deposition rate measurement is useful to determine the optimum operating parameters of the magnetron.

2.2.2 The planar magnetron and substrates

The planar magnetron used for sputtering the target material is mounted on the vertical port. Targets of diameter 75 mm and approximate thickness 5 mm are mounted on the magnetron cathode. The photograph of the planar magnetron is given in **Fig.2.5**.

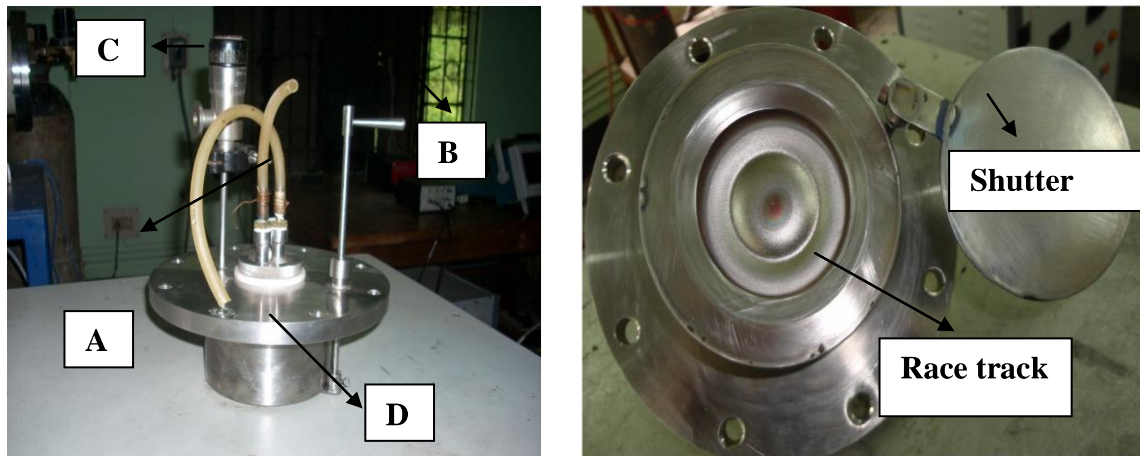

(a) **(b)**

Figure 2.5(a) Photograph of the planar magnetron, with the attached display panel of (A) Water inlet (B) Shutter (C) Sputtering gas inlet (D) Biasing port (b) Normal view of the planar magnetron. One can easily notice the race-track formed on the target surface.

For the deposition experiments conducted in the study, metallic targets of Titanium (99.99% purity), Chromium (99.95% purity) and Copper (99.95% purity) are used as the magnetron targets and operated in the DC mode (see **Fig. 2.6**). The magnetron is provided with a mechanical shutter positioned in front of the target. When the magnetron is operated

in the ‘closed state’ the entire sputtered flux is deposited on the surface of the shutter and only by turning the shutter by more than 90^0 the magnetron could be brought into an ‘open state’ such that the deposition can be done on the experimental substrate.

Before commencing the deposition, the magnetron is operated for a few minutes with the shutter in the closed state to sputter off any possible oxide layers formed over the target. A stainless steel disk of diameter 80mm is used as a substrate holder mounted from one of the ports of the chamber using suitable vacuum feed-through. The substrate holder could be positioned at various locations below the magnetron target plane during deposition.

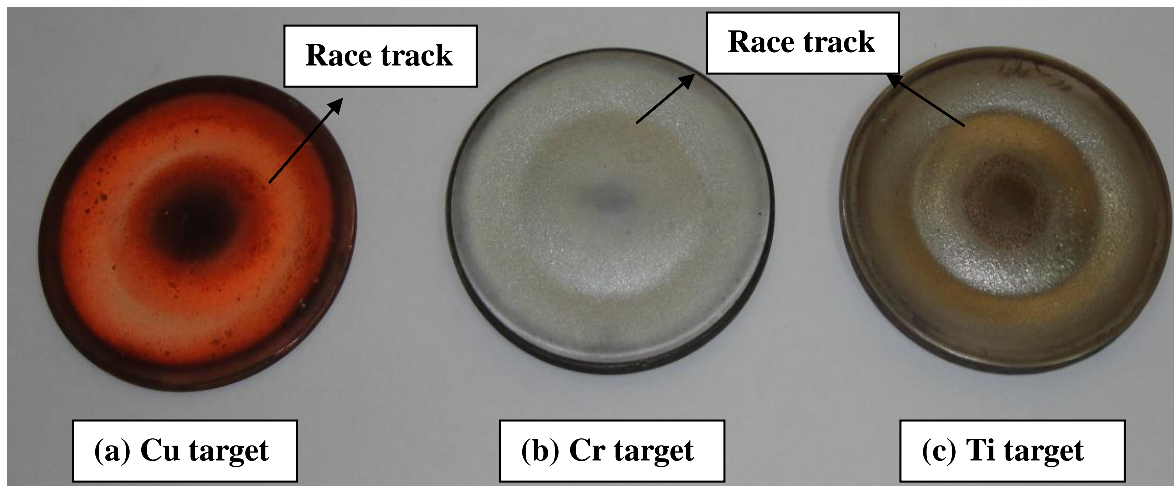

Figure 2.6 Photograph of the planar magnetron targets used in the various experiments of this investigation.

The magnetron is to be operated in the DC mode and the bias power supply is designed accordingly. The specifications of the DC supply used are as follows.

Voltage range: 0 to -1000 V

Current range: 0 to 3A

2.2.3 Calculating the pumping speed and flow rate of gas flow controller

For a chamber made up of electro-polished SS 304 of effective surface area (A) 4×10^4 cm^2 and out gassing rate (R) of 4.3×10^{-9} mbar ls^{-1}cm^{-2} [7], the total gas load (Q) is given by,

$$Q = R\times A \tag{2.2}$$

The required pumping speed (S) is defined as [8],

$$S = \frac{Q}{P} \tag{2.3}$$

with P is the base pressure in the chamber. For typical magnetron operation a base pressure of 1.0×10^{-6} mbar is required. Then, using the Eq. (2.3) the pumping speed of the chamber is calculated as 172 ls^{-1}. But the efficiency of a pump decreases with increasing pressure in the chamber and the pumping speed is significantly lower at the working pressure (1-5×10^{-3} mbar) condition applicable for magnetron operation. Taking into accounts various other factors such as secondary out gassing source etc., the effective pumping speed should be at least 2-3 times of the calculated value. In practice for such chamber dimension, a diffusion pump of 1000 ls^{-1} capacity is sufficient enough to achieve such working pressure. Such pump cannot be exposed to atmospheric pressure as the exhaust pressure need to be in molecular flow regime and the additional drag on the fan is reduced. Hence such fore pump is backed by a rotary pump connected in series with the pump and the chamber. The condition of constant throughput is given as,

$$S_1P_1 = S_2P_2 \tag{2.4}$$

Here, $S_1 = 172$ ls^{-1} and $P_1 = 3\times10^{-3}$ mbar. Taking into account the value of lower pressure attained by such pump (5×10^{-2} mbar) as P_2, the required pumping speed for the backing

pump is calculated as, 10.32 ls^{-1}.

The gas flow rate into the chamber through the mass flow controller is balanced by the pumping speed giving stable chamber pressure and in this respect the Eq. (2.4) becomes,

$$S_{MFC} \times P_{atm} = S_{pump} \times P_{Chamber} \quad (2.5)$$

With $P_{atm} = 1000\,\text{mbar}$, $S_{pump} = 172\,\text{ls}^{-1}$ and $P_{Chamber} = 5\times10^{-3}\,\text{mbar}$, the required flow rate,

$S_{MFC} = 8.6\times10^{-4}\,\text{ls}^{-1} = 50\,\text{SCCM}$.

In practice the required total gas flow rate to maintain the chamber of the mentioned dimension at 5×10^{-3} mbar is 15 SCCM.

2.3 Plasma diagnostic tools and techniques

The diagnostics mainly used in this experimental work are the Langmuir probe (Cylindrical as well as Plane), Optical emission spectrometer (OES) and Ion Acoustic Waves (IAW). The Langmuir probe is used for determination of the plasma parameters like density and temperature. The IAW diagnostic is used to determine the relative density of negative ions present in such discharge using the phase velocity of the ion acoustic waves. Optical emission spectroscopy is performed to determine the degree of ionization and dissociation of various species of the plasma using the relative intensity of emission line present in the OES spectrograph.

2.3.1 Langmuir Probe

A Langmuir probe is a device named after physicist Irving Langmuir and used to determine the physical properties of the plasma such as the electron temperature, electron density, and electric potential. It works by inserting one or more electrodes into plasma. A constant or time -varying electric potential is applied between the various electrodes or between them

and the surrounding vessel. The measured currents and potentials in this system determine the physical properties of the plasma. Cylindrical, spherical as well as planar Langmuir probe are used for the measurement of plasma parameters. The electrode that is inserted in the plasma is commonly known as the 'probe tip'. For cylindrical Langmuir probe, a tungsten filament of length of 3.0 mm and a radius of 0.1 mm and for the planar Langmuir probe a stainless steel disc of diameter 6mm are used as the probe tip. The probe dimension took into account the following considerations,

(1) It is ensured that the calculated deBye length (λ_D) for a plasma with electron temperature 1-5eV and density 10^{15} m^{-3} is smaller than the probe radius.

(2) The mean free path of collision of the electrons and ions is much larger than the Langmuir probe radius.

The electric connection with the probe tip is ensured with a Teflon coated conducting wire placed inside a stainless steel cylindrical pipe of diameter 7mm. Since the magnetron plasma contained in it the metallic species sputtered from the target, the probe tip upon exposure to the plasma had the tendency to get coated with a conducting film and consequently increasing the effective collecting area, an important parameter for calculating the plasma density. To overcome this concern, the probe tip is fixed at the end of a shaft using holders with a Teflon cap. The Teflon cap insures that the charge collecting area of the probe does not change significantly during prolonged deposition. The block diagram of the modified probe holder is shown in **Fig. 2.7**.This technique ensures that the charge collecting area of the probe is almost invariant during deposition [9]. The Langmuir

probe is suitably biased (-80 V to +80 V) to the (*I*–*V*) characteristic with the electron and the ion saturation region.

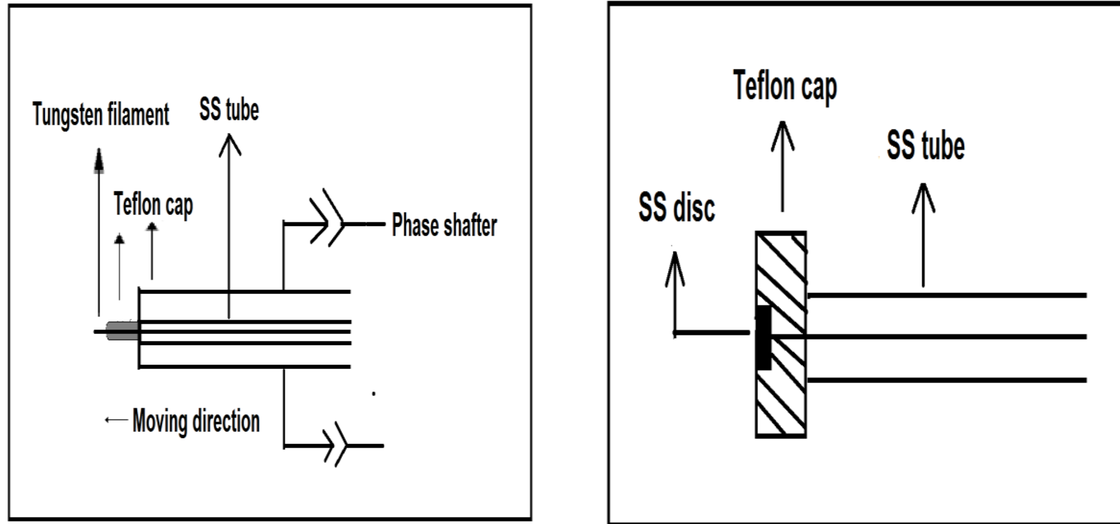

Figure 2.7 Schematic block diagram of the (a) Cylindrical Langmuir probe (b) Planar Langmuir probe

A typical (*I*–*V*) characteristic curve of the magnetron plasma obtained from the Langmuir probe is sketched in the **Fig. 2.8.** Referring to the probe characteristic of the **Fig. 2.8** we see that in the region where the probe potential (V_b) is above the plasma space potential (V_p), the collected current has contribution from the electrons only and the ions are repelled, while in the magnified region just the opposite occurs and the collected ion current reaches a saturation value (I_{is}). By evaluating the slope of the *I-V* characteristic in the transition region the electron temperature T_e is obtained. By measuring the ion or electron saturation current and the substituting the value of electron temperature the density can be computed. The expression of the ion saturation current (I_{is}), electron saturation current (I_{es}), floating

potential (V_f) and plasma potential (V_p) is mentioned below [10]. Also, the procedure to calculate the ion density in the presence of two or more gases in the plasma is explained.

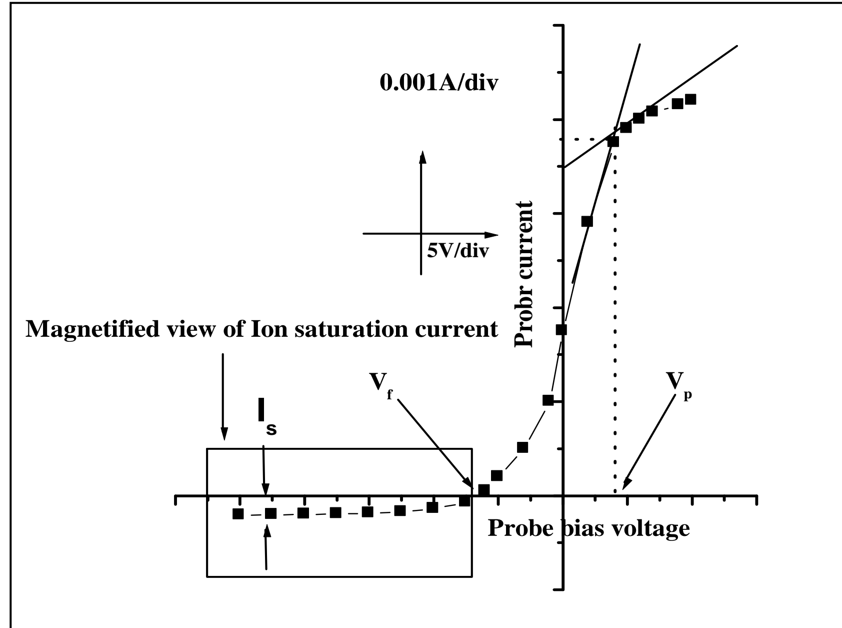

Figure 2.8 Typical Langmuir probe I-V characteristics is traced and the values of V_p (plasma potential) V_f (floating potential) and the ion saturation current can be easily obtained from the figure.

2.3.1(a) The electron saturation current

The electron saturation current region is the region where all the electrons are collected by the probe. The electron saturation (I_{es}) is given by the expression,

$$I_{es} = -n_e eA(\frac{k_B T_e}{2\pi m_e})^{1/2} \tag{2.6}$$

2.3.1(b) The ion saturation current

In order to obtain the ion saturation value the probe voltage must be negative enough to repeal all the electrons. For that the probe voltage should have a magnitude near $k_B T_e / e$, the electron energy. The sheath criterion requires that ions arriving at the periphery of the

probe sheath be accelerated towards the probe tip with Bohm velocity [11]. With all these conditions the ion saturation current expression becomes,

$$I_{is} = 0.6 n_i e A \sqrt{\frac{k_B T_e}{m_i}} \tag{2.7}$$

where m_i is ion mass. The net probe current is given by,

$$I(v) = I_{is} - n_e e A \sqrt{\frac{k_B T_e}{2\pi m_e}} \exp\left(\frac{eV}{k_B T_e}\right) \tag{2.8}$$

where $V = V_b - V_p$. Thus, the electron current increases exponentially until the probe voltage equals to the plasma potential.

2.3.1(c) Floating potential

Floating potential is defined as the value of biasing potential when the electron and ion currents are equal and the net probe current ($I(V)$) is zero. From the Eq. (2.8) the value of the floating potential (V_f) is given by,

$$V_f = V_p - \sqrt{\frac{k_B T_e}{m_i}} \ln\left(\frac{m_i}{2.3 m_e}\right) \tag{2.9}$$

2.3.1(d) Mean ion mass (M_i) and ion density measurement in multi-component plasma

In the reactive sputtering when reactive gas such as nitrogen is added, in addition to Ar^+ ions the plasma will consists of various other types of positive ions such as N^+, N_2^+, N_3^+, N_4^+ etc. Similar condition prevails when nitrogen is substituted by hydrogen in magnetron discharge. Hydrogen added argon plasma consists of various hydrogen containing species like H^+, H_2^+, H_3^+, ArH^+ etc. Due to the presence of these ionic species it is not possible to

determine the density of each ion individually using the Langmuir probe. Also the use of argon ion mass in the calculation for ion density is no longer possible in this case. The possible way to determine the densities of ions in such plasma is to divide the ions present in the discharge into two groups based on their ionic masses [12-14]. In that case rather than calculating the density of each ion, the density of each group can be calculated. For example the hydrogen added argon plasma can be divided into two ion groups: a heavy group of argon like ions (Ar^+ and ArH^+ ions) of mass 40 a.m.u and a light ion group of hydrogen like ions (H^+, H_2^+, H_3^+) having mass 2 a.m.u. The group density is represented by the mean value of masses known as the 'mean ion mass'. To determine the density of ions belonging to each group at different discharge conditions the procedure is as followed:

(1) From the Langmuir probe $I-V$ characteristics the value of n_e, T_e and I_{is} are determined for the pristine argon plasma at various deposition conditions.

(2) The values of n'_e, T'_e and I_{is}' are determined for hydrogen or nitrogen added argon plasma at the same deposition conditions.

(3) Comparing the values of plasma parameters of the later with pristine argon plasma using the Eq. (2.7), the value of ion mass for multi-component plasma at a particular deposition condition is determined. Since we are comparing it with the pristine argon plasma having ion mass 40 a.m.u, the obtained value of mean ion mass is the representative of the heavy ion group. For example, at a particular deposition condition for pristine argon plasma the value of ion mass m_i = 40 a.m.u. Substituting the values of electron density, temperature and ion saturation current from the Langmuir probe $I-V$ characteristics for

hydrogen or nitrogen added argon plasma at the same condition in the Eq. (2.7) and comparing it with the pristine argon plasma we have,

$$M_i = \frac{40 \times T_e^{'}}{T_e} \left(\frac{n_e^{'} I_{is}^{'}}{n_e I_{is}}\right)^2 \tag{2.10}$$

where M_i is the mean ion mass for hydrogen or nitrogen added argon plasma and $n^{'}_e$, $T^{'}_e$ and $I_{is}^{'}$ are the values of electron density, temperature and ion saturation current of the same. It will be found in the subsequent chapters that the values of mean ion mass decrease with addition of gases like nitrogen or hydrogen in the argon plasma.

(4) Once the mean ion mass is determined comparing it with the values of pristine argon plasma, the contribution of each group of ions in the discharge can be easily evaluated using the following equation,

$$n_{heavy} = \frac{n_i (= n_e)}{40} \times M_i \tag{2.11}$$

where n_e is the value of electron density of pristine argon plasma at the same deposition condition. It is worthwhile to mention that in the experiments described in the Chapter 3, 4, and 5, the cylindrical Langmuir probe measurements are taken in the downstream region 80 mm from the cathode, which is 10 mm above the substrate. We took the Langmuir probe measurement near the substrate plane, keeping in mind that the electron and ion density in the vicinity of the substrate can significantly affect the physical properties of the deposited film [15].

2.3.2 Ion acoustic wave (IAW) diagnostic

2.3.2(a) Method of wave excitation

In order to study the wave propagation in the laboratory plasma, an infinitely homogeneous collision less plasma must be created. Inserting a local density perturbation, ion acoustic wave is excited in such plasma. There exist various methods to excite the ion acoustic wave in plasma. The grid excitation mechanism was used by Wong et *al.* [16], and Hatto and Sato et *al.* [17] to study the linear propagation of the ion acoustic wave by exciting lower density perturbation $(\frac{\partial n_e}{n_e} < 5\%)$. Watatanabe [18] and Okustu et *al.* [19] extended this technique to study non-linear waves. They found that when density perturbation of sufficient magnitude $(\frac{\partial n_e}{n_e} \approx 10\%)$ is employed, the ion acoustic wave may evolve into soliton.

In the grid excitation method the ion acoustic waves are excited by producing a density perturbation with a conducting launch grid immersed in the plasma. The stainless steel grid has 20 meshes per centimeter and has a transparency of 70%. The inter-wire spacing of the grid is ensured greater than the deBye length (λ_d). In the grid excitation method, the grid is initially biased negatively with respect to plasma potential at time $\tau < 0$. At time zero, a small positive step potential $(\Delta\phi)$ is applied on the grid. Then the grid biased changed from $-V$ to $-V + \Delta\phi$. As the charge collection region (> 10 λ_D) is a significant portion of the inter-wire spacing, a modulation of the grid bias will produce a varying amount of absorption that results small density perturbation in the grid vicinity and then, it propagates down the plasma column [20]. Since the perturbed ion and electron densities in the ion acoustic waves are very nearly equal ($\partial n_e = \partial n_i$) and the electron current ($\partial n_e\, e\, v_{es}$) is much larger than the ion current ($\partial n_i\, e\, v_{is}$), the most sensitive detection of the ion acoustic waves

by a probe is achieved when it is biased positively to collect the electron saturation current. Here, v_{es} and v_{es} are the thermal velocities of the electron and ions respectively. Another advantage of biasing the receiving probe at or above the plasma potential is the resulting fast probe response due to the electron-rich sheath surrounding the probe permits good

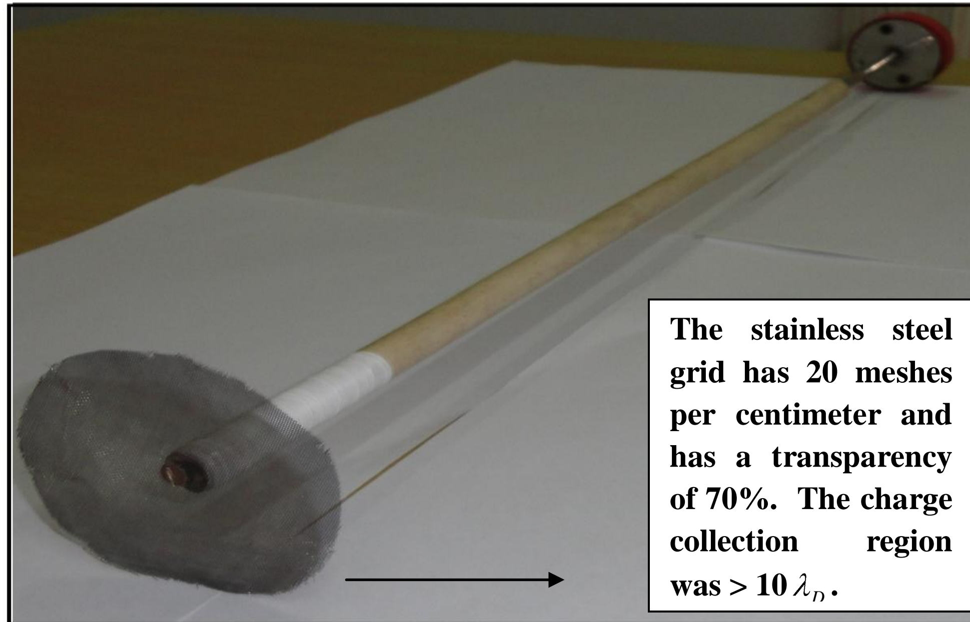

Figure 2.9 Photograph of the ion acoustic wave exciting grid.

communication between the plasma proper and the probe surface. The density perturbations ($\partial n_e/n_e$) are detected using an axially adjustable planar Langmuir probe (of 6 mm diameter) biased positively with respect to the plasma potential and placed in front of the center of the mesh. The photograph of the stainless steel grid with fine messes is this in shown in **Fig. 2.9**.

2.3.2 (b) The Wave-launcher

The typical discharge condition in this study for bulk region of the DC planar magnetron device where the wave is launched is given as, electron density (n_e) = 10^8–10^9 cm^{-3},

electron temperature (T_e) = 4-6eV and average ion temperature (T_i) ~ 0.1 eV. The plasma is assumed to be homogeneous in the experimental region. The noise to background density ratio was below 1% as determined by a probe biased at 30V [21]. Density perturbations that evolved into the waves are excited by applying sinusoidal voltages to a fine mess stainless steel grid that is inserted in the device. The amplitude of the applied signal is chosen as $|\Delta\phi| < 6.5V$ such that $(\frac{\partial n_e}{n_e} < 10\%)$ and the repetition frequency is fixed at 50-100 kHz [22]. The applied frequency is chosen such that its value is about one tenth of the ion plasma frequency.

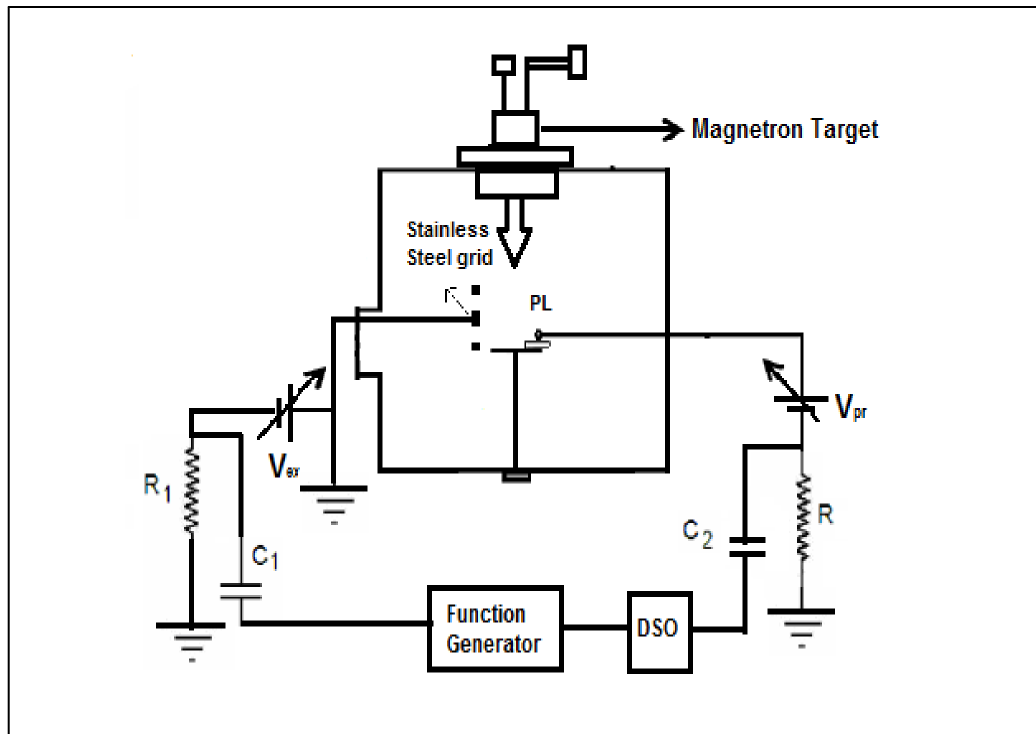

Figure 2.10 Schematic diagram of the wave Launching set up. V_{ex} — amplitude of applied voltage signal to the stainless steel, V_{pr} — Langmuir probe biasing voltage, PL — Plane Langmuir probe, DSO — Digital oscilloscope

For detecting the propagating signal, the probe is biased positively with respect to plasma potential in order to detect perturbation in the electron saturation current. The travelling wave train reaches the movable Langmuir probe in a time longer than the duration of the burst to facilitate a positive identification of the propagating signal. The perturbations in current are passed through a resistor to the ground and the resulting voltage perturbations are displayed on a digital oscilloscope that is externally triggered by the signal generator. A data acquisition software is used to send the experimental data to a computer. The time-of-flight technique is used to measure the phase velocities of the excited ion acoustic waves. The schematic diagram of the experimental set-up is given in the **Fig. 2.10**.

2.3.3 Optical emission spectroscopy (OES)

Based on the radiation emitted or absorbed it is possible to identify and determine the structure of atoms and molecules. This procedure is known as Optical emission spectroscopy (OES). The lines from the gaseous discharge are found to consist of discrete lines and bands. The lines and bands correspond to the transition between the characteristic energy levels of atoms or molecules. The physical properties of the plasma affect the intensity and wavelength distribution of such transitions in various ways, such as the line broadening, shift of spectral lines etc [23, 24]. The intensity $I(p,q)$ of a spectral line arising from transition between two bound level *'p'* and *'q'* is given by [24],

$$I(p,q) = \frac{1}{4\pi} \int n(p) A(p,q) h(p,q) ds \tag{2.12}$$

where, $A(p,q) =$ Atomic transition probability and $h(p,q) =$ Photon energy.

For excited atoms, molecules and ions in low temperature plasma with very low pressure $(<1\ \text{Pa})$ and low ionization ratio $(<10^{-5})$ the corona model of emission spectroscopy is

applicable. This is because under such conditions collision processes other than the electron impact excitation from ground state species and the spontaneous radiations from the excited species are not important, and the density of meta-stables is low enough to make a significant contribution to the excitation of excited species [25]. Under such conditions, the emission intensity from an excited state (p) is proportional to its density,

$$I(p,q) \propto A(p,q) n_p \tag{2.13}$$

where n_p refers to the population density in the in the excited state (p). With such a model, by selecting two excited levels with similar excitation threshold energies, the obtained line ratio is an indicative of the plasma parameters such as degree of ionization, degree of dissociation etc [12, 13].

2.3.4 Experimental set-up for optical emission intensity measurement

The optical emission spectroscopic measurement is performed using a ½ m digikrom spectrometer (CVI Laser Corp, USA. Digikrom Model DK 480).The system consists of a photo multiplier tube (PMT: Model AD110, wavelength range: 185-930nm) and a grating with 1200 grooves/mm for detection in the region λ = (400 – 850) nm. The entrance slit and exit slit of mono-chromator are adjusted at 20 Å to obtain an acceptable spectral resolution sufficient to detect the emission lines. The emissions are collected by a light collecting system (LCS) through the optical fiber (F) that is put on the glass window approximately at a vertical distance of 8 cm from the target in the downward region and kept in a manner to avoid the background radiation as well as to detect maximum emission. The light collecting system with the optical fiber (LCSF) is further aided by a plano-convex lens (diameter 2mm, focal length 3 cm) and a silica fiber of 1.0 mm core (numerical

aperture:0.22). The view subtended by this LCS was parallel to the discharge column grazing the vicinity of the substrate and always collected radiations from the fixed location. The schematic diagram of the experimental set-up used for OES study is given in the **Fig. 2.11**.

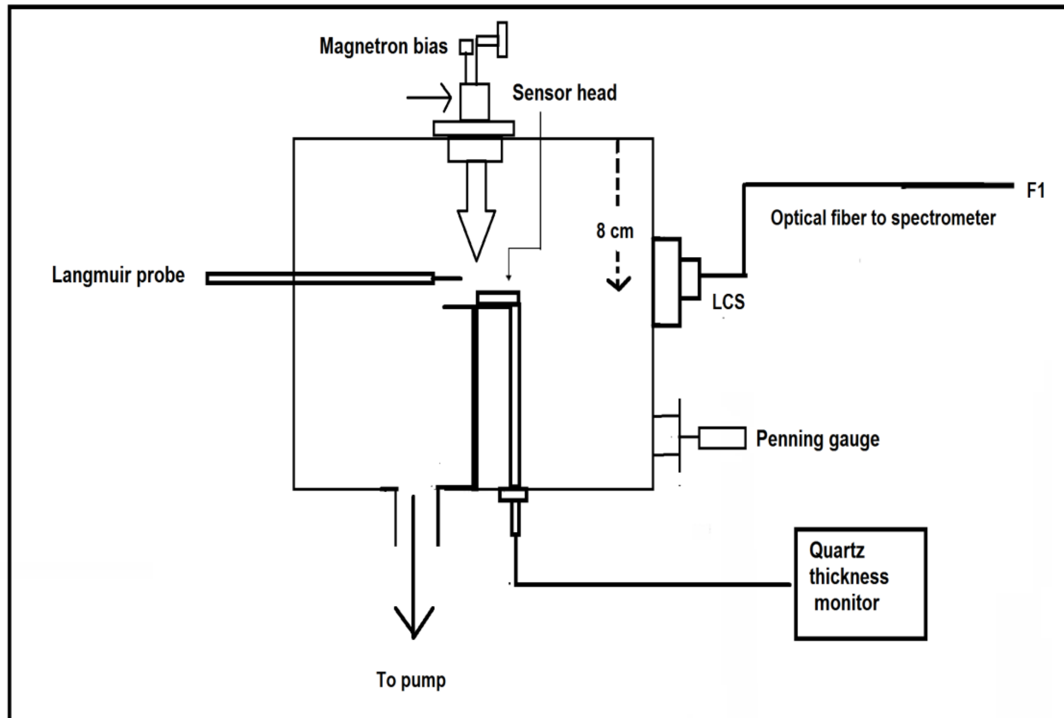

Figure 2.11 Schematic diagram of the experimental set-up for optical emission spectroscopy measurement.

2.3.5 Measurement of deposition rate: Quartz Crystal Thickness Monitor

The quartz thickness monitor operates on a principle called the Piezo electric effect. When an electric potential is applied to a quartz crystal it vibrates at its natural frequency. At a constant temperature this frequency remains stable unless the mass of the crystal change. Depositing a thin film on the crystal surface will change the mass of the crystal. The increase in mass from the deposition causes the resonant frequency of the crystal to

decrease. Such changes are easily detected electronically by the sensors and the sensor performs appropriate mathematical functions to convert the frequency data to thickness data, both the instantaneous rate and calculated thickness. Such sensors not only read and display the rate and thickness data, but also provide outputs for other deposition system elements. It has an analog drive signal in a closed loop technique based on the rate data and thus able to maintain a preset rate during deposition. It also has a source shutter triggered to close when the preset final thickness is achieved. Since the heat also changes the frequency of vibration of the crystal, the monitor must be cooled to provide accurate reading. The photograph of the quartz thickness monitor is given in the **Fig. 2.12**.

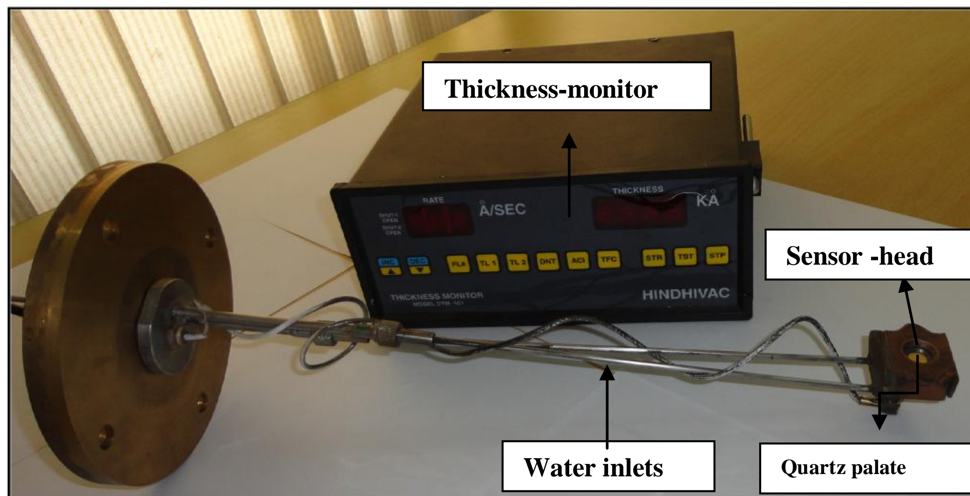

Figure 2.12 Photograph of the quartz thickness-monitor (DTM-101)

2.4 Initial plasma characterization experiments

2.4.1. I/V characteristics acquired at various operating conditions

The Langmuir probe I-V characteristics are acquired for (a) different magnetron targets at varying working pressures and input powers for the hydrogen additive argon plasma. Here, the working pressure is varied by adding hydrogen keeping the argon flow rate same. (b)

different working pressures keeping the nitrogen to argon partial pressure ratio same in the nitrogen added argon plasma with titanium as the magnetron target (c) different oxygen partial pressures in the oxygen additive argon plasma with titanium as the magnetron target. The plasma parameters are evaluated as mentioned in section 2.3.1 and discussed in the subsequent chapters (Chapter 3 to Chapter 5). **Fig. 2.13** shows the pattern of Langmuir probe I-V characteristics for condition (a). For the same discharge condition the plasma density and electron saturation currents are observed to have a higher magnitude for Ti target than the Cu and Cr target. This is due to the difference in secondary electron yield (γ) for the materials with $\gamma_{Ti} > \gamma_{Cr} > \gamma_{Cu}$ for a given discharge voltage [26].

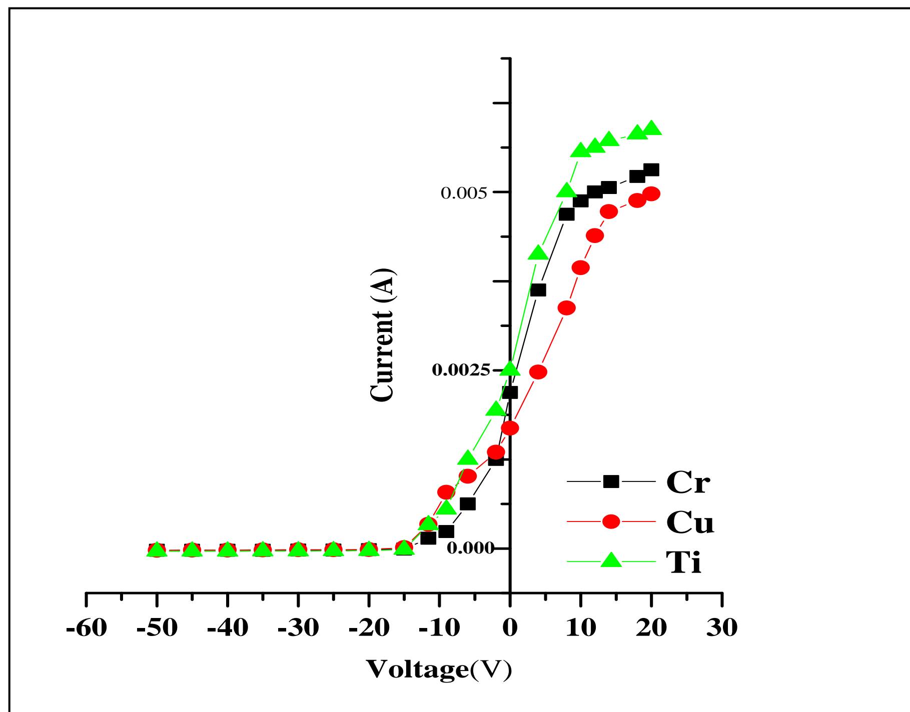

Figure 2.13 Typical Langmuir probe I-V characteristics traced at working pressure 4×10^{-1} Pa for the hydrogen added argon plasma for titanium, chromium and copper magnetron target. The input power (P) = 300W for each target.

The pattern of the Langmuir probe I-V as a function of hydrogen partial pressure for Cr target is shown in **Fig. 2.14**. It is again observed that introduction of hydrogen in argon decreases the plasma density and electron saturation currents. On the other hand the gradual addition of oxygen in the argon discharge will create and enhance the negative ion density in the background of otherwise positive ion-electron plasma [27]. With the introduction of negative ions the shapes of Langmuir probe I-V characteristics and as such, the magnitudes of plasma parameters change. Here, electrons are replaced with negative ions having thermal velocities and therefore mobility close to that of positive ions. Thus the electron saturation current decreases. A review and interpretation of probe diagnostic technique in negative ion plasma is elaborately explained by Amemiya [28] et *al*. A detail evaluation of the plasma parameters for such plasmas will be given in the Chapter 4.

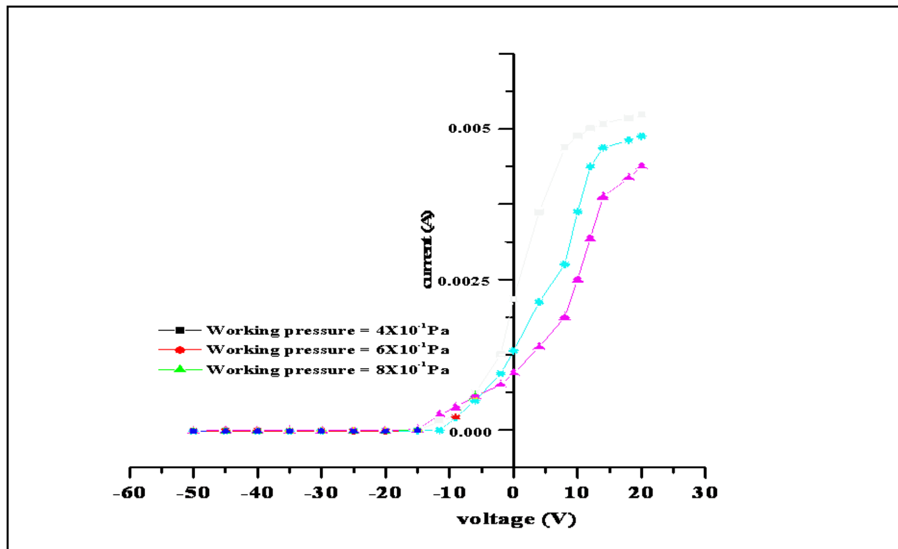

Fig. 2.14 Typical Langmuir probe I-V characteristics traced with input power (P) = 300W for hydrogen added argon plasma for chromium magnetron target. The parameter is working pressure and argon partial pressure (3.7×10^{-1} Pa) was kept constant.

2.4.2. Measurement of optical emission line intensity

The emission from the discharge is monitored for the experimental conditions mentioned in 2.4.1(a)-2.4.1(c).The collected spectra is shown in the **Fig. 2.15(a)** to **Fig. 2.15(c)**. The procedure to estimate the value of the degree of ionization and degree of dissociation of the selected species based on the above spectrograph is mentioned in Chapter 3 and Chapter 5.

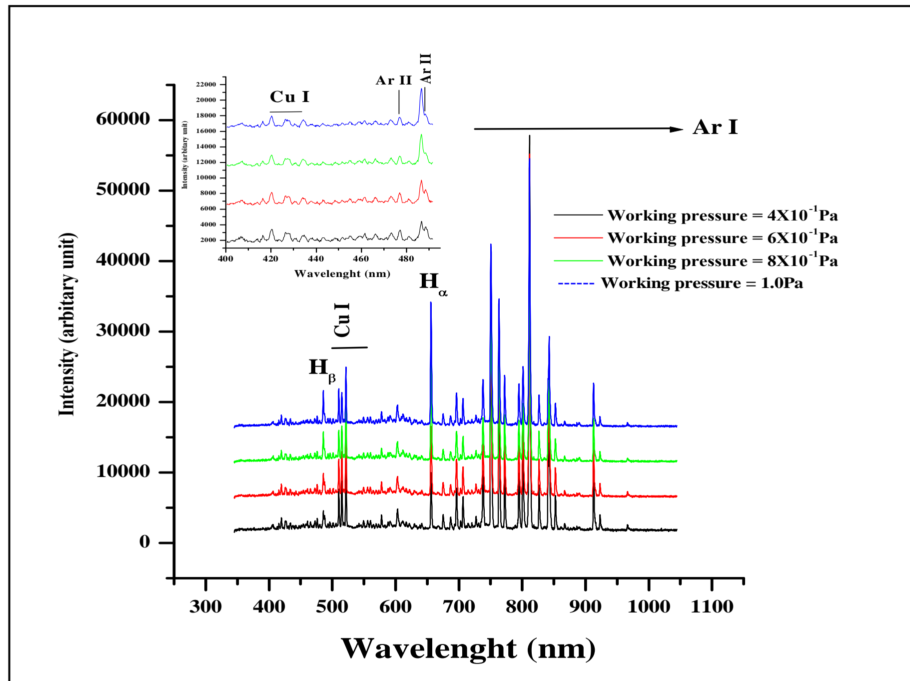

Figure 2.15 (a) The emission lines of the spectra collected for the hydrogen added argon plasma at different working pressure. The parameter is working pressure and the partial pressure for argon (3.7×10^{-1} Pa) was kept constant. The emitting species are identified by comparing with NIST database.

In the **Fig. 2.15(a)** the intensity variation of the species of Ar I [3s^2 3p^5 (2 $p^0_{3/2}$) 4s]$\rightarrow$[3s^2 3p^5 (2 $p^0_{1/2}$) 4p] at 696.45 nm, 738.39 nm, 801.47 nm, 811.53 nm; Ar I [3s^2 3p^5 (2 $p^0_{1/2}$) 4s]$\rightarrow$[3s^2 3p^5 (2 $p^0_{1/2}$) 4p] at 751.46 nm, 763.51 nm, 772.37 nm, 794.81 nm, 826.45 nm, 840.42 nm, 852.14 nm; Ar II [3s^2 3p^4 (^3p)4s]$\rightarrow$[3s^2 3p^4 (^3p)4p] at 434.80 nm, 454.15 nm,

472.68 nm, 476.48 nm, 480.60 nm; H_α line (656.28 nm) and H_β line (487.54 nm); Cu I at 510.554 nm, 515.324 nm, 521.820 nm, 529.252 nm are shown. It is observed that the intensity profile of Ar and Cu transitions follow the discharge current, i.e. intensity of all these transitions peaked when discharge current is the maximum. The intensity of H_α line increases rapidly in comparison to the intensity of H_β line. The energy required for direct excitation by electron from the ground state is 12.1 eV corresponding to to H_α line and for H_β excitation it is 12.7 eV [29]. This explains the faster increase in the intensity of H_α line than the intensity of H_β line.

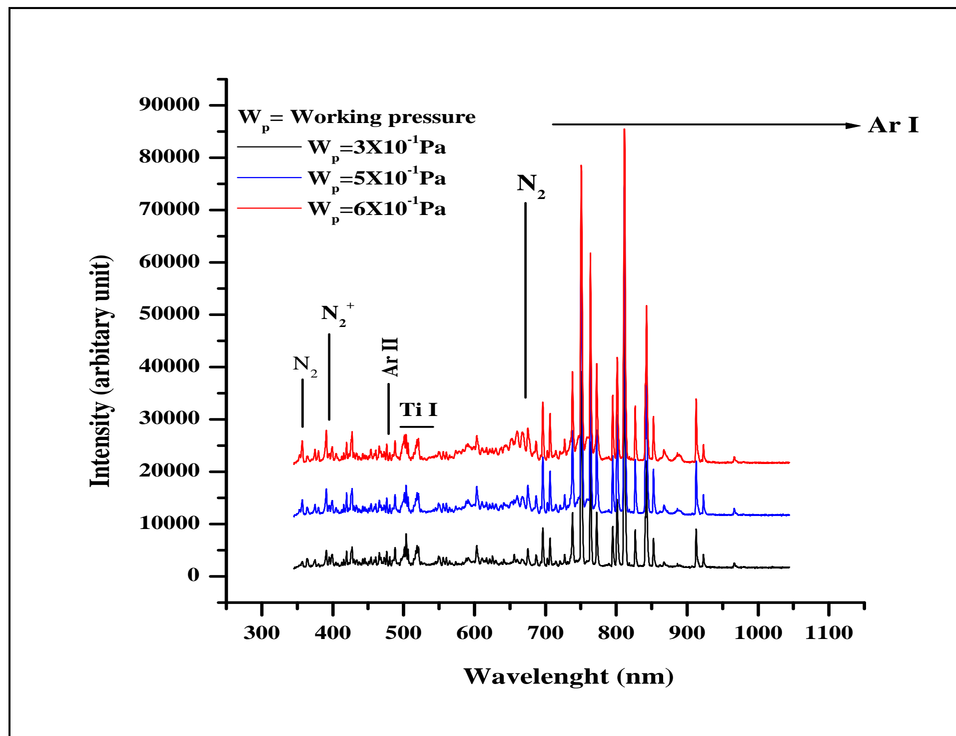

Figure 2.15 (b) The emission lines of the spectra collected for the nitrogen added argon plasma at different working pressure. The nitrogen to argon flow ratio is kept fixed. The emitting species were identified by comparing with NIST database. The variation in the relative intensities of Ar II and Ar I could be observed.

Similarly in the **Fig. 2.15(b)** intensity variation of the most prominent species of nitrogen such as N_2^+ ($B\,^2\Sigma_u^+ \rightarrow X\,^2\Sigma_g^+$) at 391.58 nm and N_2 ($C\,^3\Pi_u \rightarrow B^3\Pi_g$) at 356.85 nm, Ti I line at 499.5 nm, and 510.53 nm in the nitrogen added argon plasma are shown. Also in the **Fig. 2.15(c)** the gradual increase of intensity of the oxygen atomic lines O I [$2s^2$ $2p^3$ $(^4S^0)\,3s$] $\rightarrow$ [$2s^2$ $2p^3$ $(^4S^0)\,3p$] at 777 nm and 845 nm with increasing oxygen partial pressure in oxygen added argon magnetron discharge with Ti target can be seen easily. For the low-temperature plasmas with very low pressures (<1 Pa) and low ionization ratios ($<10^{-5}$) such as the DC planar magnetron discharge, the corona model is valid and is used to determine the plasma parameters [30-31].

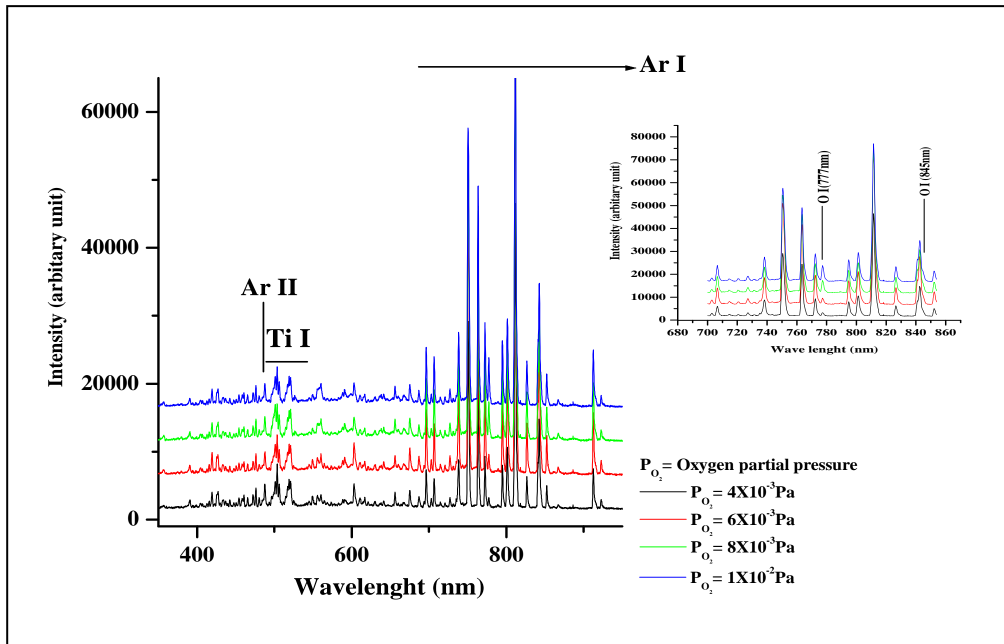

Figure 2.15 (c) The emission lines of the spectra collected for the oxygen added argon plasma at different oxygen partial pressure. The argon partial pressure is kept fixed at 8×10^{-2}Pa. The emitting species are identified by comparing with NIST database. The variation in the relative intensities O I line is observed.

2.5 Plasma nitriding experimental set-up

Plasma nitriding is plasma based surface hardening process that utilizes the nitrogen-hydrogen plasma for supplies of the ions, excited atoms and molecules as well as radicals for nitrogen incorporation into the iron and iron alloys [32]. The differences of the operating conditions between the two processes are mentioned in the **Table 2.1**. It is generally done in the abnormal glow region. In typical plasma nitriding condition the substrate is kept negatively biased between 400V to 800V having typical current density of 1.5 mA/cm^{-2} [33]. The ions from the plasma sheath boundary (i.e. negative glow) accelerated towards the cathode. On its way to the cathode the ions undergo charge exchange collision and also generate energetic neutrals. N_2^+ ions and energetic N_2 are the main active species in plasma nitriding (PN). Thus near the substrate surface by recombination of N_2^+ ions and dissociative recombination of energetic N_2 atomic nitrogen is effectively generated. The thermo- chemical diffusion of nitrogen atom in the surface of substrate causes the nitriding.

Table 2.1 Comparison of operating conditions of plasma nitriding and thin film deposition

	PN	Thin film deposition
- operating pressure	few mbar (1-5mbar)	10^{-3} mbar
- Gas mixtures	N_2/H_2	Ar/N_2 or O_2 or H_2
- Treatment duration	Tens of hours	hours
- Line of sight process	No	Yes
- Sample manipulation	No	Yes
- Temperature	400-560^{0}C	Room temperature to 450^{0}C
- Substrate bias	high	low

A high temperature is thus necessary so that nitrogen diffusion into the steel takes place. However, depending on the alloying element and stability of elements the nitriding temperature lies in the range of 250^0C to 600^0C [34]. The distance up to which nitrogen diffusion occurs is known as the diffusion zone and its depth is given by,

$$d = \sqrt{kDt\frac{[N]}{[X]}} \tag{2.14}$$

with [N] is the surface nitrogen content, [X] is the original concentration of the nitride forming element and D is the diffusion coefficient of atomic nitrogen [35].The diffusion zone consists of nitrogen in solid solution as long as the temperature dependent solubility limit is not exceeded. If it is exceeded, the nitrides and alloy formation occur. Depending on the alloying elements and their amounts iron nitrides, alloy nitrides and mixture of both can be found either on the grain boundary or within the grain boundary. This layer is known as the compound layer and when it forms, the diffusion zone can be found below the nitride layer [36]. The compound layer generally consists of mono phase layer such as the $\gamma^{'}Fe_2N$ or $\varepsilon Fe_{2-3}N$ or mixtures of both. The ε layer is best for wear and fatigue application. The $\gamma^{'}$ layer is somehow softer and wear resistant but is tougher and more forgiving in severe loading situation [36]. The formation of compound layer depends on the N_2 / H_2 gas composition as well as the treatment temperature. When the gas composition is such that nitrogen species are more, in that case treated surface contain multiphase layer $(\varepsilon + \gamma^{'})$ known popularly as the white layer. Plasma nitriding can inhibit the formation of white-layer and if needed can form a mono phase layer which may be either ε or $\gamma^{'}$ nature.

As per requirements a diffused layer can be generated or a mono-phase layer can be made available on top of the diffused layer. The role of hydrogen in plasma nitriding is to increase the sticking coefficient [37] of atomic nitrogen formed near the cathode surface. Plasma nitriding achieves repetitive metallurgical results and complete control of the nitrided layers. This control results in superior fatigue performance, wear resistance and hard layer ductility.

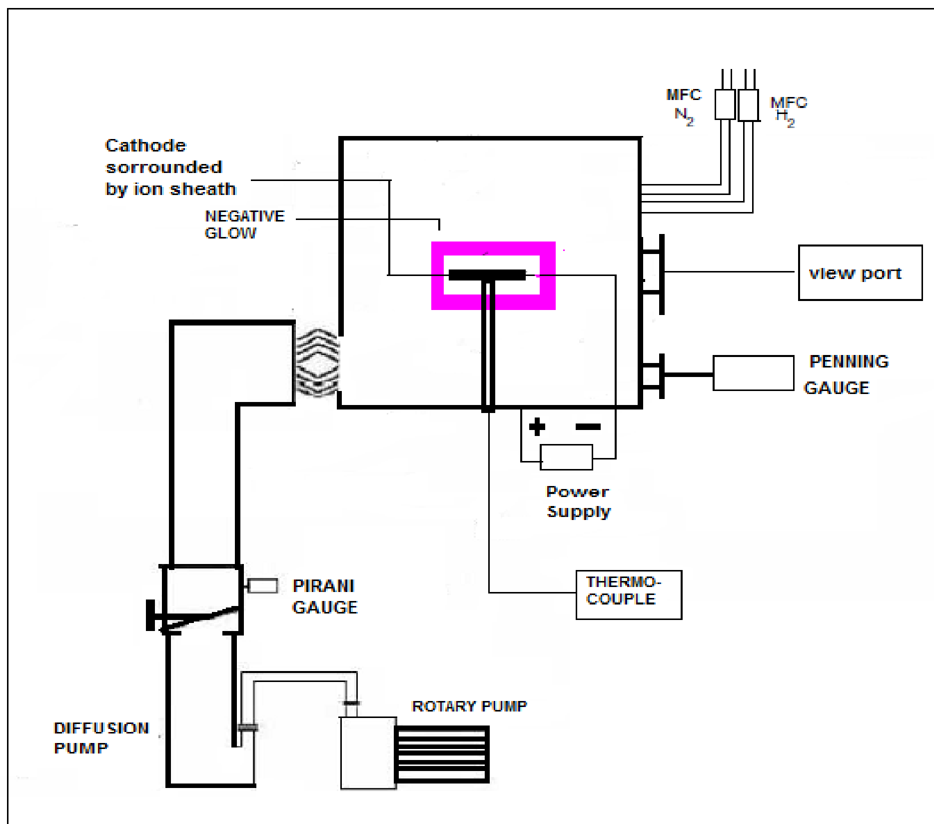

Figure 2.16 The experimental set-up for DC pulsed plasma nitriding. Pulsed plasma nitriding is done at fixed duty cycle of 80% and frequency of 50 kHz.

Moreover, the process ensures high dimensional stability, eliminates secondary operations, offers low operating-temperature capability and produces parts that retain surface finish. As the PN operates at very high pressure compared to planar magnetron sputtering, therefore it

does not require diffusion pump. The schematic diagram of the plasma nitriding set up is given in **Fig. 2.16**.The rotary pump (Make: Hind High Vacuum, Banglore, India; Model: ULK-06) of suitable pumping speed (35m^3/hr) is sufficient to acquire the base pressure (10^{-2} mbar) and working pressure (1-5 mbar) required for PN. In practice, a conductance control valve is connected between the rotary pump and the remaining system to reduce the effective pumping speed and for this system the required flow rate to sustain 5 mbar working pressure is 80 SCCM.

2.6 Summary

A DC planar magnetron set up is used to characterize the magnetron discharge plasma. The fundamental aspects for the planar magnetron chamber design; such as pumping speed for the pumps and flow rate to be kept for maintaining the operating pressure is calculated. The details of the diagnostic tools to characterize the magnetron discharge plasma are given in this chapter. The Langmuir probe I-V characteristics and optical emission spectrographs at various operating conditions for the magnetron set up is achieved to determine the values of plasma parameters. A description of plasma nitriding mechanism is discussed and the basic differences between the two surface modification techniques are mentioned. The schematic diagram of the plasma nitriding chamber is also given in this chapter.

References

[1] B. C. Chapman. *Glow Discharge Processes,* chapter 6, page 188. John Wiley and Sons, Inc., 1980.

[2] A. J. Lichtenberg, and M. A. Lieberman. *Principles of Plasma Discharges and Materials Processing*, pages 559–560. John Wiley and Sons, Inc., Hoboken, New Jersey, 2 edition, 2005.

[3] A. T. Stelbovics and P. L. Bartlett, Phys. Rev(A). **66,** 102707 (2002).

[4] N. Laegreid and G. K. Wehner, J. Appl. Phys. **32,** 365 (1961).

[5] R. V. Stuart and J. Appl. Phys. **33,** 2345 (1962).

[6] K. Koski, J. Holsa, and P. Juliet, Surf. Coat. Technol. **116,** 716 (1999).

[7] R. J. Elsey, Vacuum, **25(7),** 299 (1975).

[8] J. F. O'Hanlon. *A User's Guide to Vacuum Technology*, page 123. John Wiley and Sons, Inc., Hoboken, New Jersey, 3 edition, 2003.

[9] H. Kakati, A. R. Pal, H. Bailung, and J. Chutiya, J. Appl. Phys. **101,** 083304 (2007).

[10] F. F. Chen, Lecture notes on langmuir probe diagnostics. In IEEE-ICOPS meeting, Jeju, Korea, June 5, 2003.

[11] F. F. Chen. *Introduction to Plasma Physics and Controlled Fusion*, page 23. Plenum Press, 1984.

[12] P. Saikia, B. Kakati, and B. K. Saikia, Phys. Plasmas. **20,** 103505 (2013).

[13] P. Saikia, and B. Kakati, J. Vac. Sci. Technol. **31,** 061307 (2013), Erratum: "Effect of process parameters on properties of argon–nitrogen plasma for titanium nitride film deposition, P. Saikia, B. Kakati, and B. K. Saikia, J. Vac. Sci. Technol. **A 32,** 043401 (2014) doi: http://dx.doi.org/10.1116/1.4884595.

[14] N. Laidani, R. Bartali, P. Tossi, and M. Arderle, J. Phys. D: Appl. Phys. **37,** 2593 (2005).

[15] P. J. Kelly and R. D. Arnell, Vacuum **56,** 159 (2000).

[16] A. Y. Wong, N. D'Angelo, and R. W. Motley, Phys. Rev. Lett., **9,** 415 (1962).

[17] P. Hatta, and N. Sato, *Prof. 5th Int. Conf. on Ionization, Phen in Gases,* North Holland, Amsterdam, (1962).

[18] S. Watanbe, J. Plasma Phys. **14,** 353 (1975).

[19] E. Okutsu and Y. Nakamura, Plasma Physics **21,** 1053 (1979).

[20] L. Schott, Phys. Fluids B **3,** 236 (1991).

[21]J. L. Cooney, D. W. Aossey, J. E. William, M. T. Gavin, H. S. Kim, Y. C.Hsu, A. Scheller, and K. E. Lonngremi, Plasma Sources Sci. Technol. **2,** 73 (1993).

[22] S. K. Sharma, K. Devi, N. C. Adhikari, and H. Bailung, Phys. Plasmas. **15,** 82111 (2008).

[23] D. L. Smith, *Thin film deposition Principal and Practices*, McGraw-Hill professional, (1995).

[24] J. M. Hollas, *Modern Spectroscopy*, (4th Edition, John Wiley & Sons Ltd, England), (2004).

[25] Xi. M. Zhu and Yi. K. Pu, J. Phys. D: Appl. Phys. **43,** 403001 (2010).

[26] D,. Deepla, G. Buyle, J. Hammer, and R. De. Gryse, Surf. Coat. Technol. **200,** 4329 (2006).

[27] P. Saikia, B. K. Saikia, K. S. Goswami, and A. Phukan, J. Vac. Sci. Technol A **32,** 031303 (2014).

[28] H. Amemiya, N. Yasuda, and M. Endou, Plasma Chem. Plasma Proc. **14,** 209 (1994).

[29] N. Renevier, T. Czerwiec, P. Collignon, H. Michel, Surf. Coat. Technol. **98**, 1400, (1998).

[30] Y. K. Pu, Z. G. Guo, Aman-ur-Rehman, Z. D. Yu and J. Ma Plasma Phys.Control. Fusion **48,** 61(2006).

[31] J. B. Bofard, C. C. Lin, and C. A. DeJoseph, J. Phys. D: Appl. Phys. **37,** R143 (2004).

[32] David Pye, *Practical Nitriding and Ferritic Nitrocarburizing*, ASM International, materials Park, Ohio. 2003.

[33] S. Mukherjee, Current Science, **83,** 263 (2002).

[34] C.F.M. Borges, S. Hennecke, E. Pfender, Surf. Coat. Technol. **123**, 112 (2000).

[35] P. C. Jindal, J. Vac. Sci. Technol.,**15**, 313(1978).

[36] S. K. Sinha, Effect of process parameters on plasma nitriding, PhD Thesis, Devi Ahilya Vishwavidyalaya, Indore (2008).

[37] A. Szasz, D.J. Fabian, A. Hendry, Z. Szazne-Csih, J. Appl. Phys. **66**, 5598 (1989).

CHAPTER 3

Study on the effect of target on the plasma parameters of hydrogen added argon DC planar magnetron plasma

This chapter contains the observations on the effects of target material and hydrogen addition in the evaluation of the plasma parameters in the substrate vicinity of the magnetron discharge plasma.

3.1 Introduction

In the magnetron sputtering the target is used as the cathode and it is bombarded by ions. The secondary electrons emitted from the magnetron target due to ion bombardment plays an important role in sustaining the discharge as well as determining the plasma parameters [1-3]. Amount of secondary electrons emitted per ion is known as the ion induced secondary electron coefficient (ISEE). Phels et *al.* [4] have shown that the ISEE coefficient strongly depends on the condition of the target material and independent of the bombarding ion types for ion energy below 500 eV. Most of the works in the literature using magnetron sputtering have commonly reported the properties of deposited films [5-7]. Many experimental and theoretical works have been performed on the physical properties [8] of magnetron discharge and its dependence on the process parameters like gas pressure, substrate biasing, electrical power etc. But very few reports are available about the dependence of the plasma parameters of the magnetron discharge on the target conditions namely; the target material and degree of chemisorptions in case of reactive sputtering [9]. The target conditions mostly depend on its ISEE coefficient values. The shape of the target current voltage (V-I) characteristics of a magnetron sputtering device is also dependent on the ISEE coefficient [9] that in turn influences the plasma parameters of the magnetron

discharge. Ion flux flowing to the substrate is affected by the ISEE coefficient values significantly. Several authors have published empirical relations for the ISEE coefficient as [10-12],

$$\gamma_{ISEE} = 0.032(0.78E_i - 2\phi) \qquad (3.1)$$

$$\gamma_{ISEE} = 0.16(E_i - 2\phi) \qquad (3.2)$$

$$\gamma_{ISEE} = 0.2(0.8E_i - 2\phi)/E_F \qquad (3.3)$$

Here, E_i is the ionization energy of the ion, ϕ is the work function and E_F is the Fermi energy of the metal. Based on these empirical relations, an averaged value of 0.091 for Chromium (Cr) and 0.082 for Cupper (Cu) target materials are calculated. In this chapter, the experimental measurement of influence of the target material on the plasma parameters of the magnetron discharge is reported. Along with the target effect, the trend of modulation of the plasma parameters as a function of hydrogen addition is also studied. The addition of hydrogen is based on the fact that the use of hydrogen radicals as the reducing agents to improve the density and crystallinity of the transition metal nitrides thin films by the DC planar magnetron sputtering is getting an increased interest in the last few years [13].

Cu and Cr targets are selected because of their wide range of utility as coating materials and distinct ISEE coefficient values. Cr and Cu are sputtered deposited on Si(100) substrate in the argon-hydrogen (Ar/H_2) plasma at different discharge conditions. The working pressure and the applied input power are the two most important experimental parameters in magnetron sputtering. First, adding more hydrogen at a fixed argon partial pressure varies the working pressure. These types of experiments are interesting to understand the variation

of the plasma parameters of the discharge during sputtering. Second, at a fixed working pressure the V-I characteristics of the planar magnetron are determined by varying the input power. Finally, measured values of ion density, electron density, degree of ionization, and sputtering rate as a function of working pressure for both targets are reported here. In the section 3.2 the experimental set-up and diagnostics tools are discussed in detail. The variations of plasma parameters and other results obtained are presented in the section 3.3. In the conclusion section 3.4, the important findings of this work are summarized.

3.2 Experimental set up and diagnostic procedure

The details of the experimental set up to study the effect of target on the plasma parameters of the hydrogen added argon DC planar magnetron plasma have been described in the section 2.2 of Chapter 2. The water-cooled Cu and Cr target of diameter 70mm are used as the cathode of the planar magnetron sputtering system. The chamber is evacuated by a diffusion pump backed by a rotary pump up to base pressure of 10^{-4} Pa. During the deposition argon (Ar) and hydrogen (H_2) are fed into the deposition chamber by two digital mass flow controllers (DFC 26, AALBORG USA). Working pressure in the chamber is varied by increasing the hydrogen concentration [H_2] in the argon discharge from 0 to 18.9% at a constant argon flow rate (8.5 SCCM). The concentration of H_2 in feed gas is calculated comparing the partial pressure of both the gases. For different percentage of hydrogen flow rate, the total working pressure changes from 4×10^{-1} Pa to 10×10^{-1} Pa. Again at a constant working pressure (4×10^{-1} Pa), keeping the other conditions same, effective load power is varied from 50W to 350 W. The details of the currents and voltages at different discharge conditions for both Cr and Cu targets are given in **Tables 3.1** and **Table 3.2**. Plasma parameters of the discharge are probed by a cylindrical probe with a

length of 3.0mm and a radius of 0.1mm. To estimate the value of degree of ionization and the degree of dissociation in the hydrogen by measuring the intensity level of specific emission, a 1/2 m digikrom spectrometer (CVI Laser Corp, USA. Digikrom Model DK 480) is used.

Table 3.1: Discharge Voltage and Current at various working pressures for Chromium and Copper Target

Target	Chromium		Copper	
Working Pressure ($\times 10^{-1}$Pa)	Voltage (V)	Current(A)	Voltage (V)	Current (A)
4	587	0.52	627	0.481
6	598	0.513	635	0.472
8	605	0.507	645	0.465
10	615	0.493	668	0.451

3.3 Results and discussions

To discuss the effect of the target material and hydrogen addition in the evaluation of the plasma parameters in the substrate vicinity, knowledge of secondary electron density and the various ionic processes in the hydrogen added argon plasma is very essential. Results and discussion part of this chapter thus begins with discussing this two important aspects.

3.3.1 Variation of the secondary electron density in the ring region of the magnetron discharge

There are two categories of electrons in the DC planar magnetron discharge: fast secondary electrons (hot electrons emitted at the cathode) and bulk electrons created in the main

discharge region. Those electrons that have enough energy to ionize neutrals include mostly the fast secondary electrons. In the ring region [14] of the magnetron discharge, the hot

Table 3.2: Discharge Voltage and Current at various applied powers for Chromium and Copper Target

Target	Chromium		Copper	
Input Power (Watt)	Voltage (V)	Current(A)	Voltage (V)	Current (A)
50	452	0.11	510	0.10
100	500	0.21	550	0.19
200	562	0.36	606	0.33
300	600	0.51	650	0.47

secondary electrons are responsible for ionization of neutrals and thus eventually generating electrons in the plasma bulk and therefore determining the plasma parameters. Therefore, the determination of secondary electron density is the prime aspect for such investigation. Estimating the value of plasma density n_i within this ring region and using the data for the ionization cross-section for the secondary electrons, it is possible to determine the value of hot secondary electron density (n_s) [14]. The Bohm flux can be used to estimate n_i in the ring region of the discharge and can be given as,

$$0.61 e n_i u_B = J_i \tag{3.4}$$

where the electron temperature T_e enters only weakly. Here J_i is the ion current density and u_B is the Bohm velocity of ions. Now the ion density (n_i) can be related to fast secondary electron density (n_s) within this region as,

$$n_i = n_a n_s \sigma_i v \quad (3.5)$$

where v is the drift velocity of the electrons, n_a is the neutral density and σ_i is the ionization cross section for secondary electrons (~ 5×10^{-17} cm^2). Using the above-mentioned equation, the value of fast secondary electron density within the ring region is evaluated. It is observed that with increasing working pressure the secondary electron density decreases from $7.8 \times 10^{10}/m^3$ to $2.67 \times 10^{10}/m^3$ for Cr target and $6.67 \times 10^{10}/m^3$ to $2.26 \times 10^{10}/m^3$ for Cu target. While an opposite trend of rising secondary electron density from $3.34 \times 10^{10}/m^3$ to $7.5 \times 10^{10}/m^3$ for Cr target and $2.56 \times 10^{10}/m^3$ to $6.67 \times 10^{10}/m^3$ for Cu target as a function of increasing applied power (50 Watt to 350 Watt) is also found. As expected the value of ion density (of the order of $10^{17}/ m^3$) is found to be much higher than hot secondary electron density (of the order of $10^{10}/m^3$) in this region of the discharge. Also, it is interesting to mention that the density of hot secondary electron decreases when hydrogen is added to the pure argon discharge. Using Langmuir probes diagnostics the densities of bulk electrons are measured in the substrate vicinity and results will be presented in the subsequent sections.

3.3.2 Description of ionic processes in H_2 containing argon plasma

Study of basic gas phases is essential to understand the effect of H_2 addition to pure argon plasma. When H_2 is added to argon, besides Ar atoms (in ground state and excited to meta-stable states (Ar_m^*) at energy 11.2 ev), Ar^+ ions, several hydrogen species including H^+, H_2^+, H_3^+ ions; ArH^+ ions, the ground state H atom, ground state H_2 molecule and various electronically excited states of H_2 molecules are also possible [15]. All those species in plasma undergo different chemical reactions with different rate constants and relative cross-

sections. The reactions that are essential for the domain of this work are mentioned in **Table 3.3**. With increasing hydrogen addition a drop in electron and Ar^+ ion densities are experimentally observed in literature [16-19]. On the other hand, the densities of hydrogen related ions, i.e., H^+, H_2^+, H_3^+ and ArH^+ are expected to increase with H_2 addition for obvious reasons. The effect is most pronounced for H^+, H_2^+, H_3^+ and is slightly less significant for ArH^+ ions.

Addition of Hydrogen in the argon plasma causes Ar^+ ion loss predominantly through the charge transfer (Reaction 1 in **Table 3.3**) or H atom transfer (Reaction 2 and Reaction 3 in **Table 3.3**) forming different hydrogen species (ArH^+, H, H_2^+) [15].

$$Ar^+ + H_2 \rightarrow Ar(fast) + H_2^+ \quad (3.6)$$

$$Ar^+ + H_2 \rightarrow ArH^+ + H \quad (3.7)$$

$$Ar + H_2^+ \rightarrow ArH^+ + H \quad (3.8)$$

The major loss mechanism for electrons in such plasma is the electron recombination with ArH^+ (Reaction 4 in **Table 3.3**), H_2^+ (Reaction 5 in **Table 3.3**) and H_3^+ (Reaction 6 in **Table 3.3**).

$$e^- + ArH^+ \rightarrow Ar + H \quad (3.9)$$

$$e^- + H_2^+ \rightarrow H + H \quad (3.10)$$

$$e^- + H_3^+ \rightarrow H + H + H \quad (3.11)$$

Reaction 2 and Reaction 3 are responsible for the formation of ArH^+ ions. In such plasma, the densities of H_3^+ ions are reported to be several orders of magnitude higher [20-21] than H_2^+ and H^+ densities in literature. H_3^+ ions are mostly formed through proton transfer (Reaction 7 and Reaction 8 in **Table 3.3**).

$$ArH^{+} + H_2 \rightarrow Ar(fast) + H_3^{+} \quad (3.12)$$

$$H_2^{+} + H_2 \rightarrow H + H_3^{+} \quad (3.13)$$

The Ar meta-stable atoms are mainly created by electron impact excitation (Reaction 9), followed by fast Ar^0 impact excitation and fast Ar^+ impact excitation and relative importance of these processes are more or less same. On the other hand, quenching upon collision with H_2(Reaction 10) is the main loss mechanisms [15] for Ar_m^* atoms.

$$Ar + e^{-} \rightarrow Ar_m^{*} + e^{-} \quad (3.14)$$

$$Ar_m^{*} + H_2 \rightarrow Ar + H + H \quad (3.15)$$

3.3.3 Plasma parameters as a function of working pressure

3.3.3 (a) Langmuir probe measurement

The probe measurement is carried out in the downstream region at a distance of 80mm from the cathode, i.e., 10mm above the substrate keeping in mind about the fact that the ions present in this region most significantly affect the growth of thin film on the substrate. Plasma parameters such as the electron temperature (T_e), electron density (n_e), and ion density (n_i) are measured with the probe in practically magnetic field free region. The radius of the probe (0.1mm) was chosen such that it is greater than the calculated deBye length. A Teflon holder is used to cover the probe tip in order to avoid it being coated by sputtered target. Only during the duration of the Langmuir probe scan the probe tip is exposed to the magnetron discharge. Thus, the charge collection area of the Langmuir probe does not vary significantly during the deposition and the values of the plasma parameters is authentic.

Table 3.3: Ar^+ , ArH^+, Ar_m^* and Hydrogen like ion production and loss processes

No.	Reaction	Rate Constant (K)	Name
1.	$Ar^+ + H_2 \rightarrow Ar(fast) + H_2^+$	8.0×10^{-11} cm^3s^{-1}	Charge transfer [22]
2.	$Ar^+ + H_2 \rightarrow ArH^+ + H$	6.0×10^{-10} cm^3s^{-1}	H atom transfer [22]
3.	$Ar + H_2^+ \rightarrow ArH^+ + H$	1.7×10^{-9} cm^3s^{-1}	Proton Transfer [22]
4.	$e^- + ArH^+ \rightarrow Ar + H$	1.7×10^{-7} cm^3s^{-1}	Recombination[22]
5.	$e^- + H_2^+ \rightarrow H + H$	1.0×10^{-7} cm^3s^{-1}	Recombination [22]
6.	$e^- + H_3^+ \rightarrow H + H + H$	1.0×10^{-7} cm^3s^{-1}	Recombination [15]
7.	$ArH^+ + H_2 \rightarrow Ar(fast) + H_3^+$	1.5×10^{-9} cm^3s^{-1}	Proton Transfer [22]
8.	$H_2^+ + H_2 \rightarrow H + H_3^+$	$2.2\times 10^{-10} cm^3s^{-1}$	Charge Transfer [22]
9.	$Ar + e^- \rightarrow Ar_{m*} + e^-$	$1.0\times 0^{-11} cm^3s^{-1}$	Ionization [15]
10.	$Ar_m^* + H_2 \rightarrow Ar + H + H$	$7\times 10^{-11} cm^3s^{-1}$	Quenching dissociation [15]
11.	$ArH^+ + Ar \rightarrow Ar(fast) + H^+ + Ar$	1.5×10^{-9} cm^3s^{-1}	Induced Ionization [15]
12.	$H^+ + Ar \rightarrow H(fast) + Ar^+$	$2.2\times 10^{-10} cm^3s^{-1}$	Charge Transfer [15]
13.	$H_2 + H^+ \rightarrow H(fast) + H_2^+$	2×10^{-9} cm^3s^{-1}	Charge Transfer [15]

The typical Langmuir probe I-V plots for Ti, Cr and Cu target are shown **Fig. 3.1**.The electron (n_e) and ion density (n_i) are obtained from the electron and ion saturation current collected by the probe using the following equation,

$$n_{e,i} = \frac{I_{ie,is}}{A_p}\sqrt{\frac{2\pi m_{i,e}}{e^2 k_B T_e}} \tag{3.16}$$

with A_p stands for the probe area, $m_{i,e}$ is either the electron (*e*) or ion (*i*) mass, $k_B T_e$ is the electron temperature (in electron volts) and *e* the electronic charge. $k_B T_e$ is calculated from

retardation region of the I-V characteristic as the inverse slope of the logarithmic electron probe current with respect to the probe voltage. In order to explain the modulation of the plasma parameters as a function of working pressure (i.e., addition of hydrogen keeping argon partial pressure constant), it is necessary to compare the results

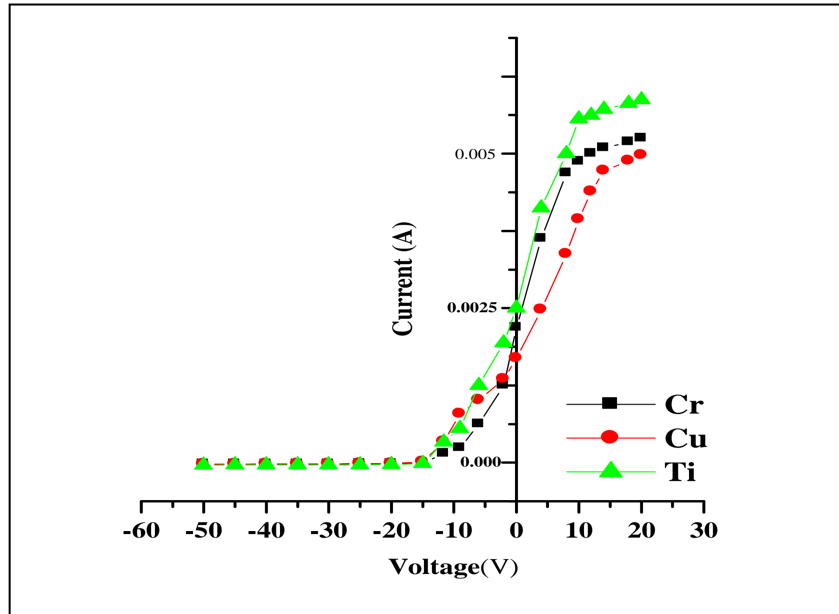

Figure 3.1 Typical Langmuir probe I-V characteristics traced at working pressure 4×10^{-1} Pa for hydrogen added argon plasma for titanium, chromium and copper magnetron target. Input power (P) = 300W for each target.

with the pristine argon plasma. Evolution of electron density (n_e) and the ion saturation current density ($I_{is}(V)$) with working pressure for pristine and hydrogen added argon plasma are shown in the **Fig. 3.2**. It can be seen that there is a gradual increase of electron density for both the targets in the pristine argon plasma. But the hydrogen addition reduces n_e from 1.4×10^{15} m^{-3} to 6.46×10^{14} m^{-3} for Cr and 9.5×10^{14} m^{-3} to 5.8×10^{14} m^{-3} for Cu target, respectively. As the electron density decreases as a function of working pressure the

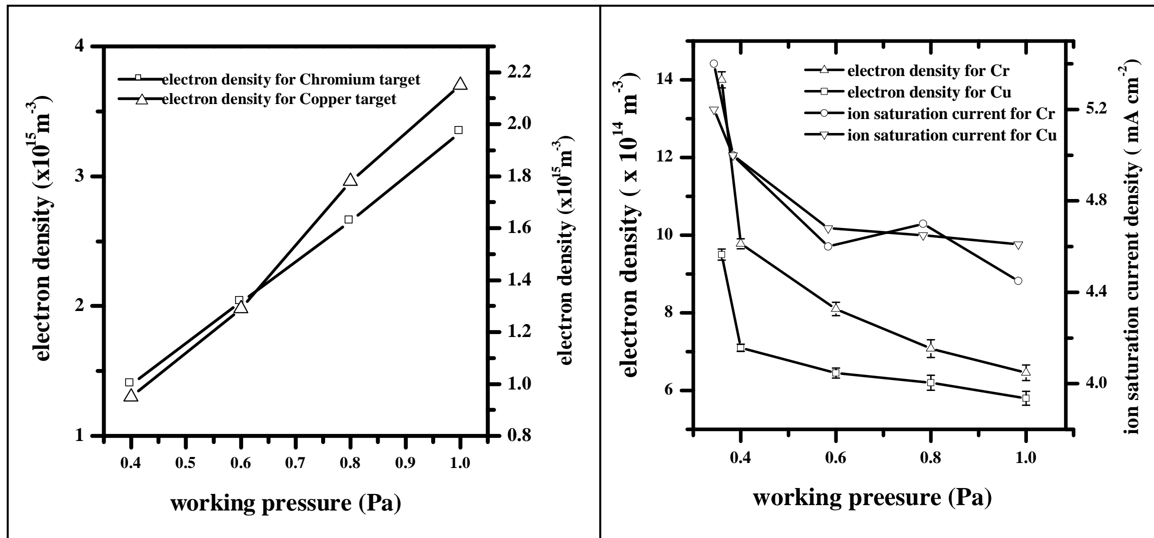

Figure 3.2(a) Variation of electron density (n_e) as a function of working pressure for Cr and Cu target for pristine argon plasma.(b) Variation of electron density (n_e) and ion saturation current density as a function of working pressure for Cr and Cu target for hydrogen added argon plasma.

ion density should follow the similar behavior if one refers to the quasi neutrality property of plasma. With this consideration, it is found that the ion saturation current ($I_{is}(V)$) declines with hydrogen enrichment in argon plasma. The decreasing value of electron density reflects major electron loss rate when H_2 is added to Argon plasma. In Ar-H_2 plasma the dissociative recombination reactions between electrons and molecular ions (H^+, H_2^+ and H_3^+) formed in the plasma tend to more pronounce than am-bipolar diffusion and Ar^+-electron recombination [18,23]. Due to presence of these additional loss processes with hydrogen introduction in such plasma, the electron consumption rate becomes more significant than the various electron production processes. As a result n_e drops as a function of working pressure and this fact can be represented mathematically by the following equation:

$$\frac{d(n_e)}{dt} = k_{ion} n_e n_{Ar} - \sum_i k_{recom} n_e n_{Hions} < 0 \tag{3.17}$$

Here, n_{Ar} is the density of neutral argon atoms, k_{recom} is the rate constant of electron recombination with the hydrogen-like ions [Eq. (3.9) to Eq.(3.11)], n_{Hions} is the density of hydrogen-like ions and k_{ion} is the rate constant for the ionization of argon atom by electrons. For such plasma, a prominent change in electron temperature is also observed. With increasing working pressure, the value of electron temperature increases significantly from 3.3 eV to 6.60 eV for Cr and from 5.20 eV to 7.8 eV for Cu. Since in the ohmic heating regime there is an inverse relation between n_e and T_e, the observed gradual increase of T_e upon hydrogen addition can be easily understood [**Fig. 3.3**].

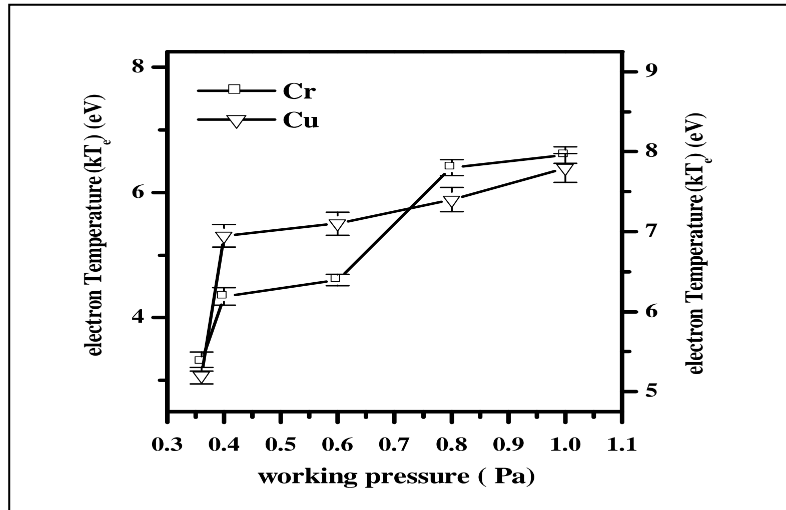

Figure 3.3 Influence of working pressure on the variation of electron temperature ($k_B T_e$ in eV) for Cr and Cu target.

The higher value of the bulk electron density in the magnetron discharge with Cr target than Cu target is due to its high ISEE coefficient value (0.091) compared to Cu (0.082). By particle simulation Kondo et *al.* [9] have shown that the plasma density in the bulk region

of the plasma is larger for higher value of ISEE. As the electron density value is higher for Cr compared to Cu one could expect lower value of electron temperature. As Ar/H_2 plasma contains various ion species (Ar^+, ArH^+, H^+, H_2^+, H_3^+ etc.), it is not possible to determine the density of each ion individually using the Langmuir probe. Also, due to the presence of these ionic species the use of argon ion mass in the calculation for ion density is not valid. As such, we have divided the ions present in such discharge into two groups based on their masses. A heavy group of mass 40 a.m.u (Ar-like ions) consisting of Ar^+ and ArH^+ ions and a light group of mass 2 a.m.u (Hydrogen-like ions) consisting of H^+, H_2^+, H_3^+. Rather than calculating the density of each ion, the density of each group is calculated following the mean ion mass procedure as developed by Laidani et *al* [24]. As explained in Chapter 2, using the ion saturation current ($I_i(V)$), electron temperature ($k_B T_e$) and ion density (n_i) values, the mean ion mass is calculated [24] and the trend of its variation as a function of working pressure is found to be similar for both types of targets [**Fig. 3.4 (a)**].

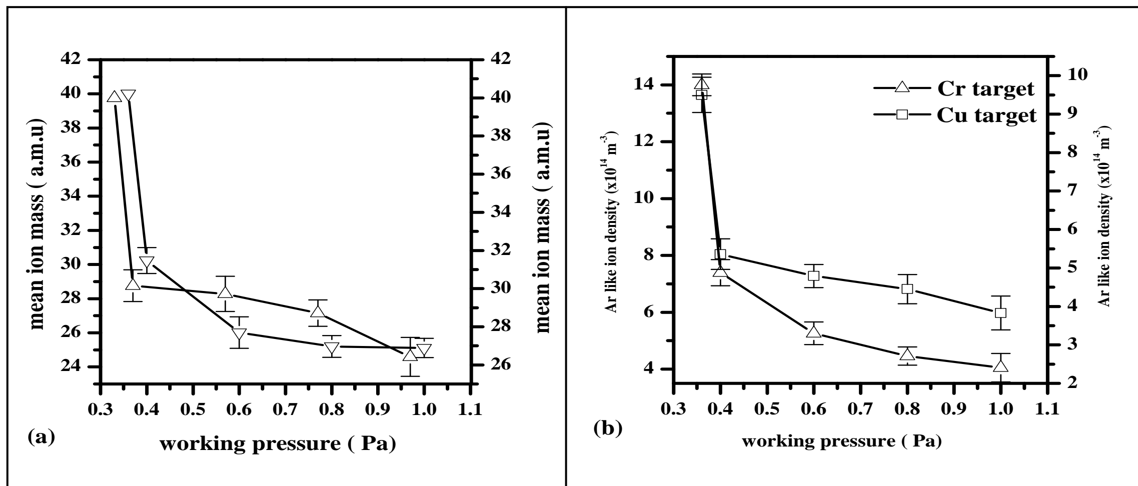

Figure 3.4 Variation of (a) mean ion mass and (b) Ar like ion density as a function of working pressure for Cr and Cu target.

It is clear from the figure that presence of hydrogen-like ion decreases the mean ion mass from 40 a.m.u to 25.11 a.m.u. for Cr target and 40 a.m.u to 26.42 a.m.u for Cu target, respectively. From the above data and using the fact that total ion density (n_i) is the sum of Ar-like (Ar^+, ArH^+) and hydrogen-like ions (H^+, H_2^+, H_3^+), Ar like ion density is calculated and given in the **Fig. 3.4 (b)**. Ar like ion density decreases linearly with the hydrogen percentage enrichment in the discharge. Addition of hydrogen in the argon plasma reduces Ar^+ ion predominantly through charge transfer between Ar^+ and H_2 (Reaction 1 in **Table 3.3**) or H atom transfer between the between the same (Reaction 2 in **Table 3.3**). This trend is found to be similar for both types of targets. The observed enhanced value of Ar like ion density for Cr target than Cu target in the discharge is due to higher ISEE coefficient of Cr than Cu.

3.3.3 (b) Optical emission spectroscopy study

The Langmuir probe scan of the plasma at the mentioned discharge condition reveals a decrease of Ar-like ion density in the discharge. As the argon partial is kept constant, it is reasonable to expect a decrease of degree of ionization of argon in such discharge. This fact is qualitatively examined by the optical emission spectroscopy study. In the low pressure plasma discharge, the intensity of spectral emission line is closely related to the density of the species and hence is often used to deduce the evaluation of density [25]. Thus, the line intensity ratio between two suitable spectral lines can be used to estimate the value for degree of ionization of Ar and degree of dissociation H_2. The experimental arrangement for collection of emission intensity from the magnetron discharge was shown in the **Fig. 2.11** of the Chapter 2. The emissions are collected by a light collecting system (LCS)

through an optical fiber (F). The variations in the intensity of different species with hydrogen composition are observed with the LCSF placed at a vertical distance of 8 cm below the cathode surface. **Fig. 3.5** shows the comparison between argon and argon added hydrogen spectra. In the argon-hydrogen magnetron discharge the most prominent excited species are: Ar I lines corresponds to atomic argon emission(696.45 nm, 738.39 nm,751.46 nm,763.51 nm,772.37 nm,794.81 nm,801.47 nm,811.53 nm,826.45 nm,840.42 nm, and 852.14 nm), Ar II lines correspond to Ar^+ ionic emission (434.80 nm, 454.15 nm, 472.68 nm, 476.48 nm, 480.60 nm) H_α line (656.28 nm) and H_β line (487.54 nm). Here, the intensity ratio of argon spectral line at 476.4 nm (Ar II) to at 751.46 (Ar I) (δ) is used to estimate the value of degree of ionization. These two lines are selected as the excitation thresholds are very close and the transition probabilities (6.4×10^7 s^{-1} at 476.48 nm and

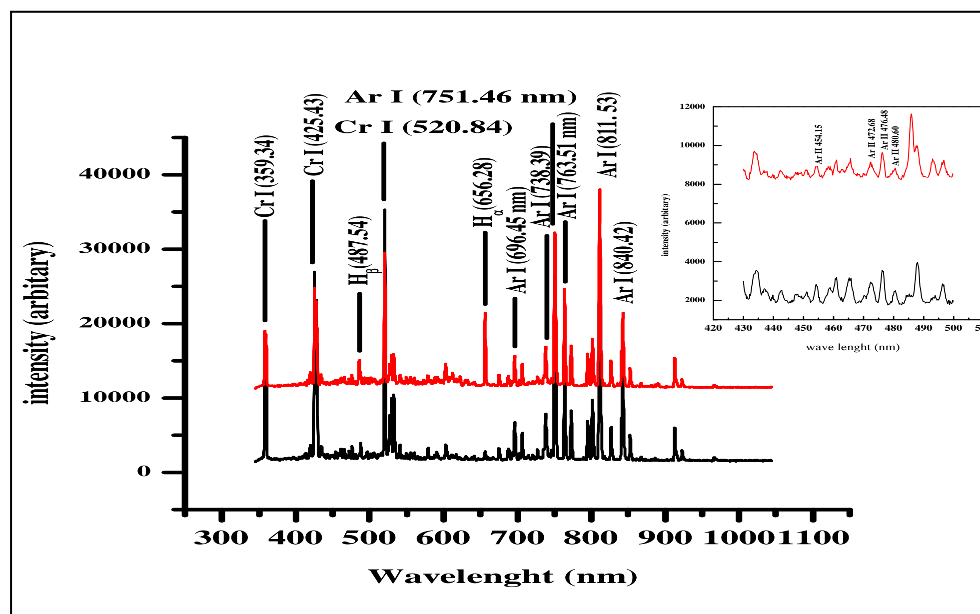

Figure 3.5 The emission lines of the spectra collected for the pristine (black line) and hydrogen added argon plasma (red line) at the working pressure of (4.0×10^{-1}Pa).The emitting species were identified by comparing with NIST database.

4.0×10^{7} s^{-1} at 751.46 nm) are almost similar [26, 27]. Also, the intensity ratio of H_α line (656.28 nm) to Ar(I) line (811.53 nm) can be used to determine the value for degree of dissociation (f_D) of H_2. **Fig. 3.6** shows the variation of Ar I line (751.46 nm), Ar II line (476.48 nm), H_α line (656.28 nm), Ar(I) line (811.53 nm) intensity as a function of working pressure for the Cr and Cu target respectively. It is clear from the **Fig. 3.6** that the intensity of Ar I and Ar II lines decreases with hydrogen addition. The intensity of H_α line increases rapidly in comparison to the intensity of H_β line. The energy required for direct excitation by electron from ground state to H_α is 12.1 eV, where as for H_β excitation is 12.7 eV [30]. This explains the faster increase in intensity of H_α line than the intensity of H_β line.

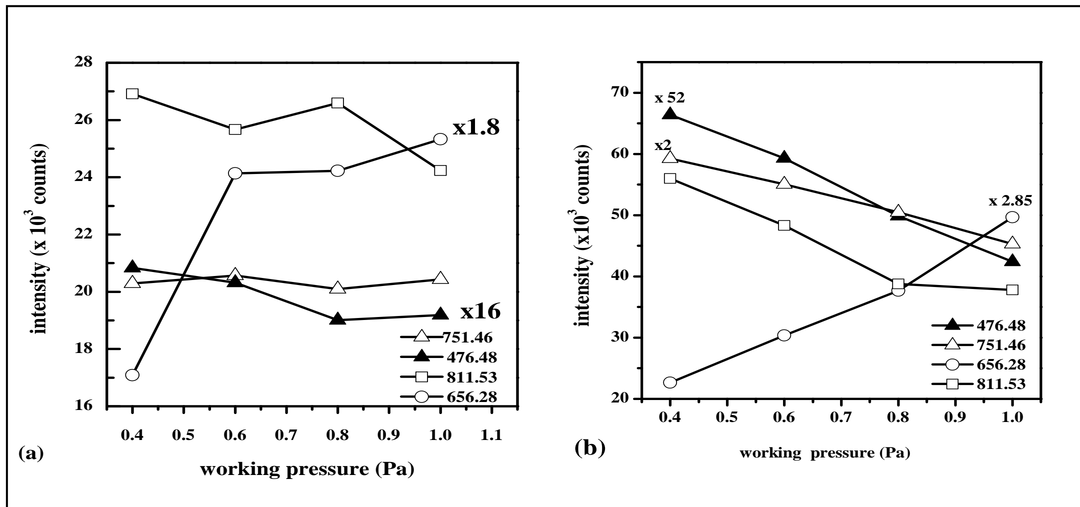

Figure 3.6 Observed Intensity (I) of atomic argon line at 476.48nm (Ar II), 751.46nm (Ar I), 811.53nm (Ar I) and H_α line (656.28 nm) as a function of working pressure (a) Cr target (b) Cu target.

Fig. 3.7 shows that with increase of working pressure, δ decreases from 7.1×10^{-2} to 5.8×10^{-2} for Cr and 4.3×10^{-2} to 3.6×10^{-2} for Cu target. The decline of the value of δ as a function of working pressure indeed justifies the trend of Ar-like ion density variation in such plasma. It is reasonable to find higher value of δ for Cr to Cu irrespective of discharge

condition. As electron impact ionization of Ar atom is major production mechanism for Ar^+ ions, higher electron density for Cr will naturally lead to enhanced value for δ compared to Cu.

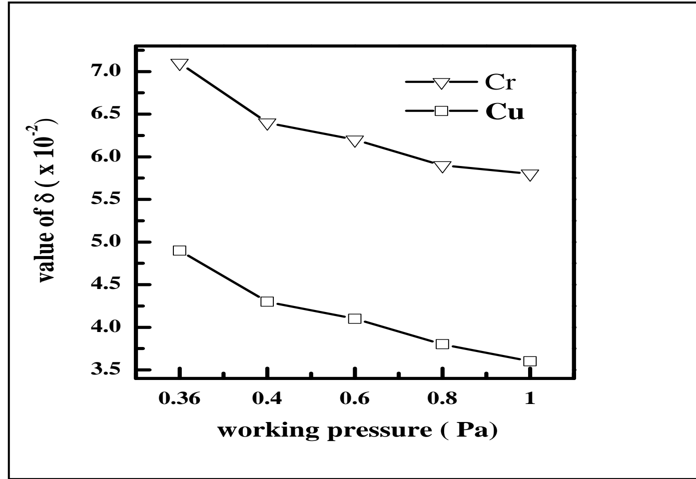

Figure 3.7 Variation of the intensity ratio (δ) as a function of working pressure.

The variation of f_D as a function of working pressure is given in **Fig. 3.8**. It can be seen that f_D decreases from 7.2% to 2.94% for Cr and 2.8% to 2.35% for Cu target with hydrogen enrichment in the discharge. In Ar/H_2 plasma, the dominant production of H atoms is due to the dissociative excitation of H_2 molecules by Ar_m* atoms [15]. With the addition of H_2, the density of Ar_m* atoms decrease continuously. As the quenching dissociation (due to Reaction 10 in **Table 3.3**) is the most important mechanism for formation of H atoms, it indeed explains the gradual drop in f_D. Here also, we have observed a relatively higher value of f_D for Cr target compared to Cu.

3.4 Influence of target material on V-I characteristics of magnetron discharge

The Langmuir probe study reveals the higher electron and ion density in the lower working pressure condition. Keeping this fact into account, the variation of input power was done at a fixed working pressure of 4×10^{-1}Pa. These types of experiments are interesting to under-

stand the dependence of steepness of the V-I characteristics on the magnetron target during

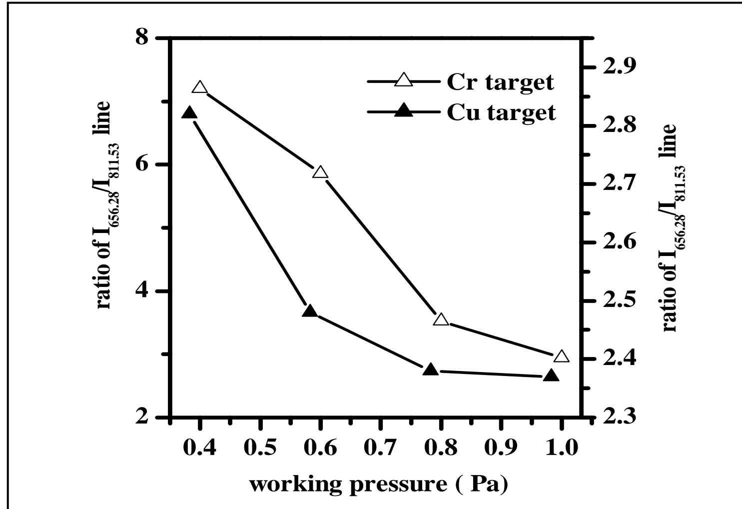

Figure 3.8 Variation of intensity (I) ratio of H_α line (656.28 nm) to Ar(I) line (811.53 nm) as a function of working pressure.

sputtering. The V-I characteristics of magnetron discharge have been proposed by Westwood et *al.* [31] as,

$$I = \beta(V - V_0)^2 \tag{3.18}$$

with V_0 is minimum voltage required to maintain the discharge, β is a constant which is a measure of the steepness of V-I characteristics and I is the discharge current that comprises mainly of ion current. Value of β can be determined by a linear fit to the square root of current (I) as a function of the discharge voltage. Based on a PIC/ MC simulation, Kondo et *al.* [32] concluded that the effect of the ISEE coefficient on the magnetron discharge is qualitatively analogous to the DC glow discharge. Their simulations show that at constant discharge voltage, a higher ISEE coefficient results in a higher plasma density. A higher plasma density results in lower plasma impedance [9], and therefore, a higher

value of β is expected in this case. Now, at fixed working pressure of 4×10^{-1} Pa, the V-I characteristics of both the targets are plotted in the **Fig. 3.9** and β ($\times10^{5}$ V/A^{2}) values are found to be 34.1 for Cr and 21.9 for Cu. Higher value of β for the Cr target justifies its superior electron and ion density in the magnetron discharge compared to the Cu target.

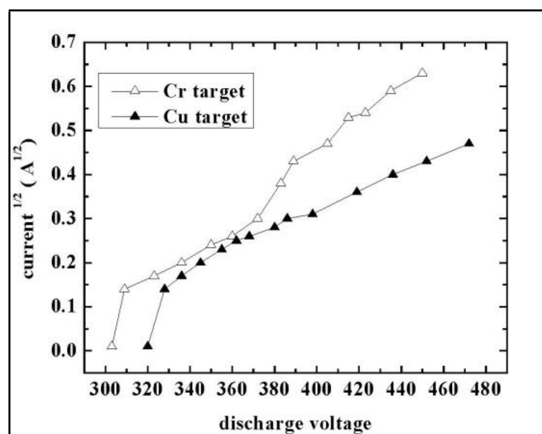

Figure 3.9 $\sqrt{I}-V$ **characteristics at working pressure of** 4×10^{-1} **Pa.**

3.5 Hydrogen effect on the film deposition rate

In order to correlate the observed trend of plasma parameters with physical nature of sputtering process, we have measured the deposition rate for various discharge conditions. The result is given in the **Fig. 3.10**. It is seen that the sputtering rate is maximum with pure argon plasma compared to hydrogen additive Ar plasma. Addition of hydrogen gradually decreases the sputtering rate from 2.6 A^0 s^{-1} to 2.1 A^0 s^{-1} for Cr and 5.6 A^0 s^{-1} to 4.3 A^0 s^{-1} for Cu target, respectively. The sputtering yield of Cr/Cu target to Ar^+ and Ar (fast) atoms is greater than to hydrogen-like ions. From the OES and Langmuir probe study, it is clear that the addition of hydrogen in pure argon plasma leads to decrease of degree of ionization of Ar and corresponding density of the Ar like ions. Due to this fact, the drop of sputtering rate as a function of the working pressure is seen. It is interesting to find higher deposition

rate for the Cu target compared to the Cr target at particular deposition condition as sputtering yield of Cu to Ar (S = 2.3) is higher than Cr(S = 1.3) to Ar.

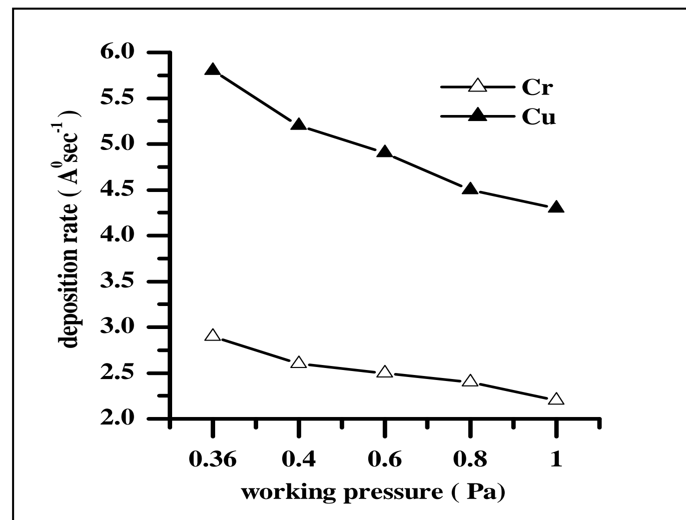

Figure 3.10 Influence of working pressure on deposition rate for Cr and Cu target.

3.6 Conclusion

The effect of target on the plasma parameters of the magnetron discharge as a function of working pressure is described in this chapter. For better film deposition the plasma parameters like electron temperature, electron density, degree of dissociation and ionization are key factors. From the Langmuir probe study, it is found that with addition of hydrogen in pure argon plasma, the densities of electrons and Ar like ions drop gradually. On the other hand, a corresponding increase in T_e is observed. To cross check the results we have also performed the OES study which also reveals a gradual decline of the degree of ionization of Ar as well as the degree of dissociation of H_2 as a function of working pressure. From the present study, it is clear that the addition of H_2 in the pure argon plasma reduces the sputtering rate. Also it is seen that the ISEE coefficient plays a crucial role in

determining plasma parameters while its effect on the sputtering rate of the target material is not observed. The increased value of electron density (n_e), ion density (n_i), degree of ionization of Ar and degree of dissociation of H_2 for Cr compared to the Cu target is explained on the basis of its higher ISEE coefficient value.

References

[1] I. Safi, Surf. Coat. Technol. **127,** 203 (2000).

[2] P. J. Kelly and R. D. Arnell, Vacuum **56,** 159 (2000).

[3] A. R. Nyaiesh, Thin Solid Films **86,** 267 (1981).

[4] A. V. Phelps and Z. L. Petrovic, Plasma Sources Sci. Technol. **8,** R21 (1999).

[5] J. Musil, L. Bardos, A. Rajsky, J. Vyskocil, B. Dolezal, G. Loncar, K. Dadourek, and V. Kubicek, Thin Solid Films **136,** 229 (1986).

[6] J. H. Huang, F. Y. Ouyang, and Ge. P. Yu, Surf. Coat. Technol. **201,** 7043 (2007).

[7] B. Subramanian and A. K. Jayachandran, Appl. Surf. Sci. **255,** 2133 (2008).

[8] S. Kondo and K. Nambu, J. Phys. D: Appl. Phys. **32,** 1142 (1999).

[9] D. Depla, G. Buyle, J. Haemers, and R. D. Gryse, Surf. Coat. Technol. **200,** 4329 (2006).

[10] R. A. Baragiola, E. V. Alonso, J. Ferron, and A. O. Florio, Surf. Sci. **90**, 240 (1979).

[11] Y. P. Raizer, Gas Discharge Physics (Springer, New York, 1991).

[12] L. M. Kishinevsky, Radiat. Eff. **19,** 23 (1973).

[13] J-S. Park, M-J. Lee, C-S. Lee and S-W. Kang, El. Solid St. **4,** C17 (2001).

[14] G. Buyle, W. D. Bosscher, D. Depla, K. Eufinger, J. Haemers, and R. D. Gryse, Vacuum **70,** 29 (2003).

[15] A. Bogaerts and R. Gijbels, Spectrochim. Acta, Part B **57,** 1071 (2002).

[16] P. F. Knewstubb and A. W. Tickner, J. Chem. Phys. **36,** 674 (1962).

[17] M. H. Gordon and C. H. Kruger, Phys. Fluids B **5,** 1014 (1993).

[18] R. F. G. Meulenbroeks, A. J. van Beek, A. J. G. van Helvoort, M. C. M. van de Sanden, and D. C. Schram, Phys. Rev. E **49,** 4397 (1994).

[19] R. S. Mason, P. D. Miller, and I. P. Mortimer, Phys. Rev. E **55,** 7462 (1997).

[20] J. T. Gudmundsson, Plasma Sources Sci. Technol. **8,** 58 (1999).

[21] A. C. Dexter, T. Farrell, and M. I. Lees, J. Phys. D **22,** 413 (1989).

[22] M. A. Liberman and A. J. Lichtenberg in Principles of Plasma Discharges and Materials Processings, edited by M. A. Liberman and A. J. Lichtenberg (JohnWiley & Sons, Inc., Hoboken, New Jersy, 2005), p. 569.

[23] M. J. de Graph, R. Servens, R. P. Dahya, M. C. M. van de Sanden, and D. C. Schram, Phys. Rev. E **48,** 2098 (1993).

[24] N. Laidani, R. Bartali, P. Tosi and M. Anderle, J. Phys. D: Appl. Phys. **37, 2593** (2004).

[25] S. Yugeswaran, K. Suresh, and V. Selvarajan, Plasma Sci. Technol. **12,** 35 (2010).

[26] J. B. Shumaker and C. H. Ponenoe, J. Opt. Soc. Am. **57,** 8 (1967).

[27] W. R. Bennett, Jr., P. J. Kindlmann, and G. N. Mercer, Appl. Opt. Suppl. **2,** 34 (1965).

[28] B. P. Lavrov, A. V. Pipa, and J. R. Opcke, Plasma Sources Sci. Technol. **15,** 135 (2006).

[29] M. Capitelli and M. Dilonardo, Chem. Phys. **24,** 417 (1977).

[30] N. Renevier, T. Czerwiec, P. Collignon, H. Michel, Surf. Coat. Technol. **98**, 1400, (1998).

[31] W. D. Westwood, S. Maniv, and P. J. Scanlon, J. Appl. Phys. **54,** 6841 (1983).

[32] S. Kondo, K. Nanbu, J. Phys. D: Appl. Phys. **32,** 1142 (1999).

CHAPTER 4

Probing magnetron discharge plasma with ion acoustic wave

This chapter contains the results of an experimental observation of ion acoustic wave propagation in the bulk region of oxygen added argon magnetron discharge plasma. The variation of the relative negative ion density as a function of reactive gas addition is studied using the ion acoustic wave diagnostics.

4.1 Introduction

As already mentioned in the introduction of this thesis, the conventional plasma diagnostics like the Langmuir probe, the optical emission spectroscopy have their limitations while using in DC planar magnetron discharge. The probe tip of the Langmuir probe is used to get coated by the material sputtered from the magnetron target during prolonged deposition. It will increase the charge collection area of the Langmuir probe and it may lead to erroneous results. Thus while using the Langmuir probe; precautions must be taken in order not to coat the tip during data acquisition. In order to overcome such limitation, the ion acoustic wave can be used as a suitable alternative diagnostic tool. Ion acoustic waves have been used as a diagnostic tool for determination of electron temperature and electron density for long. For the relative measurement of ion density, ion acoustic wave is certainly a more precise diagnostic tool than that of the Langmuir probe [1]. In this chapter, a detail study of probing the magnetron discharge plasma in the presence of negative ions is reported. Presence of negative ions is very advantageous for measurement of the relative ion density as it significantly affects the propagation of the ion acoustic wave [2]. Negative ion containing argon magnetron discharge is obtained by adding little amount of oxygen (O_2) in the argon (Ar) magnetron discharge. As oxygen is electronegative gas, it can create

volume produced negative oxygen ions by dissociative attachments with low temperature electron [3].

Multi-component oxygen additive argon plasma finds wide applications in the magnetron discharge plasma for various industrial processes. This reactive sputtering technique is widely used for the deposition of thin films of metal oxides such as SiO_2, TiO_2, Al_2O_3 etc [4-6]. The negative ions coming from the driven phase of the discharge transfer energy flux to the substrate which can be more significant than from the positive ions [7]. Also, the negative ions created in the bulk region of the discharge can alter the properties of entire discharge affecting the process and deposition characteristics. Thus, for the optimization of sputtering process a precise determination of the relative negative ion density is very essential.

In this chapter, we present an experimental study of the effect of oxygen addition on the relative negative oxygen ion concentration using ion acoustic wave diagnostics in the magnetron discharge plasma. The experiments in this study are performed in a magnetron discharge by adding oxygen gas gradually in argon plasma at an argon partial pressure of 8×10^{-4} mbar. The phase velocity of the ion acoustic waves in the discharge is measured, leading to a determination of the value of the relative negative ion concentration. The measured values of relative ion density at each discharge condition using ion acoustic wave diagnostic is benchmarked with that of a Langmuir probe measurements.

The chapter is organized in following sections. In next section (4.2) the details of the experimental arrangements for the ion acoustic wave measurement are given. The theoretical model for propagation of ion acoustic wave is presented in the section 4.3.

Detail discussion of ionic processes in oxygen containing argon plasma surface has been discussed in the section 4.4. In the following section (4.5) the estimation of the relative concentration using ion acoustic wave and benchmarking the obtained value with the Langmuir probe diagnostic is achieved. The findings of the chapter are summarized in the section 4.6.

4.2 Experimental set up and diagnostic procedure

The experiment is carried out in a DC planar magnetron system and its schematic diagram is given in the **Fig. 2.10** of Chapter 2. The method of ion acoustic wave excitation technique with the block diagram of the wave launcher is explained in the section 2.3.2 of Chapter 2. The water-cooled Titanium target of diameter 70mm is used as the cathode of the magnetron sputtering system. The chamber is evacuated by a diffusion pump backed by a rotary pump up to a base pressure of 10^{-4} Pa. Initially; argon plasma is produced at a working pressure of 8×10^{-2} Pa with applied power of 100W DC. Multi component plasma with negative oxygen ions is then formed by gradually adding oxygen in the argon plasma keeping the applied power constant. The partial pressure of oxygen is varied from 4×10^{-3} Pa to 8×10^{-3} Pa keeping the argon partial pressure constant at 8×10^{-2} Pa. Ar and O_2 are fed into the deposition chamber by digital mass flow controllers (Aalborg Make). For processes operated at a constant power, the observation of a decrease in the target voltage must be accompanied by a corresponding increase in the ion current and in the secondary electron coefficient (γ_{se}). Similarly, the observation of an increase in target voltage must be accompanied by a corresponding decrease in the ion current and in the secondary electron coefficient (γ_{se}). Because the change in the secondary electron coefficient (γ_{se}) is not

significant as a function of working pressure [8], the change in voltage is compensated by a corresponding change in the ion current, which is related to the discharge current by [9]

$$I_d = (1 + \gamma_{se})I_i \qquad (4.1)$$

For most metals γ_{se} ~ 0.05 − 0.2, so the dominating fraction of the discharge current at the target is the ion current [8]. The observed values of the discharge current and the target voltage at a constant power of 100 W are given in **Table 4.1**. It is clear that with an increasing partial pressure of oxygen there is a gradual decrease of ion current and a corresponding increase in discharge voltage.

Table 4.1: Current and voltage values in the discharge at various discharge conditions

Oxygen partial pressure (Pa)	Voltage (V)	Current (mA)
0	550	183.63
4×10^{-3}	587	170.15
6×10^{-3}	598	167.20
8×10^{-3}	605	165.28

The plasma parameters of electron temperature (T_e), electron density (n_e) and ion density (n_i) are measured with the Langmuir probe in a region that is practically free of any magnetic field ($|B| \cong 0$) [10]. Ion-acoustic perturbations are excited by using an arbitrary function generator to apply a positive sinusoidal voltage pulse of suitable amplitude (3.0 − 6.5 V) and a frequency of 50-100 kHz [11-12] to a circular fine mesh stainless steel

grid (8 cm diameter) inserted in the downstream region of the discharge. The position of the excitation grid is 10 mm above the substrate. The stainless steel grid has 20 meshes per centimeter and has a transparency of 70%. The detail procedure of excitation and detection of the ion acoustic wave is given in the Chapter 2 (Section 2.3.2). The density perturbations ($\partial n_e/n_e$) are detected using an axially adjustable planar Langmuir probe (of 6 mm diameter) biased positively with respect to the plasma potential and placed in front of the center of the mesh. The distance of the planar probe from the center of the excitation grid is varied along the axial line for the time-of-flight measurement. In this study, the phase velocity is measured from the temporal evaluation of the observed wave pattern. The range of exciting voltage is chosen such that $\partial n_e/n_e << 1$ and the signals are recorded in a digital storage oscilloscope. The position of the probe used to detect the density perturbation is kept the same as that of the cylindrical Langmuir probe.

The Optical emission spectroscopy measurement is performed using a 0.5 m Digikrom Spectrometer (CVI Laser Corp, USA. Digikrom Model DK 480). A Crystal Thickness Monitor (DTM-101) manufactured by HIND-HIVAC, Banglore, India monitored the deposition rate at various discharge conditions. The monitor head is placed at the same horizontal plane as the substrate holder.

4.3 Theory of ion acoustic wave in multi-component plasma

The propagation of the ion acoustic wave in the presence of negative ion is different than from the propagation in normal single component plasma. For the study of ion acoustic wave propagation, we assume that argon-oxygen magnetron plasma is effectively composed of Ar^+, O^- and electrons. The assumption is based on the fact that the density of Ar^+ and O^- ions is greater than the other positive and negative ions present in such plasma

[14]. In order to obtain the dispersion relation for ion acoustic wave in such plasma we can couple the continuity and momentum equation in to Poisons equation. For such cold plasma the Poisons equation can be expressed as,

$$\frac{\partial^2 \phi}{\partial x^2} = 4\pi e(n_e - n_1 + n_2)\,. \tag{4.2}$$

Here, n_e, n_1 and n_2 are electron, positive ion and negative ion density respectively.

After we perturb and linearize the continuity equation and momentum equation, and couple it to the Poisson's equation assuming the electrons to be Maxwellian, the Eq. (4.2) can be written as

$$-k^2\phi_1 = \frac{4\pi e^2 n_{e0}}{k_B T_e}\phi_1[1 - \frac{n_{10}}{n_{e0}}.\frac{k^2 k_B T_e}{m_- \omega^2 - 3k_B T_i k^2} - \frac{n_{20}}{n_{e0}}.\frac{k^2 k_B T_e}{m_+ \omega^2 - 3k_B T_i k^2}], \tag{4.3}$$

where n_{e0}, n_{10} and n_{20} are equilibrium density of the electron, positive ion and negative ion, respectively. If we assume such a multi-component plasma for n_0 positive ions with mass m_+, for εn_0 negative ions with mass m_-, and that includes $(1-\varepsilon)n_0$ electrons in equilibrium, the Eq. (4.3) can be expressed as

$$1 = -\frac{1}{k^2 \lambda_o^2}\left[1 - \frac{k^2 k_B T_e n^-}{m_- \omega^2 - 3k_B T_i k^2} - \frac{k^2 k_B T_e n^+}{(m_+ \omega^2 - 3k_B T_i k^2)}\right] \tag{4.4}$$

with $\lambda_o = \dfrac{\lambda_{Do}}{(1-\varepsilon)^{1/2}}$

where $\lambda_{Do}^2 = \dfrac{k_B T_e}{4\pi e^2 n_{eo}}$

and $\dfrac{n_{10}}{n_{eo}} = \dfrac{\varepsilon}{1-\varepsilon} = n^-$, $\quad \dfrac{n_{20}}{n_{eo}} = \dfrac{1}{1-\varepsilon} = n^+$, $\varepsilon = \dfrac{n_-}{n^+}$.

Eq.(4.4) can be written as

$$1=-\frac{1}{k^2\lambda_o^2}\left[1-\frac{k_B n^-}{m_+\left(\frac{m_-}{m_+}\frac{\omega^2}{k^2T_e}-\frac{3k_BT_i}{m_+T_e}\right)}-\frac{k_B n^+}{m_+\left(\frac{\omega^2}{T_ek^2}-\frac{3k_BT_i}{m_+T_e}\right)}\right]. \tag{4.5}$$

Again, Eq. (4.5) can be written as,

$$1=-\frac{1}{k^2\lambda_o^2}\left[1-\frac{n^-}{\left(\frac{m_-}{m_+}\frac{\omega^2}{k^2}\left(\frac{m_+}{T_ek_B}\right)-\frac{3T_i}{T_e}\right)}-\frac{n^+}{\left(\frac{\omega^2}{k^2}\left(\frac{m_+}{T_ek_B}\right)-\frac{3T_i}{T_e}\right)}\right]. \tag{4.6}$$

Here, $(\frac{k_BT_e}{m_+})^{1/2}$ is the ion sound velocity for the positive ions. Thus, the Eq. (4.6) becomes

$$1=-\frac{1}{k^2\lambda_o^2}\left[1-\frac{n^-}{m\frac{v_p^2}{c_s^2}-\gamma\tau}-\frac{n^+}{\frac{v_p^2}{c_s^2}-\gamma\tau}\right], \tag{4.7}$$

with

$$-k^2\lambda_o^2=\left[1-\frac{n^-}{mv^2-\gamma\tau}-\frac{n^+}{v^2-\gamma\tau}\right]. \tag{4.8}$$

where the symbols are defined as,

$v=\frac{v_p}{c_s}=\frac{w}{kc_s}$ with $c_s=\sqrt{k_BT_e/m_+}$ and $m=\frac{m_-}{m_+}$

Cooney et *al.* [15] obtained a similar kind of dispersion relation for the ion acoustic waves in such plasma, and obtained two branches of phase velocity. The speed of one branch (fast mode) increases and the speed of the other branch (slow mode) decreases with increasing ε.

In the slow mode, positive ions, negative ions and electrons oscillate in phase, while in the fast mode they oscillate out of phase. However, in the cold plasma the slow mode does not exist, and the fast mode phase velocity for the long wavelength reduces to [15]

$$v_f = c_s \sqrt{\frac{1+\varepsilon/m}{1-\varepsilon}} \, . \tag{4.9}$$

4.4 Description of ionic processes in oxygen containing argon plasma

To study the propagation of ion acoustic wave in oxygen added argon plasma, a study of various ionic processes in the oxygen added argon plasma is essential. When oxygen is added to argon, in addition to ground state Ar atoms, O_2 molecules, Ar^+, O_2^+ and O^+ ions, there exists the possibility of the various meta-stable atoms of Ar ($3d^5 4s^3 p_2$) at 11.55 eV above the ground state (denoted as Ar_m^*), oxygen molecules in two meta-stable states (O_2^m) at 0.977 and 1.672eV and oxygen atoms at the lowest meta-stable states (O^m) at 1.97eV [14]. The essential reactions in the scope of this study are mentioned in **Table 4.2**. The species of the Ar/O_2 plasma mentioned above undergo different chemical reactions with different rate constants and different relative cross sections. Before experimental analysis of the relative negative ion concentration, it is very important to discuss the relevant reaction routes for the formation and destruction of O^- present in such a plasma. Electron impact dissociative attachment of O_2 is the main production scheme of O^-, though to a lesser extent electron impact dissociation of O_2 is also responsible for the production of O^- ions [14].

$$e^- + O_2 \rightarrow O^- + O \tag{4.10}$$

$$e^- + O_2 \rightarrow O^- + O^+ + e^- \tag{4.11}$$

As shown by Panda et *al.* [16], the creation of O^- also takes place through dissociative attachment of a meta-stable oxygen molecule (O_2^m), which will likely be a very strong production channel in low electron temperatures. However, in the observed electron temperature range in this study (5.78-6.20 eV), the decay of a meta-stable oxygen molecule into pairs of neutral oxygen atoms is far more dominant than the creation of meta-stable molecules.

$$e^- + O_2^m \rightarrow O^- + O \qquad (4.12)$$

The O^- ions are chiefly lost via neutralization of Ar^+ ions throughout the volume of the discharge [3].

$$O^- + Ar^+ \rightarrow O + Ar \qquad (4.13)$$

However, in the downstream region of the magnetron discharge, the negative ions are lost by ion-ion recombination via the following routes [3]:

$$O^- + O_2^+ \rightarrow O + O_2 \qquad (4.14)$$

$$O^- + O_2^+ \rightarrow 3O \qquad (4.15)$$

$$O^- + O^+ \rightarrow 2O \qquad (4.16)$$

The electron impact dissociative ionization of O_2 is the main production mechanism for O^+, while charge transfer of Ar^+ with O_2 is responsible for the production of O_2^+ ions [14]. Therefore, it is reasonable that both ion densities increase as a function of increasing O_2 partial pressure in the discharge.

$$e^- + O_2 \rightarrow 2e^- + O^+ + O \qquad (4.17)$$

$$Ar^+ + O_2 \rightarrow Ar + O_2^+ \qquad (4.18)$$

Table 4.2: Reactions and rate coefficients

No.	Reaction	Rate Constant (K) ($cm^3 s^{-1}$)
1.	$e^- + Ar \rightarrow 2e^- + Ar^+$	4.4×10^{-10}
2.	$e^- + O_2 \rightarrow O^- + O$	$8.8\times 10^{-11}\exp(-4.4/T_e)$
3.	$e^- + O_2 \rightarrow O^- + O^+ + e^-$	$7.1\times 10^{-11}\sqrt{T_e}\exp(-17/T_e)$
4.	$e^- + O_2^m \rightarrow O^- + O$	$-1.69\times 10^{-12} + 6.72\times 10^{-10}/T_e$ $-1.30\times 10^{-10}/T_e^{\,2} + 9.60\times 10^{-12}/T_e^{\,3}$
5.	$O^- + Ar^+ \rightarrow O + Ar$	$2.7\times 10^{-7}\sqrt{300/T_g}$
6.	$O^- + O_2^+ \rightarrow O + O_2$	$2.0\times 10^{-7}\sqrt{300/T_g}$
7.	$O^- + O_2^+ \rightarrow 3O$	$2.0\times 10^{-7}\sqrt{300/T_g}$
8.	$O^- + O^+ \rightarrow 2O$	$2.7\times 10^{-7}\sqrt{300/T_g}$
9.	$e^- + O_2 \rightarrow 2e^- + O^+ + O$	$5.3\times 10^{-10}T_e^{\,0.9}\exp(-20/T_e)$
10.	$Ar^+ + O_2 \rightarrow Ar + O_2^+$	5×10^{-11}
11.	$O_2^+ + Ar \rightarrow O_2 + Ar^+$	2.1×10^{-11}
12.	$O^+ + Ar \rightarrow O + Ar^{+-}$	2.1×10^{-11}
13.	$e^- + O \rightarrow O^m + e^-$	$4.2\times 10^{-9}\exp(-2.25/T_e)$
14.	$O^- + O^+ \rightarrow O^m + O$	$2.7\times 10^{-7}\sqrt{300/T_g}$

Note that T_g is the gas temperature in K (Kelvin)

Concerning the loss of O^+ and O_2^+ ions, an asymmetric charge transfer with an Ar atom is found to be the most significant process compared to other possible processes [14].

$$O_2^+ + Ar \rightarrow O_2 + Ar^+ \qquad (4.19)$$

$$O^+ + Ar \rightarrow O + Ar^+ \qquad (4.20)$$

The meta-stable oxygen atoms (O^m) created in the discharge play an important role in determining the relative concentration of negative ions in the oxygen additive argon magnetron discharge plasma. Viteralu et *al.* [17] have shown that O^- ions produced at the target region of the magnetron discharge lead to O^m formation in the downstream region of the discharge via electron and argon stripping[18], followed by

$$e^- + O \rightarrow O^m + e^- . \qquad (4.21)$$

Again, lower energetic O^- ions formed due to electron attachment onto atoms [17] can set up another reaction route to O^m, given by

$$O^- + O^+ \rightarrow O^m + O \qquad (4.22)$$

with characteristic emission lines at 777 and 845 nm. In the literature, the intensity of the emission line at 777 nm is used as a representative of the relative density of negative oxygen ions in the discharge [19].

The steady state density of O^- ions at pressures lower than ~4 Pa can be given as

$$n^- = \frac{k_{da} n_e n_{o_2}}{k_{rec} n_+} \qquad (4.23)$$

where $k_{da} = 8.8\times10^{-17} \exp[-4.4/T_e]$ m^3s^{-1} and $k_{rec} \approx 2.5\times10^{-13} [300/T_g]^{1/2}$ m^3s^{-1} are the rate constants for dissociative attachment (Reaction 2 in **Table 4.2**) and ion–ion recombination (Reactions 5, 6 and 7 in **Table 4.2**), respectively [20-21]. Here, T_e is the electron

temperature in eV, T_g is the neutral temperature in Kelvin, and n_{o_2} is the neutral density of oxygen. In deriving this equation, it is assumed that for the conditions of electron temperature and working pressure existing in our investigation, the dissociative attachment of O_2 is dominant over other production channels for O^-. Here, n^- is the density of O^- ions in the discharge, n_+ is the total positive ion density $(n_+ = n_{Ar^+} + n_{o_2^+} + n_{o^+})$ where the symbol represents the corresponding density of ions. Due to similar reaction rate coefficients of negative O^- ion recombination with Ar^+, O^+ and O_2^+ ions (Reactions 5, 6 and 7 in **Table 4.2**) we can assume a single rate constant (k_{rec}) for such processes. If we take $\gamma = n^-(n^+ - n^-)^{-1}$, it will represent the electro-negativity of the discharge. Then Eq. (4.23) can be stated as

$$n^- = \frac{k_{da} n_{o_2}}{k_{rec}(1+\gamma)} \tag{4.24}$$

When $\gamma \ll 1$, as in this work, $n^- \propto n_{o_2} \propto P_{o_2}$, where P_{O_2} is the partial pressure of the oxygen in the discharge. Thus, a gradual increase in the oxygen negative ion density is expected with an increase in the oxygen partial pressure.

4.5 Results and discussions

4.5.1 Measurement of the relative concentration of ion using ion acoustic wave diagnostics

In this investigation the fast mode phase velocities (v_f) of the grid excited ion acoustic waves are used to determine the relative concentration of negative ions. The fast mode phase velocity of ion acoustic wave in such plasma is given by the Eq. (4.9). With the help of the mentioned equation, determination of the relative density of negative ion is possible

provided the ion sound velocity for pristine argon plasma is known. In the pristine argon plasma, at first the compressive linear perturbations are excited for a transient, weak ($3.0V$ and $10\mu s$) sinusoidal excitation pulse. **Fig. 4.1(a)** shows the evolution of a compressive pulse for the applied excitation amplitude detected as the maximum normalized density fluctuation ($\frac{\partial n_e}{n_e} \langle 0.05$) by the positively biased Langmuir probe at a different distance (2-8 cm) from the grid. Due to the damping in plasma media the amplitude of the perturbation decreases as it travels further from the excitation grid. Using the time-of-flight technique, the ion sound velocity for pristine argon plasma is measured and found to be (2.26 ± 0.19) $\times 10^5$ cm/s for the pure argon plasma. The measured value of ion sound velocity is within the range limited by the expression $c_s = \sqrt{\frac{kT_e}{M_i}}$. After studying the linear characteristic of wave propagation, an attempt was made to study the non-linear propagation of wave by increasing the amplitude of the applied pulse [22]. **Fig. 4.1(b)** shows the detected signals at the location X = 6 cm for different excitation voltages (V_{ex}) of the applied positive pulse. It is observed that the velocity of the wave increases and the width of the wave become narrower with increasing wave amplitude. These are the properties of the propagation of the ion acoustic soliton [2]. A soliton is a non-linear ion acoustic wave which results due to the delicate balance between the non-linearity and dispersion present in the plasma medium. The non- linearity in the wave increases with increasing wave amplitude. Also, when the wave propagates away from the exciting grid, the role of dispersion becomes larger. Soliton is formed at the distance where the non-linearity is balanced by the dispersion present in the plasma medium (in this case at a distance of 6 cm from the centre of the exciting grid in

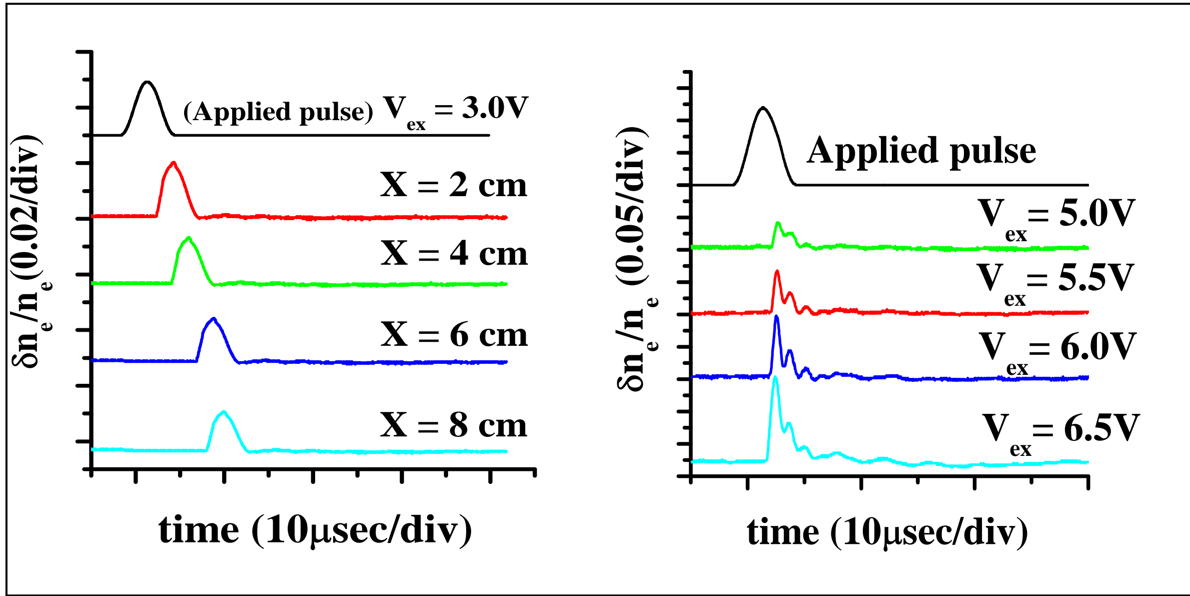

Figure 4.1(a) Observed signals at several distances from the grid for an initial positive sinusoidal pulse (V_{ex} = 3.0V) in pure argon plasma. Partial pressure of argon P_{Ar} = 8x10^{-2} Pa. (b) Detected signal at different amplitudes of the positive excited signal V_{ex} in oxygen added argon plasma. The probe is fixed at X = 6 cm. Top trace is applied signal (not to scale).

this study). The evaluation of an initial perturbation with increasing negative ion concentration is shown in **Fig. 4.2.** The planar probe is fixed at X = 6 cm for an excitation voltage (V_{ex}) of 6.5 V. It is found that the phase velocity of the ion acoustic wave in the presence of negative ions is faster than in pure argon plasma. Another important observation is the increase in phase velocity with an increasing negative ion concentration (**Fig. 4.3**). With the addition of oxygen into the pure argon plasma, there is a gradual decrease of electron density, which decreases the resistance to positive ion motion. As a result, the phase velocity of the fast mode increases gradually with the oxygen partial pressure though its amplitude is slightly reduced. The phase velocity is calculated from the mentioned time-of-flight technique in the presence of negative ions. The measured values of the phase velocities at the conditions with oxygen partial pressure of 4×10^{-3} Pa, 6×10^{-3}

and 8 $\times 10^{-3}$ are inserted in the Eq. (4.9) to calculate the values of ε and are found to be 0.042, 0.067 and 0.082 respectively.

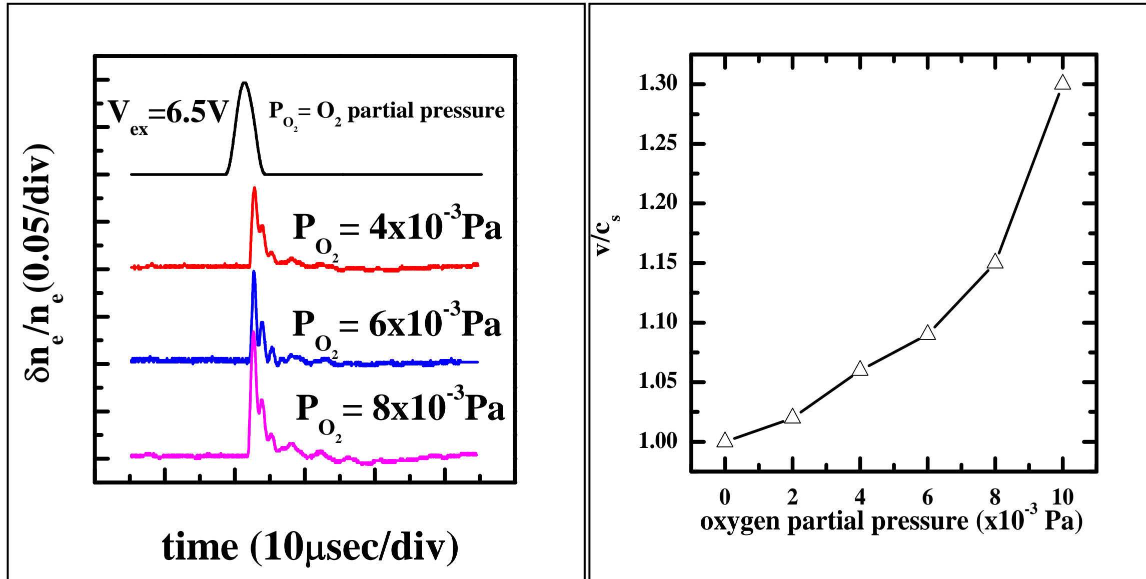

Figure 4.2 Observed signals at X = 6 cm from the grid for an initial pulse (V_{ex} = 6.5V) at different oxygen partial pressure. Partial pressure of argon P_{Ar} = 8$\times 10^{-2}$ Pa. Top trace is the applied pulse (not to scale)

Figure 4.3 Variation of Mach number of the ion acoustic wave (v/c_s) as a function of oxygen partial pressure.

4.5.2 Langmuir probe and optical emission spectroscopy measurement

As oxygen is added to pure argon plasma, the Langmuir probe current-voltage (I-V) plot and its plasma parameters begin to change. The procedure to determine the electron density and electron temperature from the I-V characteristics of the Langmuir probe is mentioned in the Chapter 3 and the electron density is found to decrease with an increase of the oxygen partial pressure in the discharge (**Fig. 4.4**). Because the ionization potential of oxygen is lower than that of argon, a gradual decrease of electron temperature from 6.20 to 5.78 eV is also observed upon oxygen addition. This effect has been nicely explained by

Aijaz et *al.* [23] when adding a gas with a higher ionization potential compared to Ar. The electron saturation current reduces as a function of oxygen addition and in addition, the

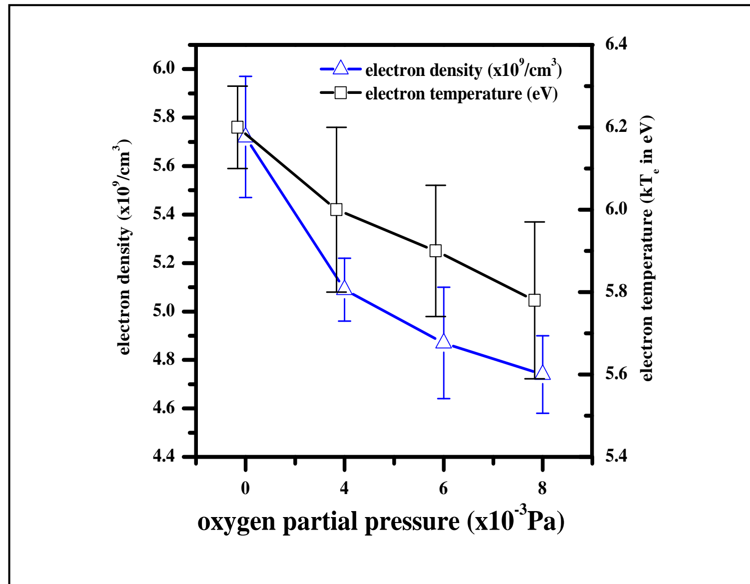

Figure 4.4 Electron density and electron temperature as a function of oxygen partial pressure in the discharge.

plasma potential decreases and the floating potential become more negative. The plasma potential is determined by using the zero second derivative of the I-V plot. It is defined as the voltage at which the second derivative, d^2I/dV^2 goes to zero. The modulation of the plasma potential and the floating potential are shown in the **Fig. 4.5**. In a pure argon discharge, the plasma potential is found to be positive because the loss of highly mobile electrons leaves the plasma with a net positive charge. However, with the introduction of oxygen, the electron density decreases as electrons are replaced with negative oxygen ions. Although there is no change in the quasi-neutrality condition, a corresponding fall of plasma potential is observed in this case because negative oxygen ions have a smaller thermal velocity than the electron. Therefore, the loss rate of the negative species decreases,

and the bulk plasma adjusts itself to compensate for this loss rate. The modulation of the floating potential is found to be similar to that of the plasma potential.

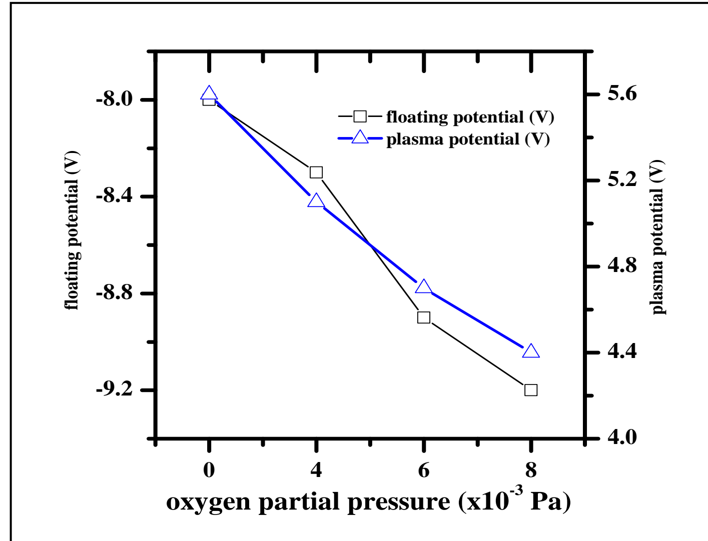

Figure 4.5 Plasma potential and floating potential variations as a function of oxygen partial pressure in the discharge

As the oxygen added argon plasma consists of various types of positive (Ar^+, O_2^+ and O^+) and O^- ions, rather than calculating the individual density we have obtained the group density. The procedure of dividing the ions into two groups and calculation of ion density using mean ion mass procedure was already explained in the Chapter 2. For oxygen added argon plasma, the heavy ion group consists of Ar^+ and O_2^+ while, O^- ions are included in the light ion group. From the Langmuir probe I-V characteristics using the procedure followed in the Chapter 3, the total heavy ion density in the discharge can be easily evaluated, and is given in the **Fig 4.6**. In this investigation, the partial pressure of oxygen is much smaller than the partial pressure of argon (less than 1:10). Therefore, it is reasonable to expect that the Ar^+ ion density is greater than the oxygen positive ion density in this discharge. For

such multi-component plasma the density of ions varies as: $n_{Ar^+} >> n_{O_2}{}^+ > n_{O^+}$ [14] where the symbol represents the density of the corresponding ions. However, with the addition of oxygen at a fixed argon partial pressure, the density of the oxygen positive ions should increase [24] for obvious reason. Since the majority of the charge carriers in the discharge are Ar^+ ions, the density modulation of heavy ions is more indicative of Ar^+ density variation as is found in the **Fig. 4.6**.

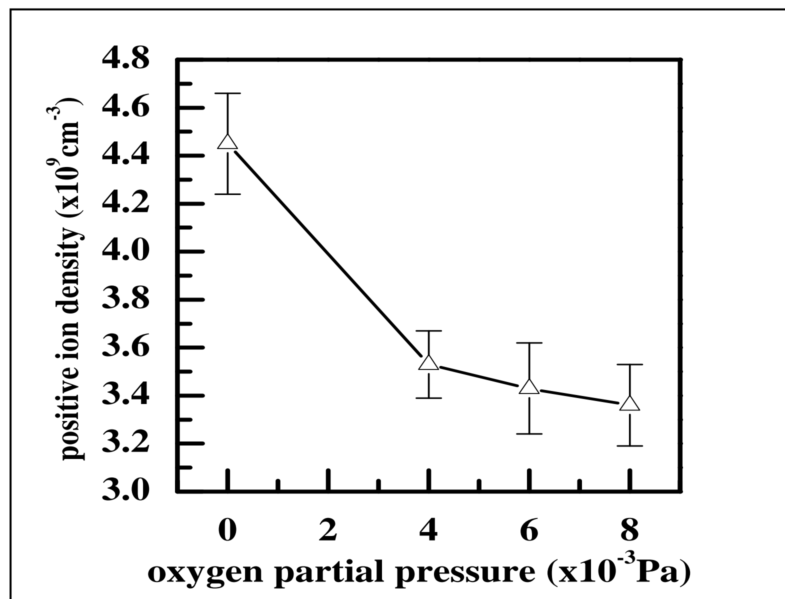

Figure 4.6 Modulation of total heavy positive ion density as a function of oxygen partial pressure in the discharge.

Optical emission spectroscopy (OES) is an excellent non-intrusive technique used to determine the concentration of plasma species. To a good approximation the emission intensity of a particular line of an element is considered to be proportional to the density of that particular species in a low pressure discharge [25-26]. The experimental arrangement to probe the plasma with optical emission spectroscopy is explained in details in the Chapter 2. The aim of the OES scan is to qualitatively investigate the density variation of

the Ar^+ as well as the O^- ions in the discharge. In argon-oxygen magnetron discharge the most prominent excited species are: Ar I lines corresponds to atomic argon emission(696.45 nm, 738.39 nm,751.46 nm,763.51 nm,772.37 nm,794.81 nm,801.47 nm,811.53 nm,826.45 nm,840.42 nm, and 852.14 nm), Ar II lines correspond to Ar^+ ionic emission (434.80 nm, 454.15 nm, 472.68 nm, 476.48 nm, 488.0 nm), Ti I line (499.5 nm, 510.53 nm), and excited oxygen atoms with characteristic emission lines at 777 nm and 845 nm [19].

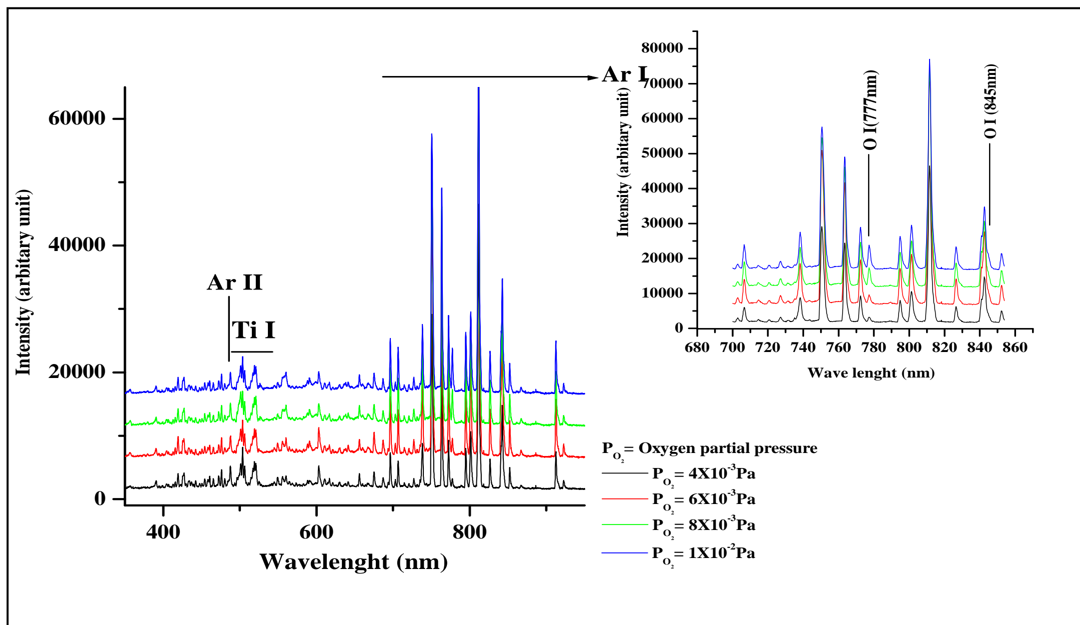

Figure 4.7 The emission lines of the spectra collected for the oxygen added argon plasma at different oxygen partial pressure. The argon partial pressure was kept fixed at 8×10^{-2}Pa. The emitting species were identified by comparing with NIST database. The variation in the relative intensities O I line could be observed.

The typical OES scan of the oxygen added argon plasma is shown in the **Fig. 4.7**. To estimate the value of degree of ionization and relative negative ion density, the intensity of

neutral excited species Ar, O and Ar^+ excited ions are considered at 751.46, 777 and 488 nm, respectively. By following the reaction given in Eq. (4.22), it is clear that the intensity of the emission line at 777 nm is representative of the relative density of negative oxygen ions in the discharge. The intensity ratios of the lines of the excited species of Ar^+ and O to the neutral line of Ar at 751.46 nm are given in the **Fig. 4.8**. This ratio is taken to remove any effect due to the evolution of the plasma parameters as a function of different discharge conditions, thereby creating a trend of modulation of the negative oxygen and Ar^+ ion concentration that is meaningful. It is clear from the **Fig. 4.8** that the oxygen negative ion density increases linearly with oxygen partial pressure, while the Ar^+ ion density follows the opposite trend. This fact leads to a gradual increase in the relative in the relative concentration of oxygen negative ions as a function of the oxygen partial pressure.

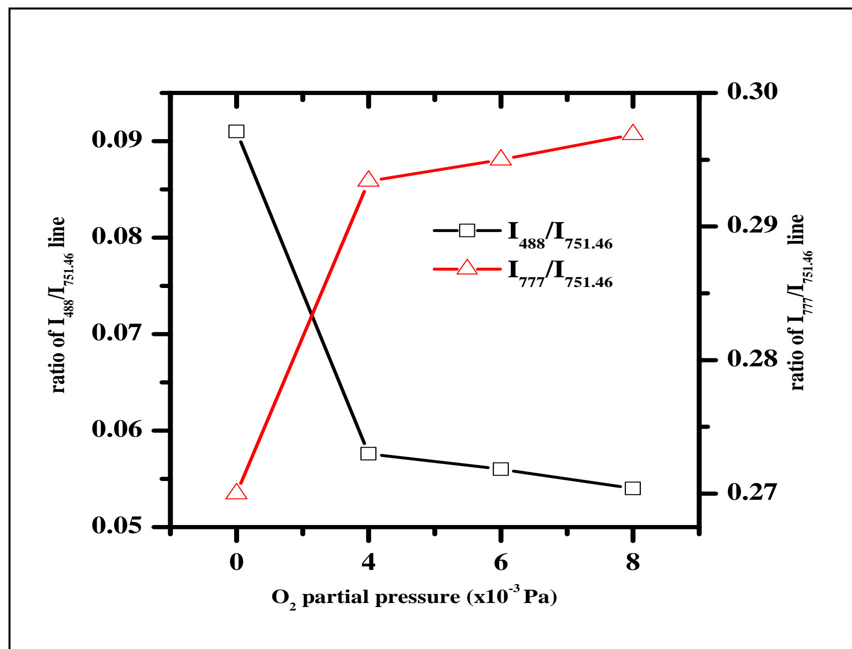

Figure 4.8 Influence of oxygen partial pressure on the intensity (I) ratio of the 777 oxygen atomic line to 751.46 nm argon line and 488 Argon line to 751.46 nm argon line.

To benchmark the values of the relative negative ion concentration measured by the ion acoustic waves, we have substituted the values of positive ion density (n_+) and electron density (n_e) as obtained by the Langmuir probe in Eq. (4.23). The ratios of the negative to positive ion density in our plasma are found to increase from 0.0318 to 0.0877 (**Fig. 4.9**). The similarity observed in the values ε, measured by the Langmuir probe and the ion acoustic wave analysis justifies the effectiveness of the ion acoustic wave analysis as a probe for magnetron plasma discharge.

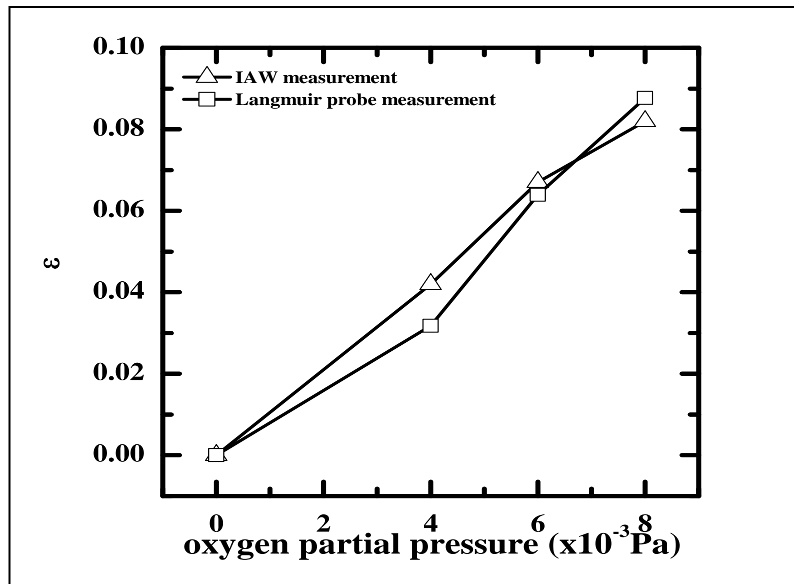

Figure 4.9 Comparison of the ratio of oxygen negative ion to positive ions (ε) measured by Langmuir probe diagnostic and IAW diagnostic as a function of oxygen partial pressure in the discharge.

4.6 Conclusion

Ion acoustic phase velocity, wavelength and frequency have been the basis of various plasma diagnostics for a long time. In this investigation, we used the temporal behavior of ion acoustic waves to provide the relative negative ion concentration in magnetron discharge plasma. With the addition of oxygen into the pure argon discharge, a gradual

decrease of the electron density, plasma potential, floating potential and electron temperature are observed, indicating the presence of negative ions in this plasma. Optical emission spectroscopy further confirms the gradual increase of the negative ion density as a function of the oxygen partial pressure. The relative negative ion concentration is determined by exciting ion acoustic waves in the downstream region of the discharge, and the phase velocity of the ion acoustic wave is found to scale linearly with the increase of the oxygen partial pressure in the discharge. This corresponds to an increase of the relative negative ion concentration (ε) value from 0.042 to 0.082. We also calculated the values of ε separately at each discharge condition using a cylindrical Langmuir probe. The measured values of relative negative ion density by the ion acoustic wave diagnostics and the Langmuir probe show good agreement.

References

[1] N. Hershkowitz and Y-C. Ghim, Plasma Sources Sci. Technol. **18** (2009) 014018.

[2] S. K. Sharma, and H. Bailung, Phys. Plasmas **17,** 032301 (2010).

[3] S. Scribbins, M. Bows, and J. W. Bradley, J. Phys. D: Appl. Phys. **46,** 045203 (2013).

[4] R. S. Nowicki, J. Vac. Sci. Technol. **14**, 127 (1977).

[5] R. K. Waits, J. Vac. Sci. Technol. **15**, 179 (1978).

[6] C. Deshpandey, and L. Holland, Thin Solid Films **96**, 265 (1982).

[7] R. Dodd, S. D. You, and J. W. Bradley, Thin Solid Films **519,** 1705 (2010).

[8] D. Depla, G. Buyle, J. Haemers, and R. De Gryse, Surf. Coat. Technol. **200,** 4329 (2006).

[9] S. Maniv, and W. B. Westwood, J. Vac. Sci. Tecnol. A **17,** 1019 (1989).

[10] P. J. Kelly, and R. D. Arnell, Vacuum **56,** 159 (2000).

[11] N. C. Adhikari, M. K. Deka, and H. Bailung, Phys. Plasmas **16,** 063701 (2009).

[12] Y. Nakamura, T. Ddagiri, and I. Tsukabayashi, Plasma. Phys. Control. Fusion **39,** 105 (1997).

[13] L. Schott, Phys. Fluids B **3,** 236 (1991).

[14] A. Bogaerts, Spectrochim. Acta Part B **64,** 1266 (2009).

[15] J. L. Cooney, D. W. Aossey, J. E. William, M. T. Gavin, H. S. Kim, Y. C. Hsu, A. Scheller, and K. E. Lonngremi, Plasma Sources Sci. Technol. **2**, 73 (1993).

[16] S. Panda, D. J. Economou, and M. Meyyappan, J. Appl. Phys. **87,** 8323 (2000).

[17] C. Vitelaru, D. Lundin, Nils Brenning, and T. Minea, Appl. Phys. Lett **103,** 104105 (2013).

[18] G. C. Tisone and L. M. Branscomb, Phys. Rev. **170,** 169 (1968).

[19] T. Ishikawa, D. Hayashi, K. Sasaki, and M. Kadota, Appl. Phys. Lett. **72,** 2391(1998).

[20] S. D. You, R. Dodd, A. Edwards, and J. W. Bradley, J. Phys. D: Appl. Phys. **43,** 505205 (2000).

[21] R. Dodd, S. D. You, P M Brayant, and J. W. Bradley, Plasma Source Sci. Technol. **19,** 015021 (2010).

[22] M. K. Deka, N. C. Adhikary , A. P. Misra, H. Bailung and Y. Nakamura Phys. Plasmas **19,** 103704 (2012).

[23] J. A. Aijaz, K. Sarakinos, O. Lunden, N. Brenning, and U. Helmersson, Diam. Relat. Mater. **23,** 1 (2012).

[24] H. Kakati, A. R. Pal, H. Bailung, and J. Chutiya, J. Appl. Phys. **101,** 083304 (2007).

[25] J. W. Coburn and M. Chen, J. Appl. Phys. **51**, 3134 (1980).

[26] G. Zambrano, H. Riascos, P. Prieto, E. Restrepo, A. Devia, and C. Rincon, Surf. Coat.Technol. **172**, 144 (2003).

CHAPTER 5

Effect of process parameters on the properties of argon–nitrogen plasma for titanium nitride film deposition

Chapter 3 and Chapter 4 were focused on the plasma properties of the hydrogen additive argon and oxygen additive argon magnetron discharge among the other things. In this chapter, plasma parameters of the nitrogen additive argon plasma are studied and a correlation of the orientation of the deposited titanium nitride thin film with plasma parameter is achieved.

5.1 Introduction

Reactive sputtering is actively used where the compound thin films of metal oxides and metal nitrides are required. For this purpose, reactive gases such as nitrogen, oxygen are added in a controlled manner in the argon glow discharge. Reactive gas addition to the argon magnetron discharge plasma is in fact a non-linear and complex process which involves many interdependent parameters [1]. The complexity arises due to the discharge behavior of the compound gases and its related plasma species. Thus, the basic physical mechanism in reactive sputtering in the background of the multi-component plasma is still an interesting topic of research. In this chapter, the delicate dependence of the plasma parameters (ion density profiles for electron and ions, electron temperature) on the addition of nitrogen gas to the argon discharge is investigated. At the low values for reactive gas flow rate, the reactive gas partial pressure is independent of the flow rate as all the available reactive gas is gettered at the condensation sites of the magnetron target [1]. When the flow rates of the reactive gas into the chamber is higher than the gettering rate of the sputtered metal, the reactive gas then reacts with the target surface to form a layer of the gas-metal

compound. The formation of the compound layer on the target is a function of the reactive gas addition. The compound layers have higher ion induced secondary electron emission coefficient (ISEE) than the pure metals. From the investigation presented in the Chapter 3, it is clear that the ISEE coefficient determines the plasma parameters in the bulk region of the magnetron discharge. As such, the compound layer formed on the target can influence the evaluation of the plasma parameters independently in the reactive sputtering [2]. As the working pressure is one of the most important experimental parameters in reactive sputtering, the aim of this investigation is to optimize the working pressure and the corresponding plasma parameters for preferred orientation of poly-crystalline TiN along the (111) diffraction plane on AISI M2 high steel speed substrate. The selection of TiN (111) diffraction plane is based on the fact that the hardness and resistivity of the TiN thin film deposited by magnetron sputtering mostly depends upon on the orientation of this plane [3]. As mentioned in Chapter 3, the optical emission spectroscopy (OES) and Langmuir probe are very popular plasma diagnostic techniques because of their accuracy and simplicity. Both electron temperature (T_e) and electron density (n_e) can be measured using a Langmuir probe. On the other hand, OES can deal with the emissions from excited species of plasma. As mentioned already, the target effect [2] needs to be taken into account while investigating the plasma parameters in the reactive sputtering. The optimization of plasma parameters with the orientation of the thin film in reactive sputtering will be meaningful only if the influence of the target on the evaluation of plasma parameters is minimal. One way of achieving it is to keep the ratio of N_2 to Ar flow rate constant during the deposition of titanium nitride thin film as done in this investigation. It is because it will not change the

composition of the compound layer formed on the magnetron target. In the next section 5.2 the details of the experimental arrangements are given. Detail discussion of ionic processes in nitrogen containing argon plasma has been discussed in the section 5.3. Then, the following section (5.4) contains the results and discussions. The findings of the chapter are summarized in the section 5.5.

5.2 Experimental set-up and diagnostic procedure

The details of the experimental set up to study the effect of target on plasma parameters of the hydrogen added argon DC planar magnetron plasma have been described in the section 2.2 of the Chapter 2. The water cooled Ti target of diameter 70mm is used as the cathode of the planar magnetron sputtering system. During the TiN deposition on THE AISI M2 high speed steel substrate, Ar and N_2 are fed into the deposition chamber by two digital mass flow controllers (Aalborg Make). The chamber is evacuated by a diffusion pump backed by a rotary pump up to a base pressure of 10^{-4} Pa. In the present study, keeping the N_2 to Ar flow ratio (1:5) in the discharge constant, the working pressure is varied from 3×10^{-1} Pa to 8×10^{-1} Pa at a fixed input power of 300 W. A single cylindrical probe with a length of 3.0mm and a radius of 0.1mm is installed in the discharge chamber to probe the plasma parameters. To estimate the relative contribution of nitrogen ions and argon ions in the plasma due to the mixing of different percentage of nitrogen gas in the argon plasma through measuring the intensity level of specific emission, a 1/2 m digikrom spectrometer (CVI Laser Corp, USA, Digikrom Model DK 480) is used. The deposition rate at various discharge conditions is monitored by a crystal thickness monitor (DTM-101) made by HIND-HIVAC, Bangalore. The phase composition of all the treated samples are studied by X-ray diffraction (XRD) using a XRD3000PTS diffractometer with the Cu–Ka radiation (λ

= 1.5406A°) in the Bragg–Brentano configuration operated at 40 keV and 50 mA. The XRD patterns are recorded with step durations of 4 s at each step in the angular range of 30^0-90^0.

5.3 Description of ionic processes in the N_2 containing argon plasma

To discuss the effect of nitrogen addition in the evaluation of the plasma parameters of the magnetron device, knowledge of the various ionic processes in nitrogen added argon plasma is very essential. When N_2 is added to pure Ar, besides Ar atoms in the ground state (gs) and excited to the meta-stable ($3p^5 4s\ ^3P_2$) level at 11.52 eV, Ar^+ ions, electrons, and several nitrogen species, i.e., four types of ions (N^+, N_2^+, N_3^+, and N_4^+), the gs N atoms, as well as N_2 molecules in gs and in various electronically excited levels [4] are also likely to be present. All those species present in plasma undergo different chemical reactions and the list of reactions essential for the present work is mentioned in **Table 5.1**. The major production mechanism for electron as well as Ar^+ is electron impact ionization, while the electron impact ionization of N_2 and dissociative ionization of N_2 play a minor role. It is due to the fact that the relative cross section for electron impact ionization of Ar [5] (1.25×10^{-16}cm^2) is one order greater than the corresponding value of relative cross section (10^{-17} cm^2) for electron impact ionization and dissociative ionization of N_2 [6]. In such plasma, charge transfer due to impact of Ar on N_2^+ (due to Reaction 2 in **Table 5.1**) becomes dominant to electron impact ionization for production of Ar^+ in higher nitrogen concentration [4]. Electrons are mainly lost due to dissociative recombination with N_2^+ (due to Reaction 3 in **Table 5.1**) while recombination with N_3^+ and N_4^+ and three body recombination with N^+ plays very minor role in its loss mechanism. Although the rate

constant for different electron–nitrogen containing ions recombination reactions are similar [7, 8] due to higher density of N_2^+ ($N_2^+ > N^+ > N_4^+ > N_3^+$) [4, 9] compared to other nitrogen ions, Reaction 3 becomes more significant in such plasma.

Table 5.1 : Ar^+, N_2^+ and N^+ ion production and loss processes

No.	Reaction	Rate Constant (K)	Name
1	$e^- + Ar \rightarrow e^- + Ar^+ + e^-$	4.40×10^{-10} cm^3s^{-1}	Ionization [9]
2	$N_2^+ + Ar \rightarrow Ar^+ + N_2$	2.81×10^{-10} cm^3s^{-1}	Charge Transfer [4]
3	$e^- + N_2^+ \rightarrow N + N$	$4.8\times 10^{-7} (\frac{300}{T_e})^{1/2}$ cm^3s^{-1}	Recombination [4]
4	$e^- + N_3^+ \rightarrow N_2 + N$	$2.0\times 10^{-7} (\frac{300}{T_e})^{1/2}$ cm^3s^{-1}	Recombination [4]
5	$Ar^+ + N_2 \rightarrow Ar + N_2^+$	4.45×10^{-10} cm^3s^{-1}	Charge Transfer [4]
6	$Ar^+ + N \rightarrow Ar + N^+$	4.45×10^{-10} cm^3s^{-1}	Charge Transfer [4]
7	$N^+ + N_2 \rightarrow N + N_2^+$	1.0×10^{-7} cm^3s^{-1}	Charge Transfer [4]
8	$N^+ + Ar \rightarrow Ar^+ + N$	6.0×10^{-14} cm^3s^{-1}	Charge Transfer [4]
9	$e^- + N_4^+ \rightarrow N_2 + N_2$	$2.0\times 10^{-6} (\frac{300}{T_e})^{1/2}$ cm^3s^{-1}	Recombination [4]

Charge transfer with N_2 (due to Reaction 5 in **Table 5.1**) is significant Ar^+ loss mechanism while charge transfer with N (due to Reaction 6 in **Table 5.1**) also plays a crucial part in this phenomenon [10]. These two processes are also the dominant production mechanism for N^+ and N_2^+.

5.4 Results and Discussions

5.4.1 Langmuir probe study

A cylindrical Langmuir probe is used to calculate electron temperature ($k_B\ T_e$ in eV) and electron density (n_e) at various working pressures in the substrate vicinity of nitrogen added argon plasma. The procedure to determine $k_B\ T_e$ and n_e at various working pressure is already explained in the preceding chapters. **Fig. 5.1** shows the evaluation of $k_B\ T_e$ and n_e as a function of various deposition parameters. As done in Chapter 3, in order to explain the modulation of plasma parameters as a function of working pressure it is necessary to compare the results with the pristine argon plasma. As seen from **Fig. 5.1** with increasing working pressure, the electron density value increases gradually from 1×10^{15} to 2.48×10^{15} m^{-3} for pristine argon plasma while it drops from 1×10^{15} to 6.4×10^{14} m^{-3} for nitrogen added argon plasma. Although the Ar to N_2 ratio is kept constant at all discharge conditions, the drop in electron density indeed signify that at higher working pressure, the loss mechanism of electrons (Reaction 3) is dominant over the different electron production mechanisms already described.

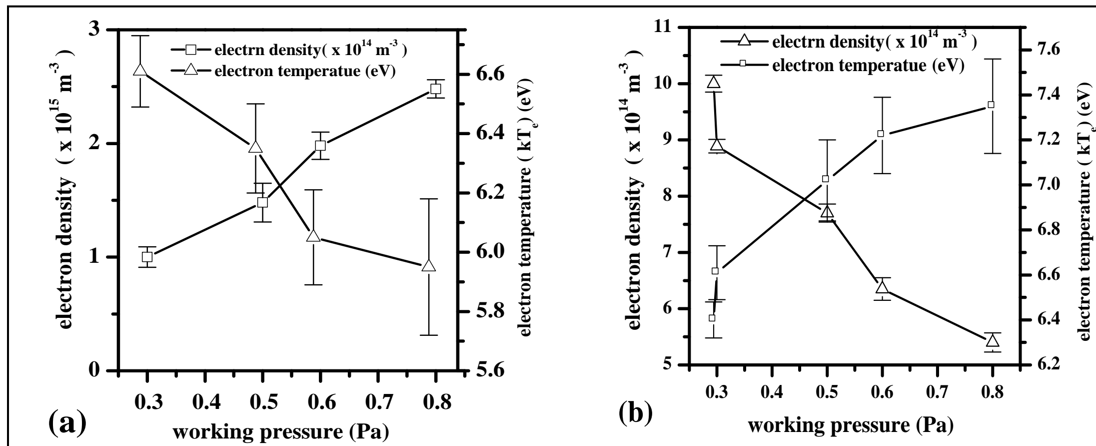

Figure 5.1 Electron temperature ($k_B T_e$) and electron density (n_e) as a function of working pressure (a) for pristine argon plasma (b) nitrogen added argon plasma.

This is due to high rate coefficient value of recombination process compared to the electron production mechanism [4]. For different working pressure conditions in such plasma, a prominent change of electron temperature is also observed. The gradual decrease/increase of the electron temperature with working pressure is due to the resulting increase/drop in electron density for the pristine and nitrogen added argon plasma respectively. It is observed that, the inverse relation between the electron density and temperature is maintained for such plasma. As the electron density decreases as a function of working pressure, the ion density should follow the similar behavior if one refers to the quasi-neutrality property of plasma. Since Ar/N_2 plasma contains various ion species (Ar^+, N^+, N_2^+, N_3^+ etc.), it is not possible to calculate the individual density of each ion by the Langmuir probe diagnostics. Therefore, following the same procedure as done in Chapter 3, the group density of ion is obtained. In this case, one group consists of Ar^+ ions and the other group consists of N_2 containing ions (N^+, N_2^+, N_3^+ etc.). The group density depends on the mean ion mass. Thus, using the ion saturation current ($I_{is}(V)$), electron temperature (T_e) and ion density (n_i) values, the mean ion mass is calculated [9] and it is found to decrease from 40 a. m. u to 31.71 a. m. u with increasing working pressure. From this data and using the fact that n_i is the sum of Ar (Ar^+) and N_2 containing ions (N^+, N_2^+, N_3^+ etc.), the Argon ion density in the discharge is easily found and given **Fig. 5.2**. It is interesting to note that with increasing working pressure the Ar^+ ion density decreases linearly from 1.0×10^{15} to 4.15×10^{14} m^{-3} and is because of the fact that the density of electrons that are mostly responsible for Ar^+ ion creation decreases with working pressure. As the nitrogen to argon partial pressure ratio is kept constant, it is reasonable to expect that

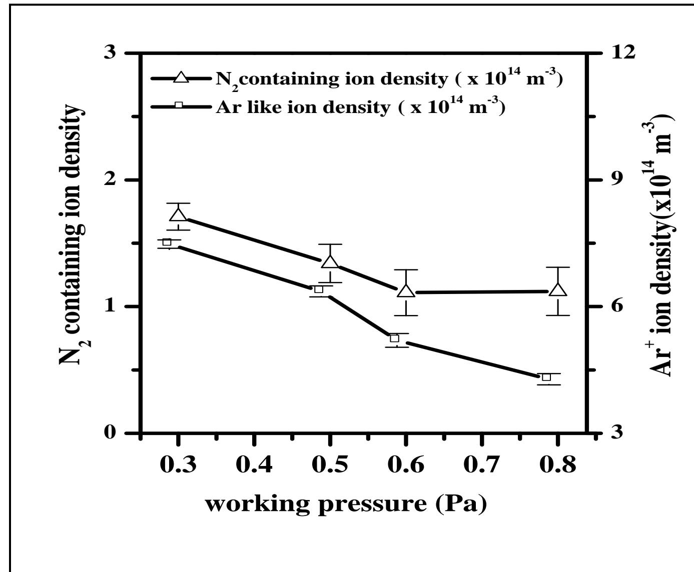

Figure 5.2 Influence of working pressure on the modulation of the argon and nitrogen containing ion density. The density of each group of ions is calculated using the mean ion mass procedure as explained in the chapter 2.

N_2 containing ions density modulation follows the similar trend as that of Ar^+ ion density. However it is found that initially N_2 containing ions density decreases from $1.71\times10^{14}\,m^{-3}$ at 3.0×10^{-1} Pa to $1.12\times10^{14}\,m^{-3}$ at 6.0×10^{-1} Pa; and after that the modulation of its density is not very significant (**Fig. 5.2**).

5.4.2 Optical emission spectroscopy study

As already mentioned in the preceding Chapters, the nitrogen added argon plasma is scanned at various working pressure conditions to investigate the qualitative variation of the degree of ionization. Typical OES spectra for nitrogen added argon plasma is shown in the **Fig. 5.3**. In argon-nitrogen magnetron discharge the most prominent excited species are: Ar I lines corresponds to atomic argon

emission(696.45 nm, 738.39 nm,751.46 nm,763.51 nm,772.37 nm,794.81 nm,801.47 nm,811.53 nm,826.45 nm,840.42 nm, and 852.14 nm), Ar II lines correspond to Ar^+ ionic emission (434.80 nm, 476.4 nm, 480.60 nm), Ti I line (499.5 nm, 510.53 nm), N_2^+ emission at 391.4 nm, and N_2 emission at 357.5 nm. The line intensity ratio between two suitable spectral lines is used to estimate the value of the degree of ionization. **Fig. 5.4** shows the variation of Ar I line (751.46nm) and Ar II line (476.4 nm) intensity as a function of working pressure. Here, the intensity ratio (δ) of Argon spectral line at 476.4 nm (Ar II) to at 751.46 (Ar I) is used to estimate the value of the degree of ionization [11]. These two lines are selected as the excitation thresholds for them are almost equal, and the transition probabilities ($6.4\times10^7 sec^{-1}$ at 476.4nm and $8.0\times10^7 sec^{-1}$ at 751.38 nm respectively) are similar [12, 13].

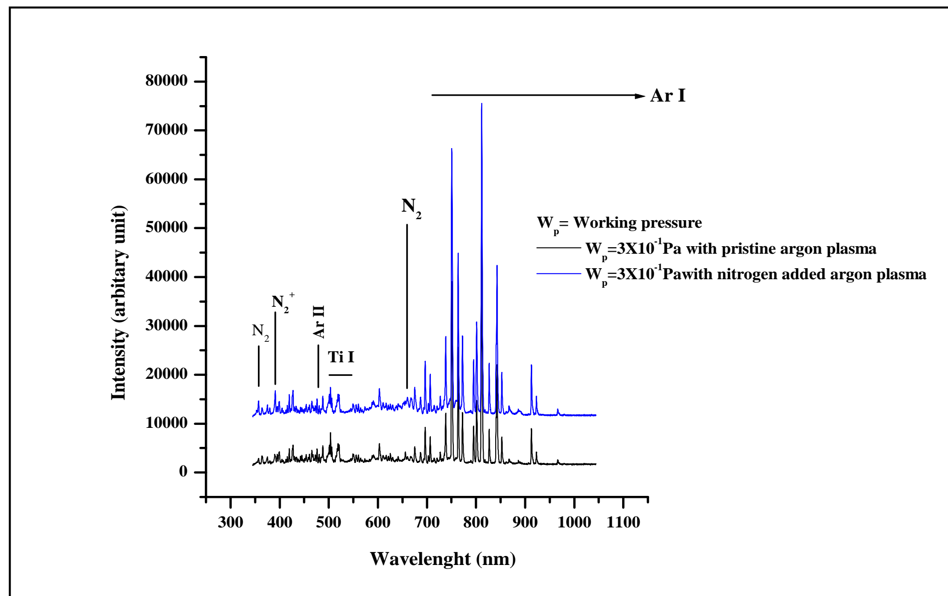

Figure 5.3 The emission lines of the spectra collected for the pristine and nitrogen added argon plasma at working pressure of 4×10^{-1} Pa. The emitting species were identified by comparing with the NIST database.

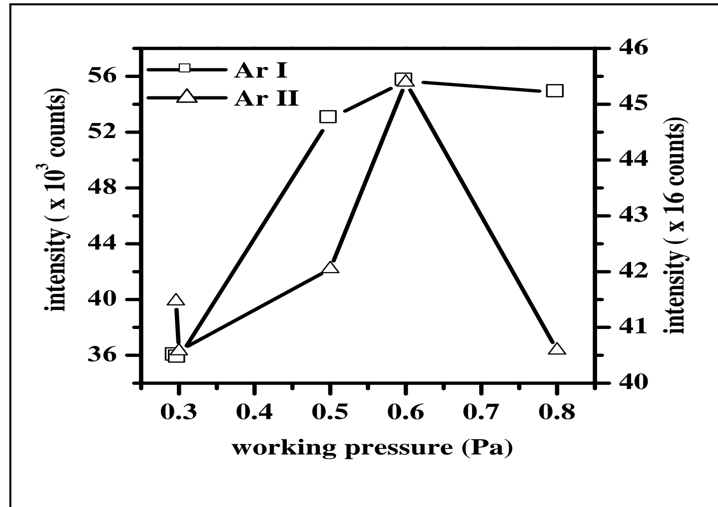

Figure 5.4 Observed intensity of atomic argon line at 476.4nm (Ar II) and at 751.46 nm (Ar I) line as a function of working pressure.

Fig. 5.5 shows that with increase of working pressure, δ decreases from 7.2×10^{-2} to 4.6×10^{-2}. This is expected because the Langmuir probe study already indicates a gradual decrease of Ar^+ ion density with working pressure and corresponding decrease in the degree of Argon ionization in the discharge as found by the OES diagnostics.

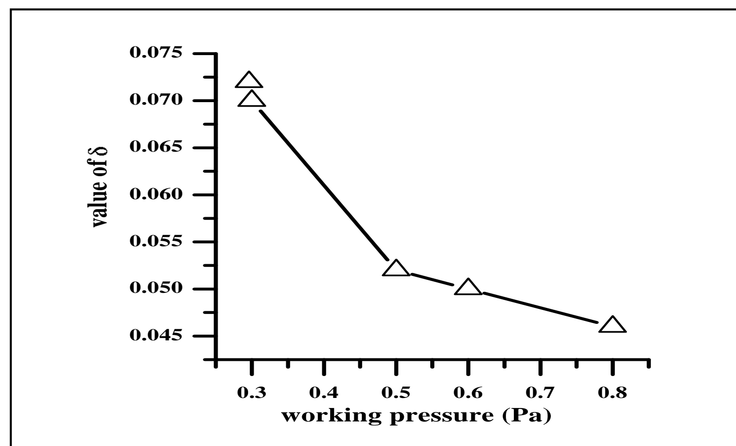

Figure 5.5 Observed intensity ratio of atomic argon line at 476.4nm (Ar II) and at 751.46 nm (Ar I) line as a function of working pressure.

5.4.3. Effect of discharge conditions on the V-I characteristic of magnetron discharge

As already discussed in Chapter 3, the β values obtained from the V-I characteristics of the magnetron are inversely related with the plasma impedance of the discharge and as such, increase with increasing plasma density [2]. Thus for the investigation on the variation of different plasma parameters as a function of working pressure a study of the V-I characteristics is very essential. Now, the DC planar magnetron V-I characteristics are achieved at different working pressures (0.3Pa to 0.8Pa) for both the clean argon plasma and nitrogen added argon plasma and their corresponding β values are determined from the linear fit to V-I plot. It is plotted as a function of working pressure in **Fig. 5.6**. It is seen that for clean argon plasma, increasing working pressure increases the value of β which indicates a gradual increase of the plasma density. When nitrogen is added, it lowers the value of β and with increasing working pressure a gradual decrease of β is noticed. This fact indeed justifies Langmuir probe measurement of electron and ion densities for the nitrogen added argon plasma as a function of increasing working pressure.

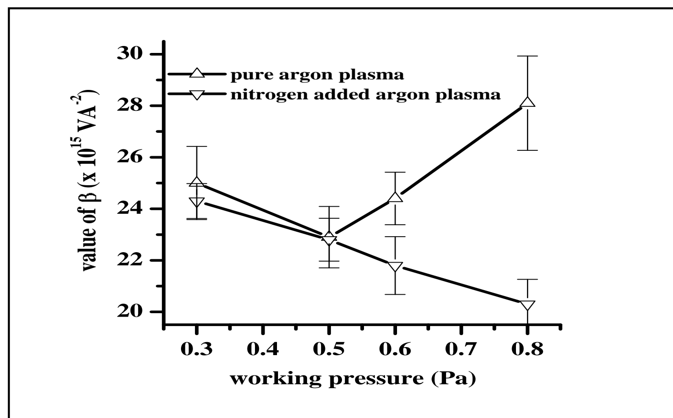

Figure 5.6 Influence of working pressure on the value of β

5.4.4 XRD analysis of the deposited thin films

The X ray diffractions pattern of TiN films of equal thickness (2.5μm) deposited at different working pressures (keeping the other conditions the same) are obtained. TiN thin film deposited by the DC planar magnetron technique is polycrystalline in nature. However, the orientation of TiN thin film can be preferred in certain diffraction direction by suitable choice of the experimental conditions. The preferred orientation of the films is explained in terms of the energy W_{hkl} which is the sum of the surface energy (S_{hkl}) and the strain energy (U_{hkl}). It should be noted that the surface energy is independent of film thickness, whereas the strain energy is a function of the thickness of the film [14]. Thus, there exists a critical thickness above which strain energy is the driving force in determining the most preferred orientation of TiN film as observed by Pelleg et *al* [15]. For TiN films of thickness 2.5μm, the strain energy is responsible in determining its preferred orientation. The (111) plane in TiN crystal is the plane of lowest strain energy and a TiN (111) preferred orientation is the result of relieving strain energy [16]. In this study with increasing working pressure, the number of Ar^+ ions decreases gradually and its results corresponding decrease in the sputtering rate. The modulation of the sputtering rate with working pressure is shown in the **Fig. 5.7**. The decrease of the deposition rate indeed signifies lowering of the degree of ion bombardment onto growing thin film and as such, lowering of strain energy. As the strain energy is the dominating factor in determining the preferential growth of TiN thin film, therefore at lower working pressure a TiN (111) preferred orientation is expected and with increasing working pressure more open diffraction directions such as (200) and (220) should prefer. Thus, the working pressure can be a better optimizing parameter for such controlled thin film growth. The XRD diffraction patterns of the deposited TiN thin films

are shown in the **Fig. 5.8**. The orientation of a polycrystalline film is quantitatively defined by the texture coefficient of the deposited film (T_c) and is defined as [17],

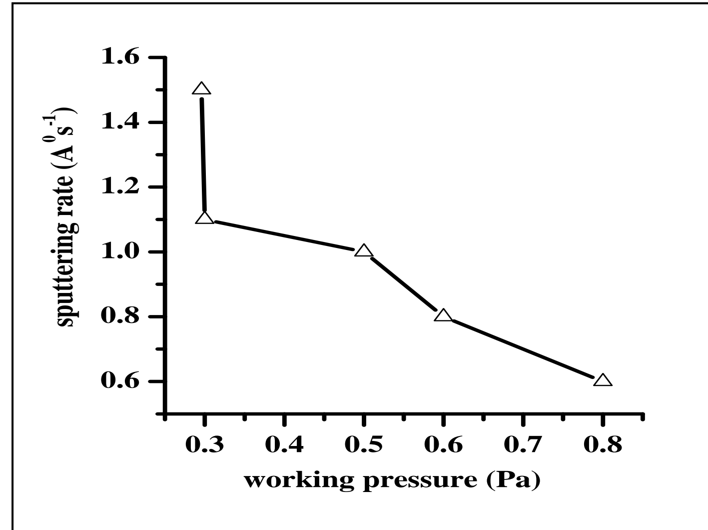

Figure 5.7 Influence of working pressure on the film deposition rate

$$T_c = [nI_{m(hkl)} / I_{0(hkl)}] / \sum (I_{m(hkl)} / I_{0(hkl)})$$

(5.1)where $I_{m(hkl)}$ is the measured intensity of the reflection from a given (hkl) plane and $I_{0(hkl)}$ is the relative intensity of reflection from the same plane as indicated in a standard sample. For random distribution $T_c = 1$ and $T_c > 1$ for a particular diffraction direction signifies the preferred orientation along that direction. Using Eq. (5.1) the value of T_c for different TiN diffraction planes is evaluated and given in the **Table 5.2.**

It is seen from the **Table 5.2** that all coatings possessed a strong (111) preferred orientation. As expected with increasing working pressure, the texture coefficient of TiN (111) diffraction plane decreases and corresponding increase in T_c values for the more open direction like (200) and (220) diffraction peaks is observed. From the discussion in this section it is now clear that for the preferential growth of TiN along (111) direction a lower

deposition pressure (< 0.5 Pa) is desired.

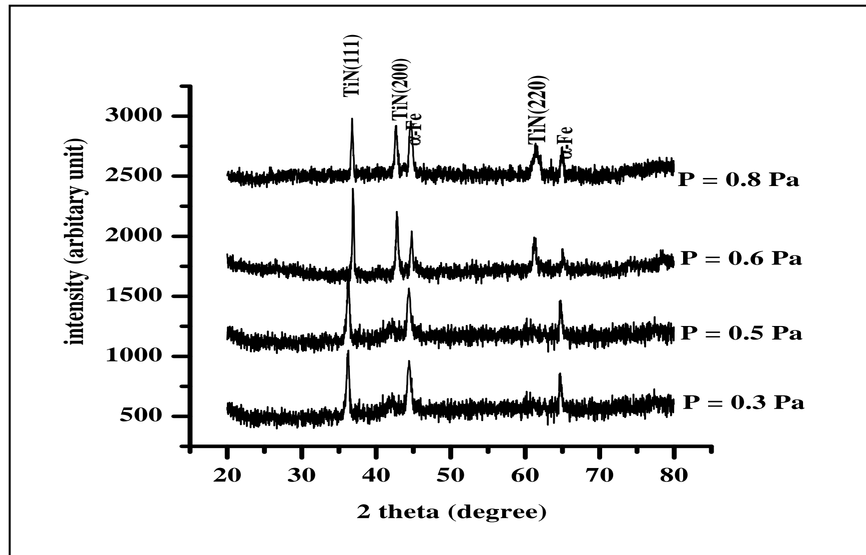

Figure 5.8 Variation of x-ray diffraction patterns of the titanium nitride film deposited on AISI M2 high speed steel substrate as a function of working pressure.

Table 5.2: Value of texture coefficient (T_c) of TiN peaks deposited on bare AISI M2 high speed steel

Nature of the substrate			
	T_c on bare AISI M2 steel		
W_p (Pa)	TiN(111)	TiN(200)	TiN(220)
3×10^{-1}	1.72	0.278	0
5×10^{-1}	1.69	0.30	0
6×10^{-1}	1.37	0.67	0.894
8×10^{-1}	1.14	0.74	1.083

5.5 Conclusion

In this chapter, the effect of working pressure on the properties of Ar/N_2 plasma and as such, the preferred orientation for the deposited TiN film is studied. From the Langmuir

probe study it is found that with increase of working pressure in the Ar/N_2 plasma, the densities of electrons and Ar^+ ions dropped gradually. It is explained on the basis of different rate constant values for loss and production routes of electron and ions, respectively. From the OES study, the degree of ionization of Ar is found to decline as a function of working pressure. From the V-I characteristics of the magnetron discharge, the β values are found to decrease with increasing working pressure and it indicates the decrease of plasma density which is found consistent with the Langmuir probe measurements. The observed plasma parameters of the nitrogen added argon plasma are correlated with the preferred orientation (structural growth) of the titanium nitride (TiN) thin films. Lesser degree of ion bombardment at higher working pressure conditions favors the growth of more open planes of poly crystalline TiN film such as the TiN(200) and TiN(220). Deposition rate measurement at the various working pressure conditions revealed the gradual decline of degree of ion bombardment for such plasma.

5.6 References

[1] I. Safi, Surf. Coat. Technol. **127**, 203 (2000).

[2] D. Depla, G. Buyle, J. Haemers, and R. De Gryse, Surf. Coat. Technol. **200,** 4329 (2006).

[3] M. I. Jones, I. R. McColl, and D. M. Grant, Surf. Coat. Technol. **132,** 143 (2000).

[4] A. Bogaerts, Spectrochim. Acta Part B **64,** 126 (2009).

[5] R. Rejoub, B. G. Lindsay, and R. F. Stebbings, Phys. Rev. A **65,** 042713 (2002).

[6] Y. Itikawa, M. Hayashi, A. Ichimura, K. Onda, K. Sakimoto, and K. Takayanegi, J. Phys. Chem. Ref. Data **15,** 985 (1986).

[7] P. A. Sa and J. Loureiro, J. Phy. D. Appl. Phys. **30,** 2320 (1997).

[8] G. M. Petrov et al., Plasma. Chem. Plasma. Process **20,** 183 (2000).

[9] N. Laidani, B. Bartali, P. Tosi, and M. Anderle, J. Phys. D. Appl. Phys. **37,** 2593 (2004).

[10] J. Henriques, E. Tatarova, V. Guerra, and C. M. Ferreira, J. Appl. Phys. **91,** 5622 (2002).

[11] S. Yugeswaran, K. Suresh, and V. Selvarajan, Plasma Sci. Technol. **12,** 35 (2010).

[12] J. B. Shumaker and C. H. Ponenoe, J. Opt. Soc. Am. **57,** 8 (1967).

[13] W. R. Bennett, P. J. Kindlmann, and G. N. Mercer, Chem. Lasers: Appl. Opt. 2, 34 (1965).

[14] U. C. Oh, J. H. Je, J. Appl. Phys. **74,** 1692 (1993).

[15]J. Pelleg, L. Z. Zevin, S. Lungo, and N. Croitoru, Thin Solid Films **197,** 117 (1991).

[16] D. R. McKenzie, Y. Yin, M. D. McFall, N. H. Hoang, J. Phys. Cond. Mater. **8,** 5883 (1996).

[17] R. L. Mills, J. Sankar, P. Ray, A. Voigot, J. He, B. Dhandapani, J. Mater. Sci. **39,** 3309 (2004).

CHAPTER 6

Role of the substrate on the growth of titanium nitride thin film

In Chapter 5, the effect of working pressure on the preferred orientation of titanium nitride thin film was studied. In this chapter the substrate induced preferred orientation of the titanium nitride thin film deposited onto plasma nitrided substrate is presented.

6.1 Introduction

Titanium nitride (TiN) films have been investigated widely for their very interesting properties such as high hardness, wear and corrosion resistance, low resistivity, etc. The high hardness value makes it applicable to coat cutting tools, thereby increasing the life of the tool [1]. As a decorative coating, the luxurious golden yellow color of TiN finds its application in many industries [2]. In microelectronic, application of the low resistivity and diffusion barrier property of TiN is of great demand [3-4]. TiN coating by magnetron sputtering has developed rapidly over the last decade in such a way that it has become an established process of choice for the deposition of a wide range of industrially important coatings. But due to their unsuitability for the use with many substrate materials such as low alloy steel and titanium alloys and the lack of load-bearing support provided by the substrate, these coatings have certain limitations. To address these problems and to extend the commercial viability of advanced PVD processes, duplex processes have been developed [5]. Physical vapor deposition of TiN on pre-nitrided steel is a good example of a duplex process. Components treated in this way exhibit low wear characteristics of the ceramic coating, combined with the high load-bearing capacity and high fatigue strength characteristics of the nitrided layer. Also, it has been reported by Gredic et *al.* [6] that the

plasma nitriding prior to coating deposition strongly improves the adhesion properties of the hard coating.

It is important to note that most of the TiN coatings are reported to exhibit a preferential crystallographic orientation [7-9] which affects the mechanical behavior of the coatings. The preferential orientation depends on the various process parameters and on the nature of the substrate surface [10]. Dependence of the preferred orientation of TiN on the process parameters like working pressure is discussed in the Chapter 5. This chapter reports thoroughly on the difference in the preferred orientation observed in the DC-sputtered TiN coatings deposited under various conditions onto the bare AISI M2 and plasma-nitrided AISI M2 substrate. The AISI M2 high-speed steel (HSS) (0.86% C, 6.0% W, 5.0% Mo, 4.1% Cr, 1.9% V, and 0.5% Co, in wt.%) is selected as the substrate material because it is mostly used as a cutting tool material.

6.2 Experimental set up and diagnostic procedure

Disc-shaped samples of 20 mm in diameter and 4 mm in thickness, made from the AISI M2 high speed steel are prepared to mirror polish finish by standard metallographic method and cleaned with acetone before processing. Plasma nitriding is done in a different arrangement. The schematic diagram of the planar magnetron sputtering system as well as plasma nitriding system used in this study is described respectively, in the section 2.2 and the section 2.5 of the Chapter 2. Initially, the samples of AISI M2 high speed steel are placed on the sample holder which is negatively biased. The vacuum chamber is evacuated to 1 Pa. The glow discharge is generated using a DC pulsed power supply (1000V, 3A, 0-100KHz) with a gas mixture composition of 80% N_2 -20% H_2. The working pressure of 5 mbar and a voltage of 550 V are maintained during the process. The samples are kept at a temperature

of 500°C with an accuracy of ±10°C, which is read on a temperature indicator using a J-type thermocouple. An external heater is used to heat the negative biased sample holder. After 24 h, AISI M2 samples are cooled with nitrogen gas and latter taken out from the chamber when the samples attained room temperature. It was obtained from the XRD studies of the deposited thin films in the Chapter 5 that lower working pressure (less than 0.5 Pa) favors the preferential growth of TiN (111) on bare AISI M2 high speed steel. Keeping this fact into account, the TiN thin film is deposited onto bare as well as the plasma nitrided high speed steel below 0.5 Pa. The working pressures at 3×10^{-1} Pa and input power of 300 W are fixed during the deposition of the samples. During the deposition the values of nitrogen partial pressure (P_{N_2}) are varied from 1×10^{-2} to 8×10^{-2} Pa. Equal duration of TiN deposition at the above mentioned values of nitrogen partial pressures results thin film of thickness 2.90μm to 1.97μm. To clean the substrate surfaces prior to the deposition and improve film's adhesion, the bare and plasma-nitrided substrates are pre-treated by Ar plasma in a sputtering chamber for 10 min with a bipolar power supply bias of −300V. Phase composition of all the untreated and treated samples are studied by X-ray diffraction (XRD) using a XRD3000PTS diffractometer (GE Inspection Technologies, Ahrensburg, Germany) with the CuK_α radiation (λ = 1.5406 Å) in the Bragg-Brentano configuration operated at 40 keV and 50 mA. XRD patterns are recorded with step durations of 4 s at each step in the angular range of 30° to 90°. In order to find out the substrate induced TiN growth, we need to compare the texture coefficients of the various TiN diffraction peaks deposited on the bare and pre-plasma nitrided substrate. Information regarding the preferred orientation of the different planes is obtained by measuring the

intensities of the diffraction peaks and as such, the texture coefficients corresponding to the various planes. The thickness of the deposited films is determined by properly calibrated quartz crystal thickness monitor model no. DTM-101 provided by Hind HiVac, Bangalore, India.

6.3 Results and discussions

6.3.1 Langmuir probe study of the magnetron plasma

The magnetron discharge plasma at the above mentioned values of working pressure is scanned by the cylindrical Langmuir probe to obtain the value of ion and the electron density. The important production and loss mechanism in the nitrogen added argon plasma is already described in the section 5.3 of the Chapter 5. When nitrogen is added at a fixed working pressure, the densities of the nitrogen related ions such as N_2^+, N_3^+, and N_4^+ should increase and Ar^+ ions should decrease for obvious reasons. However, due to the higher rate coefficients of the recombination reactions of the nitrogen related ions (Reactions 3, 4 and 9 of **Table 5.1**, section 5.3 of Chapter 5) the loss mechanisms of electrons become dominant over its production mechanisms. As a result a gradual decrease of density of electron with increasing nitrogen partial pressure is also observed. Following the procedure of the mean ion mass as explained in the Chapter 2, the density of Ar^+ ions in the discharge is calculated and as mentioned already, it is found to decrease with addition of nitrogen in the argon discharge. As the sputtering yield of titanium target to Ar^+ ions is greater than the other positive ions present in such discharge, therefore higher value of deposition rate is achieved at lower nitrogen partial pressure. Accordingly, the TiN films deposited with nitrogen partial at 1×10^{-2} Pa have the maximum thickness. The modulation of electron and

Ar^+ ion density and TiN deposition rates as a function of nitrogen partial pressure are given in **Fig. 6.1**.

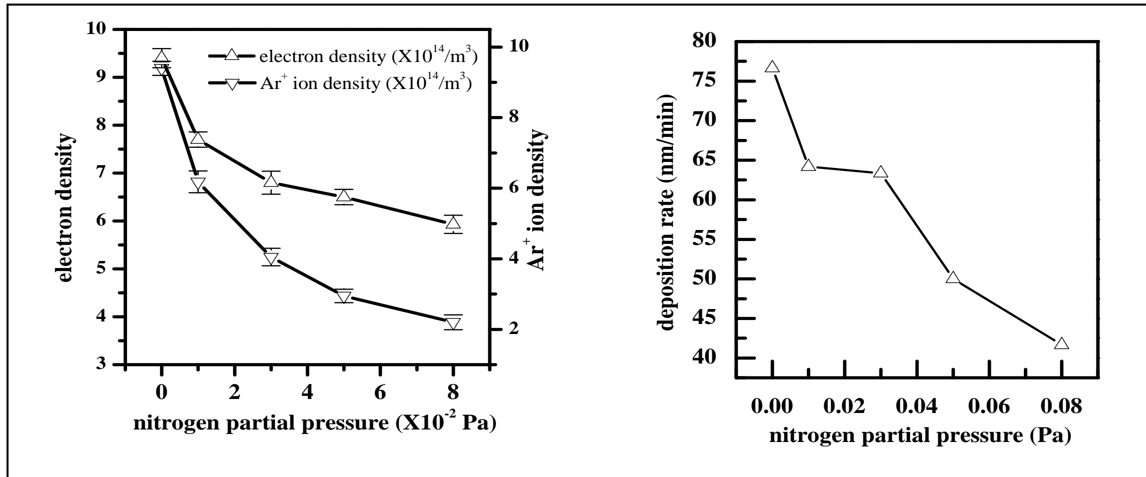

Figure 6.1 Effect of nitrogen partial pressure on (a) the variation of electron and Ar^+ ion density in nitrogen added argon plasma (b) the film deposition rate.

6.3.2 XRD studies of the plasma nitrided AISI M2 high speed steel

The X-ray diffraction patterns with CuK_{α} radiation is used to identify the formed phases in the plasma nitrided samples.

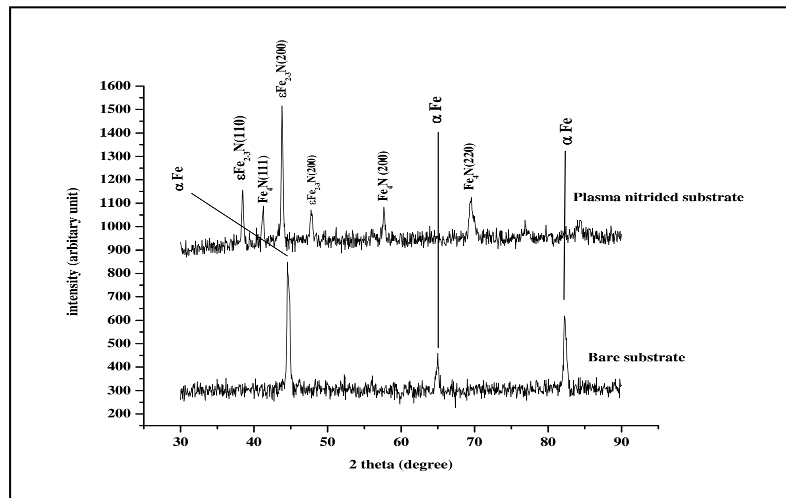

Figure 6.2 X. R. D pattern of bare and plasma nitrided AISI M2 high speed steel

The formation of the nitrided layer of different structures can be controlled by N_2/H_2 gas composition [12]. **Fig. 6.2** shows the diffraction patterns of the bare and plasma-nitrided sample, respectively. These figures reveal that all intense peaks on the bare substrate are assigned to α-Fe-phase. On the plasma nitrided substrate the most intense peaks are assigned to ε- $Fe_{2\text{-}3}N$ and γ′-Fe_4N phases while the peaks of α-phase are disappeared. It is worth mentioning that the hexagonal closed packed (hcp) ε-nitride exhibits a higher hardness than the face centered cubic (fcc) - γ′-nitride [13].

6.3.3 XRD studies of the deposited titanium nitride thin films

The phase composition and texture in polycrystalline TiN thin film deposited onto the bare and plasma-nitrided AISI M2 high-speed steel are analyzed by X-ray diffractometer. **Fig. 6.3** shows X-ray spectra for TiN coating on (a) bare AISI M2 sample and (b) plasma-nitrided AISI M2 substrate at different values of nitrogen partial pressures. The coatings deposited onto the above mentioned substrates show the presence of (111), (200), and (220) TiN diffraction peaks and α Fe(110) peak on the bare sample. All iron nitride phases like ε $Fe_{2\text{-}3}N$ and γ′ Fe_4N are observed even after deposition of the TiN coating onto the plasma-nitrided substrate. It is clear from the **Fig. 6.3(a)-(b)** that the orientation of TiN is clearly influenced by deposition and substrate conditions. On the bare samples, higher intensity of the TiN (111) peak is observed compared to the TiN (200) and TiN (220) peaks. However at higher nitrogen partial pressure an increased intensity of TiN (220) peak is noticed. On the plasma-nitrided samples, the relative intensity of diffraction peak is different than the bare samples. Here, the intensity of the TiN (200) peak is dominant over the other TiN diffraction peaks. From the observed intensity of the diffraction planes, it is possible to calculate the texture coefficients (T_c) of a particular diffraction plane that represents the

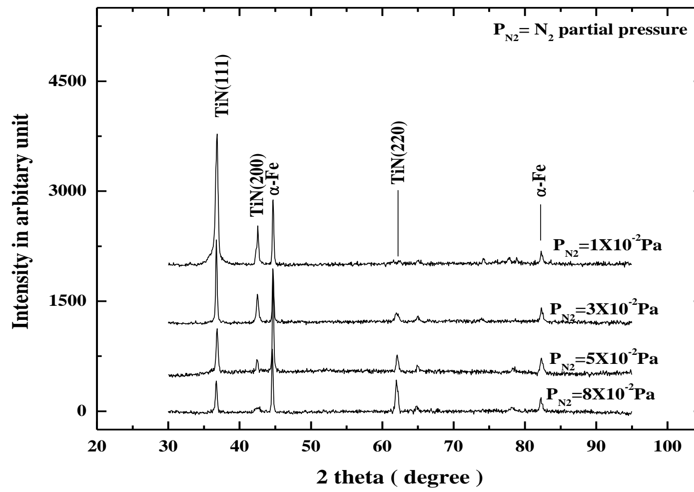

Figure 6.3(a) X.R.D patterns of TiN deposited on the bare AISI M2 substrate.

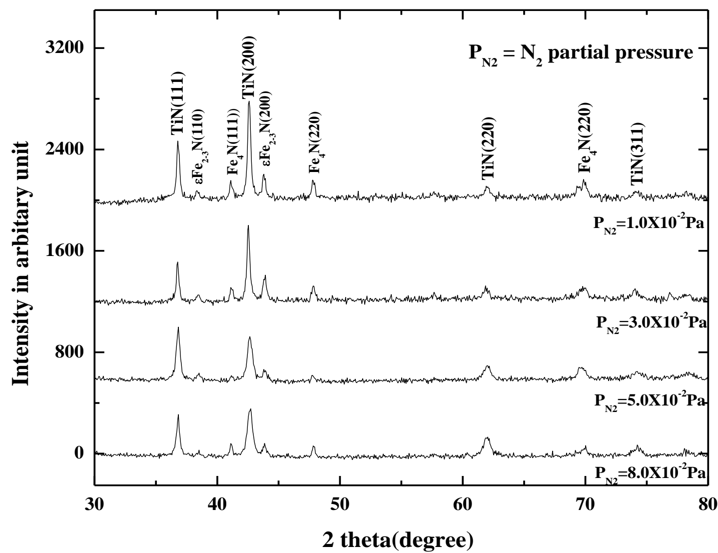

Figure 6.3(b) X.R.D patterns of TiN deposited on the plasma nitrided AISI M2 substrate.

degree of preferred orientation. On bare substrate a TiN(111) preferred orientation is observed. The minimization of the strain energy [14, 15] as a responsible factor for such preferred orientation of the TiN films on the bare AISI M2 substrate was explained in

details in the Chapter 5. It is worthwhile to mention again that for the deposited TiN thin films with such high value of thickness (greater than 1.90 μm), (111) preferred orientation is the result of relieving strain energy [16]. It is also interesting to mention that decrease of the thin film thickness at the higher value of nitrogen partial pressure promotes more open diffraction planes like the TiN(220) on the bare substrate. However, the texture growth of TiN films deposited onto the plasma-nitrided high-speed steel is different. In this case the (200) preferred orientation is observed at the various deposition conditions. The value of the texture coefficient of the different TiN peaks deposited onto the bare and plasma nitrided AISI M2 high sped steel is given in the **Table 6.1**.

Table 6.1: Value of texture coefficient (T_c) of TiN peaks deposited on bare and plasma nitrided high speed steel

Nature of the substrate							
	T_c on bare AISI M2 steel			T_c on pre-plasma nitrided AISI M2 steel			
W_p (Pa)	TiN(111)	TiN(200)	TiN(220)	TiN(111)	TiN(200)	TiN(220)	TiN(311)
1×10^{-2}	**1.79**	0.20	0	1.30	**1.68**	0.38	0.62
3×10^{-2}	**1.44**	0.72	0.43	1.19	**1.64**	0.50	0.65
5×10^{-2}	**1.31**	0.57	1.12	**1.16**	1.02	0.73	0.63
8×10^{-2}	1.18	0.13	**1.74**	1.08	**1.14**	0.91	0.80

Note that the bold indicates the preferred TiN peaks deposited onto bare and pre-plasma nitrided substrate.

It is clear from the table that minimization of strain energy cannot explain the texture of TiN films on the plasma-nitrided substrate and as such, we have to look for the substrate-induced texture growth in this case.

6.3.4 Effect of substrate on the texture growth of the TiN films

Very few investigation reports the contribution of substrate surface structure [17-18] on the preferential growth of TiN thin film. It can be seen from the XRD analysis that near-surface crystallography affects the orientation of TiN film subsequently grown on them. The XRD analysis of the plasma-nitrided samples shows the presence of $\gamma' Fe_4N$ and $\varepsilon Fe_{2\text{-}3}N$ diffraction peak leading to the formation of compound layer on the surface of the substrate. The inter-atomic spacing of $\gamma' Fe_4N$ planes of the plasma-nitrided substrate is found to be very similar to the TiN diffraction planes. Earlier studies [3, 18-21] of the TiN growth on the plasma-nitrided substrate have reported the preferred orientation of TiN (220) plane but the compositions of the hydrogen-nitrogen gases for plasma nitriding in those studies are different from the one used in this investigation. Finally in order to explain the preferential growth of the TiN (200) peak on the plasma-nitrided substrate in our study, we have compared the inter-planar distances (d) of $\gamma' Fe_4N$ planes of the plasma-nitrided surface with the TiN diffraction planes on bare substrate and are listed in the **Table 6.2**. Both TiN (200) and $\gamma' Fe_4N$ (111) planes are closed pack. Also, from **Table 6.2**, it is clear that the inter-atomic spacing between TiN (200) planes and $\gamma' Fe_4N$ (111) planes are very similar, i.e., an atomic mismatch of only 0.23%. Thus, interfacial strain at the substrate (111)/coating (200) interface would be very low [22]. This factor may be responsible for higher degree of preferred orientation of TiN (200) plane on plasma-nitrided substrate.

Table 6.2 Inter-atomic spacing between TiN planes and $\gamma'Fe_4N$ planes

Phases	γ' Fe_4N d(nm)	TiN d(nm)
(111)	***0.2191***	0.2440
(200)	0.1901	***0.2141***
(220)	0.1351	0.1487

Note the similarity of calculated values (italics) for inter-planar distances of $\gamma'Fe_4N$ (111) plane and TiN (200) plane.

Since different iron nitride phases are present on plasma-nitrided surface, additional investigations of the coating/substrate interface using HR SEM and TEM are necessary.

6.4 Conclusion

The chapter reports the growth of TiN texture on the bare and plasma-nitrided AISI M2 high-speed steel. While there are many reports available in the literature regarding the growth of TiN as a function of the deposition parameters on Si and bare substrate, very few investigations is available regarding the effect of substrate such as the plasma nitrided surface on the growth of TiN texture. In this study, the substrate-induced texture growth of TiN is clearly visible on the plasma-nitrided high-speed steel substrate. While the TiN (111) plane preferentially grows on the bare AISI M2 substrate, the TiN (200) orientation is preferred on the plasma-nitrided substrate. The matching of the inter-planar distances of the TiN (200) plane with $\gamma'Fe_4N$ plane of the plasma-nitrided substrate is believed to be a factor responsible for this preferred orientation.

References

[1] S. Veprek, J. Vac. Sci. Technol. A **17,** 2401 (1999).

[2] E. Valkonen, C. G. Ribbing, and J. E. Sundgren, Appl. Opt. **25,** 3624 (1986).

[3] P. Engel, G. Schang, and G. K. Wolf, Surf. Coat. Technol. **98,** 1002 (1998).

[4]Y. Chiba, T. Omura, and H. Ichimura, J. Mater. Res. **8,** 1109 (1993).

[5]P. J. Kelly, and R. D. Arnell, Vacuum **56,** 159 (2000).

[6]T. Gardic, M. Zlatanonic, N. Popovic, and Z. Bogdanov Thin Solid Film, **228** 261 (1993).

[7] F. Fichter, H. Kupfer, H. Giegengack, G. Schaarschmidt, F. Scholze, F. Elstner, G. Hecht, Surf. Coat. Technol. **54,** 338 (1992).

[8]M. Kobayashi, Y. Doi, Thin Solid Film **54,** 67 (1992).

[9] J. E. Sundgren, Thin Solid Film **128,** 21 (1985).

[10]S. Guruvenket, G. Mohan Rao, J. Vac. Sci. Technol. A **20,** 678 (2000).

[11] R. L. Mills, J. Sankar, P. Ray, A. Voigot, J. He, B. Dhandapani, J. Mater. Sci. **39,** 3309 (2004).

[12] J. Walkowicz, P. Supiot, J. Smolik, M. Grushin, Surf. Coat. Technol.**180-181**, 1187 (1998).

[13] H. Ferkel, Y. Estrin, C. Blawert, R.Z. Valiev, Surf. Coat. Technol. **173–174**, 1164 (2003).

[14] J. Pelleg, L. Z. Zevin, S. Lungo, and N. Croitoru, Thin Solid Films **197,** 117 (1991).

[15]U. C. Oh, and J. H. Je, J. Appl. Phys. **74,** 1692 (1993).

[16] D. R. McKenzie, Y. Yin, M. D. McFall, and N. H. Hoang, J. Phys. Cond. Mater. **8,** 5883 (1996).

[17] H. H. Yang, J. H. Je, and K. B. Lee, J. Mater. Sci. Lett. **14,** 1635 (1995).

[18] C. Quaeyhaegens, L. M. Stals, M. VanStappen, and L. De Schepper, Thin Solid Films **197,** 37 (1991).

[19] H. H. Huang, J. L. He, and M. H. Hon, Surf. Coat. Technol. **64,** 41 (1994).

[20] M. Zlatanovic, T. Gredic, N. Popovic, Z. Bogdanov, Vacuum **44,** 83 (1993).

[21] M. I. Jones, I. R. McColl, and D. M. Grant, Surf. Coat. Technol.**132**, 143 (2000).

[22] W. Ensinger, Surf. Coat. Technol. **65**, 90 (1994).

CHAPTER 7

Theoretical investigation of the ion acoustic soliton in hydrogen added argon plasma

7.1 Introduction

Ion acoustic soliton in plasma is a nonlinear wave results due to the delicate balance between the non-linearity and dispersion present in the plasma medium [1-3]. From a detailed numerical study Zabusky and Kruskal [4] found that they could collide with each other and yet preserve their shapes and speeds after the collision. This particle-like nature led Zabusky and Kruskal to name such waves 'solitons'. The first success of the soliton concept was the explanation of the recurrence in the Fermi-Pasta-Ulam system. It is worthwhile to mention that, Ikezi et al [5] first observed the compressional wave excited by the applied potential which transformed into soliton under certain plasma conditions. Experimental existence of the ion acoustic solitons in various processing plasmas is available in literature [6-7]. The presence of ion acoustic solitary wave in the oxygen-added argon magnetron discharge was reported in the Chapter 4 and the phase velocities of the solitary waves were effectively used to measure the value of the relative negative oxygen ion concentration. However, as done in the Chapter 4 when we try to excite the ion acoustic solitary wave in the hydrogen added argon plasma by increasing the amplitude of the applied sinusoidal signal keeping the other discharge conditions same, it seems as if the lighter hydrogen-like ions inhibit the formation of the soliton. **Fig. 7.1** shows the detected signal by a plane Langmuir probe fixed at a distance of 6 cm from the centre of the exciting grid in the hydrogen and oxygen added argon plasma for an exciting sinusoidal voltage (V_{ex}) of 6.0 V. It was reported by Tran et *al.* [8] that addition of small amount of light ion

impurity in the argon DC glow discharge plasma is sufficient enough to prevent the formation of solitons. Since, the various plasma processing techniques like the DC magnetron sputtering, etching etc, use argon glow discharge, it is reasonable to believe that the formation of soliton is inhibited upon the addition of light ion impurity such as hydrogen like ions. A proper theoretical investigation of this effect is very essential for the prediction of solitons existence in such plasma.

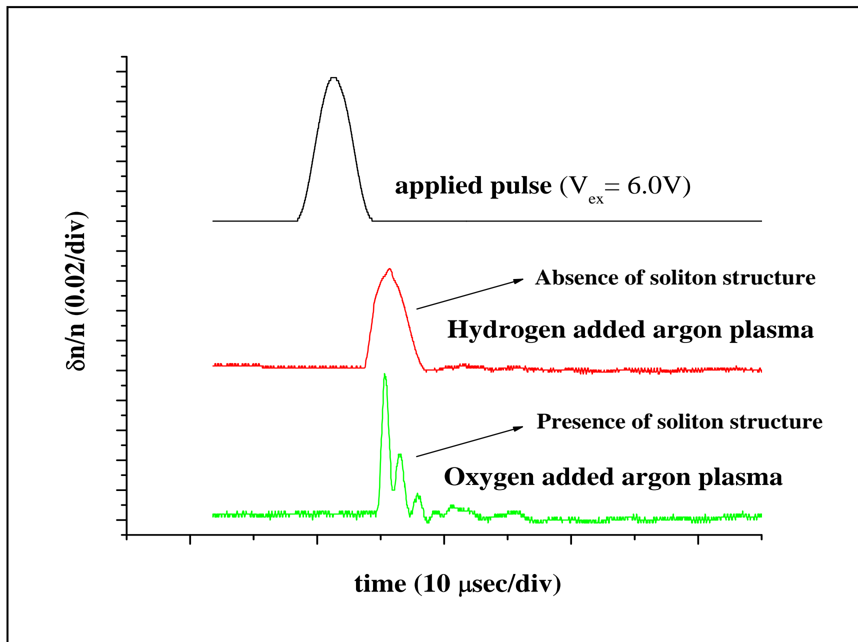

Figure 7.1 Observed signals at position of the planar probe at X = 6 cm from the grid for an initial pulse (V_{ex} = 6.0 V) at oxygen and hydrogen partial pressure of 6×10^{-3} Pa in the background of argon plasma. The traces are not to scale. Clearly the figure indicates the absence of the soliton peaks in hydrogen added argon plasma.

With this idea in mind, the bulk region of the DC planar magnetron discharge plasma is modeled as a fluid consisting of ions and electrons. Theoretical investigations of ion acoustic solitary waves in cold ion plasma have been investigated extensively by many

authors [9-12]**.** Since both the atmospheric plasmas as well as laboratory plasma have finite electron and ion temperature, it is essential to investigate the existence of these waves under such conditions. The existence of solitary waves has been investigated as a function of H_2 addition and finite ion temperature in the argon plasma using Sagdeev pseudo potential technique. Beside this, the investigation of the effect of hydrogen addition on the Mach number and amplitude of ion acoustic soliton in the Ar/H_2 plasma is also explained. The chapter is organized in following sections. In the next section (7.2) the theoretical formulation of the soliton is achieved following Sagdeev's pseudo-potential approach. The advantage of the Sagdeev pseudo-potential is its ability to describe arbitrary amplitude wave. Effects of the parametric variation on the formation and properties of the soliton have been discussed in the section 7.3. The findings of the chapter are summarized in the section 7.4.

7.2 Theoretical formulation

When H_2 is added to argon, besides Ar atoms (in ground state and excited to meta-stable states (Ar_m^*) at energy 11.2 ev), Ar^+ ions and electrons, several hydrogen species including H^+, H_2^+, H_3^+ ions; ArH^+ ions, the ground state H atom, ground state H_2 molecule and various electronically excited states of H_2 molecules are also possible [13]. All species of an Ar/H_2 plasma mentioned above undergo different chemical reactions with different the rate constants and relative cross sections. With increasing hydrogen addition a drop in the electron and Ar^+ ion densities was already reported in Chapter 3. On the other hand, the densities of hydrogen related ions, i.e., H^+, H_2^+, H_3^+ and ArH^+ are expected to increase with H_2 addition for obvious reasons. For the calculation of mean ion mass in the hydrogen containing argon plasma, the procedure of dividing the ions present in such plasma into two

mass groups was explained in the Chapter 2. In the heavy ion group, Ar^+ has higher density than ArH^+ and in the lighter ion group; the dominance of the number density of H_3^+ ions compared to the other hydrogen like ions is already reported in the literature [14-15]. This allows us to select only two types of ions with significant density which is the representative of each group respectively. As such the model equations for plasma consist of a two fluid plasma model for ions and the Maxwellian distribution for electrons. The linear dispersion relation for ion acoustic wave (IAW) for such three component cold ion plasma can be written as [16]

$$\frac{\omega}{k} = c_s \sqrt{1 + \frac{n_1}{n_e}(\mu - 1)} \times \frac{1}{\sqrt{1 + k^2 \lambda^2_{De}}} \tag{7.1}$$

Here, ω is frequency of the wave, k is the wave number, λ_{De} is the electron Debye length, μ is the mass ratio $(\mu = \frac{m_2}{m_1} > 1)$ where m_1 and m_2 are the mass of heavy and light ion, n_1 is the light ion density, n_e is the electron density and $c_s (= \sqrt{\frac{k_B T_e}{m_2}})$ is the ion acoustic velocity for heavy ion, T_e is electron temperature. In the long wavelength range for $k^2 \lambda^2_{De} << 1$ this equation reduces to

$$\frac{\omega}{k} = c_s \sqrt{1 + \frac{n_1}{n_e}(\mu - 1)} \tag{7.2}$$

Eq. (7.2) implies the fact that the phase velocity $(v_p = \frac{\omega}{k})$ of the IAW in such plasma is always greater than c_s and increases with rise in the lighter ion density. The physical reason of the increase in phase velocity is attributed to the fact of electron density depletion

in the back ground plasma with addition of lighter ion so that electron Debye length becomes larger. Instead of cold ions if finite ion temperature is considered, the continuity and momentum equation for light ($n_1^{'}$) and heavy ($n_2^{'}$) ion are given by,

$$\partial_t n_1^{'} + \partial_x (n_1^{'} v_{x1}) = 0 \tag{7.3}$$

$$m_1 n_1^{'} (\partial_x v_{x1} + v_{x1} \partial_x v_{x1}) = -\partial_x p_{x1}^{'} - e n_1^{'} \frac{\partial \phi}{\partial x} \tag{7.4}$$

$$\partial_t n_2^{'} + \partial_x (n_2^{'} v_{x2}) = 0 \tag{7.5}$$

$$m_1 n_2^{'} (\partial_x v_{x2} + v_{x2} \partial_x v_{x2}) = -\partial_x p_{x2}^{'} - e n_2^{'} \frac{\partial \phi}{\partial x} \tag{7.6}$$

In the next step, we will linearize the Eq. (7.3) to Eq. (7.6). If the equilibrium properties are donated with an index 0 and the perturbed quantities an index 1 and assuming

$$\left.\begin{aligned} n_1^{'} &= n_0 + n_1 \\ v_{x1} &= v_1 \\ \phi &= \phi_1 \end{aligned}\right\} \tag{7.7}$$

then, the first order equations for the lighter ion becomes

$$\partial_t n_1 + n_{01} \partial_x v_1 = 0 \tag{7.8}$$

$$m_1 n_{01} \partial_t v_1 = -e n_{01} \frac{\partial \phi_1}{\partial x} - \partial_x p_1 \tag{7.9}$$

For the warm plasma we have to include the linearized pressure equation,

$$\partial_t p_1 = -\gamma p_{01} \partial_x v_1 \tag{7.10}$$

The first order equations for the heavy ion are,

$$\partial_t n_2 + n_{02} \partial_x v_2 = 0 \tag{7.11}$$

$$m_2 n_{02}\partial_t v_2 = -en_{02}\frac{\partial \phi_1}{\partial x} - \partial_x p_2 \tag{7.12}$$

$$\partial_t p_2 = -\gamma p_{02}\partial_x v_2 \tag{7.13}$$

For the dispersion relation, if we assume a solution of the form $\eta = \eta^{'}\exp(-i\omega t + ikx)$ with $\eta = n_1, p_1, \phi_1$ Eq. (7.8), Eq. (7.09) and Eq. (7.10) gives,

$$-i\omega n_1 + ikn_{10}v_1 = 0 \Rightarrow \frac{n_1}{n_{01}} = \frac{k}{\omega}v_1 \tag{7.14}$$

$$-i\omega v_1 = -\frac{e}{m_1}(ik\phi_1) + \frac{1}{m_1 n_{01}}(ikp_1) \tag{7.15}$$

$$p_1 = -\frac{k}{\omega}\gamma p_{01}v_1 \Rightarrow p_1 = -\frac{k}{\omega}n_{01}k_B T_1 v_1 \tag{7.16}$$

Here T_1 is the temperature of the light ion. Substituting the value of p_1 from Eq. (7.16) in Eq. (7.15) we obtain,

$$v_1(w - \frac{k^2 k_B}{m_1\omega}T_1) = \frac{ek\phi_1}{m_1} \Rightarrow \frac{n_1}{n_{01}}(m_1\omega^2 - T_1 k^2 k_B) = e\phi_1 k^2$$

Thus, $$n_1 = \frac{n_{01}e\phi_1 k^2}{m_1\omega^2 - k^2 k_B T_1} \tag{7.17}$$

Similar treatments to Eq. (7.11) to Eq. (7.13) give,

$$n_2 = \frac{n_{02}e\phi_1 k^2}{m_2\omega^2 - k^2 k_B T_2} \tag{7.18}$$

with T_2 is the temperature of the heavy ion. With Maxwellian distribution for electrons, the Poisons equation,

$$\frac{\partial^2 \phi}{\partial x^2} = 4\pi e(n_e - n_1 - n_2) \tag{7.19}$$

in such plasma becomes,

$$-k^2\phi_1 = 4\pi e[n_{oe}\frac{e\phi_1}{k_B T_e} - n_1 - n_2] \Rightarrow -k^2\phi_1 = 4\pi e^2\frac{n_{0e}}{k_B T_e}[\phi_1 - \frac{k_B T_e}{n_{oe}}n_1 - \frac{k_B T_e}{n_{oe}e}n_2] \tag{7.20}$$

Here, n_{oe} is the equilibrium electron density. Eq. (7.20) finally gives,

$$-k^2 = 4\pi e^2\frac{n_{oe}}{k_B T_e}[1 - \frac{n_{01}}{n_{0e}}\frac{k^2 k_B T_e}{m_1\omega^2 - k^2 k_B T_1} - \frac{n_{02}}{n_{oe}}\frac{k^2 k_B T_e}{m_2\omega^2 - k^2 k_B T_2}] \tag{7.21}$$

Taking $\frac{n_{01}}{n_{oe}} = \alpha$ and $\lambda_{De}^2 = \frac{k_B T_e}{4\pi e^2 n_{eo}}$ where α is the concentration of light ions to electron density and λ_{De} is Debye length, Eq. (7.21) becomes

$$1 + k^2\lambda_{De}^2 = \frac{\alpha k^2 k_B T_e}{m_1\omega^2 - k_B T_1 k^2} + \frac{(1-\alpha)k^2 k_B T_e}{m_2\omega^2 - k_B T_2 k^2} \tag{7.22}$$

Eq. (7.22) is rearranged as,

$$1 + k^2\lambda_{De}^2 = \frac{\alpha}{\frac{m_1}{m_2}\frac{\omega^2}{k^2}\frac{m_2}{k_B T_e} - \frac{T_1}{T_e}} + \frac{1-\alpha}{\frac{m_2}{k_B T_e}\frac{\omega^2}{k^2} - \frac{T_2}{T_e}} \tag{7.23}$$

Writing $\frac{m_2}{m_1} = \mu$, $\frac{k_B T_e}{m_2} = c_s^2$, $\frac{T_1}{T_e} = \sigma_1$ and $\frac{T_2}{T_e} = \sigma_2$ Eq. (7.23) leads to,

$$1 + k^2\lambda_{De}^2 = \frac{\alpha}{\frac{1}{\mu}\frac{\omega^2}{k^2}\frac{1}{c_s^2} - \sigma_1} + \frac{1-\alpha}{\frac{\omega^2}{k^2}\frac{1}{c_s^2} - \sigma_2} \tag{7.24}$$

Here, σ_i with $i = 1,2$ for light and heavy ion respectively are the ratios of ion to electron temperature. Donating $Z = \frac{1}{1 + k^2\lambda_{De}^2}$ Eq. (7.24) leads to,

$$(\frac{\omega^2}{k^2} - \mu\sigma_1 c_s^2)(\frac{\omega^2}{k^2} - \sigma_2 c_s^2) = Z[\mu\alpha c_s^2(\frac{\omega^2}{k^2} - \sigma_s c_s^2) + (1-\alpha)(\frac{\omega^2}{k^2} - \mu\sigma_1 c_s^2)c_s^2] \tag{7.25}$$

$$\frac{\omega^4}{k^4}-\frac{\omega^2}{k^2}c_s^2[\sigma_2+\mu\sigma_1+Z\alpha\mu+(1-\alpha)Z]+c_s^4[\mu\sigma_1\sigma_2+(1-\alpha)Z\mu\sigma_1+Z\alpha\mu\sigma_2]=0 \tag{7.26}$$

Writing,

$$A=[\sigma_2+\mu\sigma_1+Z\alpha\mu+(1-\alpha)Z]$$

$$B=[\mu\sigma_1\sigma_2+(1-\alpha)Z\mu\sigma_1+Z\alpha\mu\sigma_2]$$

and solving Eq. (7.26) we get,

$$\omega^2=\frac{k^2c_s^2A\pm c_s^2k^2\sqrt{A^2-4B}}{2} \tag{7.27}$$

The normalized plasma fluid equations with finite ion temperature (warm ions) as follows,

$$\frac{\partial n_1}{\partial t}+\frac{\partial}{\partial x}(n_1v_1)=0 \tag{7.28}$$

$$\frac{\partial n_2}{\partial t}+\frac{\partial}{\partial x}(n_2v_2)=0 \tag{7.29}$$

$$(\frac{\partial v_1}{\partial t}+v_1\frac{\partial v_1}{\partial x})=-\mu\frac{\partial\phi}{\partial x}-\mu\frac{\sigma_1}{n_1}\frac{\partial P_1}{\partial x} \tag{7.30}$$

$$(\frac{\partial v_2}{\partial t}+v_2\frac{\partial v_2}{\partial x})=-\frac{\partial\phi}{\partial x}-\frac{\sigma_2}{n_2}\frac{\partial P_2}{\partial x} \tag{7.31}$$

$$n_e=e^{\phi} \tag{7.32}$$

In these equations distances are normalized to $\lambda_{De}(=T_e/4\pi e^2n_{e0})^{1/2})$, time to inverse of ion plasma frequency $\omega_{p_i}{}^{-1}(\omega_{p_i}{}^2=\frac{4\pi e^2n_{e0}}{m_2})$, velocities to ion sound velocity (c_s), density to individual equilibrium densities and electrostatic potential (ϕ) to T_e/e, pressure to ion equilibrium pressure ($p_0=n_oT_i$) respectively.

The fluid equations are coupled through Poison's equation as,

$$\frac{\partial^2 \phi}{\partial x^2} = (n_e - \alpha n_1 - (1-\alpha) n_2) \tag{7.33}$$

To obtain a solitary wave solution, we assume that all the variables in the evolution equations depend on a single variable $\xi = x - Mt$, (where M is the Mach number, i.e. the propagation velocity normalized by the sound speed). Making the transformation, $\xi = x - Mt, \quad \tau = t$ we obtained from Eq. (7.28) to Eq. (7.31)

$$-M \frac{\partial n_1}{\partial \xi} + \frac{\partial}{\partial \xi}(n_1 v_1) = 0 \tag{7.34}$$

$$-M \frac{\partial n_2}{\partial \xi} + \frac{\partial}{\partial \xi}(n_2 v_2) = 0 \tag{7.35}$$

$$\left[-M \frac{\partial v_1}{\partial \xi} + v_1 \frac{\partial v_1}{\partial \xi} \right] = -\mu \frac{\partial \phi}{\partial \xi} - 3\mu\sigma_1 n_1 \frac{\partial n_1}{\partial x} \tag{7.36}$$

$$\left[-M \frac{\partial v_2}{\partial \xi} + v_2 \frac{\partial v_2}{\partial \xi} \right] = -\frac{\partial \phi}{\partial \xi} - 3\sigma_2 n_2 \frac{\partial n_2}{\partial x} \tag{7.37}$$

with the boundary conditions that at $\xi = \pm\infty, n_i = 1, v_i = 0, \phi = 0$. Upon integrating and by putting the above boundary conditions in Eq. (7.34) to Eq. (7.37) give,

$$n_1 = \frac{M}{M - v_1} \tag{7.38}$$

$$n_2 = \frac{M}{M - v_2} \tag{7.39}$$

which finally gives,

$$3\mu\sigma_1 n_1^{\ 4} - (M^2 - 2\mu\phi + 3\mu\sigma_1) n_1^{\ 2} - M^2 = 0 \tag{7.40}$$

$$3\sigma_2 n_2^{\ 4} - (M^2 - 2\phi + 3\sigma_2) n_2^{\ 2} - M^2 = 0 \tag{7.41}$$

These equations are quadratic in nature and can be solved as,

$$n_1^{\ 2} = \frac{(M^2 - 2\mu\phi + 3\mu\sigma_1) \pm \sqrt{(M^2 - 2\mu\phi + 3\mu\sigma_1)^2 - 12\mu\sigma_1 M^2}}{6\mu\sigma_1} \tag{7.42}$$

$$n_2^{\ 2} = \frac{(M^2 - 2\phi + 3\sigma_2) \pm \sqrt{(M^2 - 2\phi + 3\sigma_2)^2 - 12\sigma_2 M^2}}{6\sigma_2} \tag{7.43}$$

To get an easily expressible form of n_1 and n_2 following Ghosh et *al.* [17] we have,

$$n_1(\phi) = \frac{1}{2\sqrt{3\mu\sigma_1}}[\{(M + \sqrt{3\mu\sigma_1})^2 - 2\mu\phi\}^{1/2} - \{(M - \sqrt{3\mu\sigma_1})^2 - 2\mu\sigma_1\}^{1/2}] \tag{7.44}$$

$$n_2(\phi) = \frac{1}{2\sqrt{3\sigma_2}}[\{(M + \sqrt{3\sigma_2})^2 - 2\phi\}^{1/2} - \{(M - \sqrt{3\sigma_2})^2 - 2\sigma_2\}^{1/2}] \tag{7.45}$$

Using the values of n_1 and n_2 from Eq. (7.44) and Eq. (7.45) in Eq. (7.33) for small amplitude limit i.e., $\phi << 1$, one obtains

$$\frac{\partial^2\phi}{\partial\xi^2} = 1 + \phi + \frac{\phi^2}{2} - \alpha\left(1 + \frac{\phi}{M^2 - 3\mu\sigma_1} + \frac{3}{2}\frac{\mu^2(M^2 + \mu\sigma_1)}{(M^2 - 3\mu\sigma_1)^3}\phi^2\right) - (1-\alpha)(1 + \frac{\phi}{M^2 - 3\sigma_2} + \frac{3}{2}\frac{M^2 + \sigma_2}{(M^2 - 3\sigma_2)^3}\phi^2) \tag{7.46}$$

Eq. (7.46) can be written as,

$$\frac{\partial^2\phi}{\partial\xi^2} = X\phi + Y\phi^2 = -\frac{\partial V(\phi)}{\partial\phi} \tag{7.47}$$

with $X = (1 - \frac{\alpha\mu}{M^2 - 3\mu\sigma_1} - \frac{1-\alpha}{M^2 - 3\sigma_2})$

and $Y = [\frac{1}{2} - \frac{3}{2}\frac{\alpha\mu^2(M^2 + \mu\sigma_1)}{(M^2 - 3\mu\sigma_1)^3} - \frac{3}{2}\frac{(1-\alpha)(M^2 + \sigma_2)}{(M^2 - 3\sigma_2)^3}]$

Now, multiplying Eq. (7.47) by $\frac{\partial\phi}{\partial\xi}$ and integrating we get

$$\frac{1}{2}(\frac{\partial \phi}{\partial \xi})^2 = \frac{X}{2}\phi^2 + \frac{Y}{3}\phi^3 = -V(\phi) \tag{7.48}$$

This is the energy equation for quasi particle with Sagdeev potential $V(\phi)$. In order to have the solitary wave solution the pseudo potential has to satisfy the following equations [18],

$$V(0) = \frac{\partial V(0)}{\partial \phi} = 0, \frac{\partial^2 V}{\partial \phi^2} < 0 \tag{7.49a}$$

$$V(\phi_0) = 0 \text{ for some } \phi_0 \tag{7.49b}$$

$$V(\phi)\langle 0 \text{ for } 0\langle|\phi|\langle|\phi_0| \tag{7.49c}$$

where $|\phi_0|$ is the amplitude of soliton.

Using the boundary condition $V(\phi)\big|_{\phi=\phi_0} = 0$, we find,

$$V(\phi)\big|_{\phi=\phi_0} = \frac{Y}{3}\phi_0\phi^2(1 - \frac{\phi}{\phi_0}) = 0 \tag{7.50}$$

With $\phi = \phi_0 \sec h^2\left(\sqrt{\frac{-Y}{24}\phi_0}\right)\xi$ (7.51)

Using the boundary condition used in Eq. (7.49) the minimum value of Mach number is obtained and we find,

$$M_{\min} = \sqrt{(\frac{3(\sigma_2 + \mu\sigma_1) + \alpha\mu + (1-\alpha)}{4} + \sqrt{\frac{3\mu(3\sigma_1\sigma_2 + \sigma_1 + \alpha(\sigma_2 - \sigma_1)}{4}})} +$$

$$\sqrt{(\frac{3(\sigma_2 + \mu\sigma_1) + \alpha\mu + (1-\alpha)}{4} - \sqrt{\frac{3\mu(3\sigma_1\sigma_2 + \sigma_1 + \alpha(\sigma_2 - \sigma_1)}{4}})} \tag{7.52}$$

As expected, the minimum value of Mach number is a function of both σ_i and α. For one component plasma the Eq. (7.52) reduces to the familiar condition $M\rangle\sqrt{1+3\sigma}$ obtained by

Ghosh et *al* [17]. It would be also interesting to find out the upper limit of Mach numbers. An attempt is made to find out the maximum allowed values of Mach number as a function of α and σ_i. Sagdeev [19] had previously shown the upper limit of M (<1.6) for such solitary wave in the cold ion plasma. In our present investigation with the inclusion of finite ion temperature and a much wider range of α , we could obtain solitary wave with much larger Mach numbers. In order to find out the maximum allowed values of the Mach number as a function of α and σ_i, we deduce an analytical condition by equating maximum value of ϕ with the ions kinetic energy ($\frac{(M-\sqrt{3\mu\sigma_1})^2}{2\mu}$) in such plasma. This condition is similar to that of the Sagdeevs condition for cold ions (i,e; $\frac{1}{2}M^2=\phi_0$) [19]. Further imposing the requirement that value of V at $\phi_0=\frac{(M-\sqrt{3\mu\sigma_1})^2}{2\mu}$ is greater than or equal to zero, we have obtained the allowed values of Mach number by solving the following equation;

$$(1-\frac{\alpha\mu}{M^2-3\mu\sigma_1}-\frac{1-\alpha}{M^2-3\sigma_2})\frac{\phi^2}{2}+(\frac{1}{2}-\frac{3}{2}\frac{\alpha\mu^2(M^2+\mu\sigma_1)}{(M^2-3\mu\sigma_1)^3}-\frac{3}{2}\frac{(1-\alpha)(M^2+\sigma_2)}{(M^2-3\sigma_2)^3})\frac{\phi^3}{3}=0 \qquad (7.53)$$

7.3 Numerical results and discussions

7.3.1 Parametric Variation

From the Eq. (7.51) it is observed that soliton solution exists only when $Y<0$. As the definition of Y includes the parameters α, σ_1 and σ_2, thus these parameters will determine the existence of the solitary wave at a fixed value of μ (= 13.34) in such plasma. It has been reported in the literature that adding small amount of light ion impurity in the argon

discharge is sufficient enough to prevent the formation of soliton while introduction of argon in the light ion plasma affects the formation of soliton much less [8]. Introduction of hydrogen in the argon plasma increases the value of α . **Fig. 7.2(a)** shows the Sagdeev pseudo potential for different α at a fixed value of Mach number and ion temperature while **Fig. 7.2(b)** shows the variation of amplitude of soliton as a function of α for different set of values of (σ_1, σ_2) .

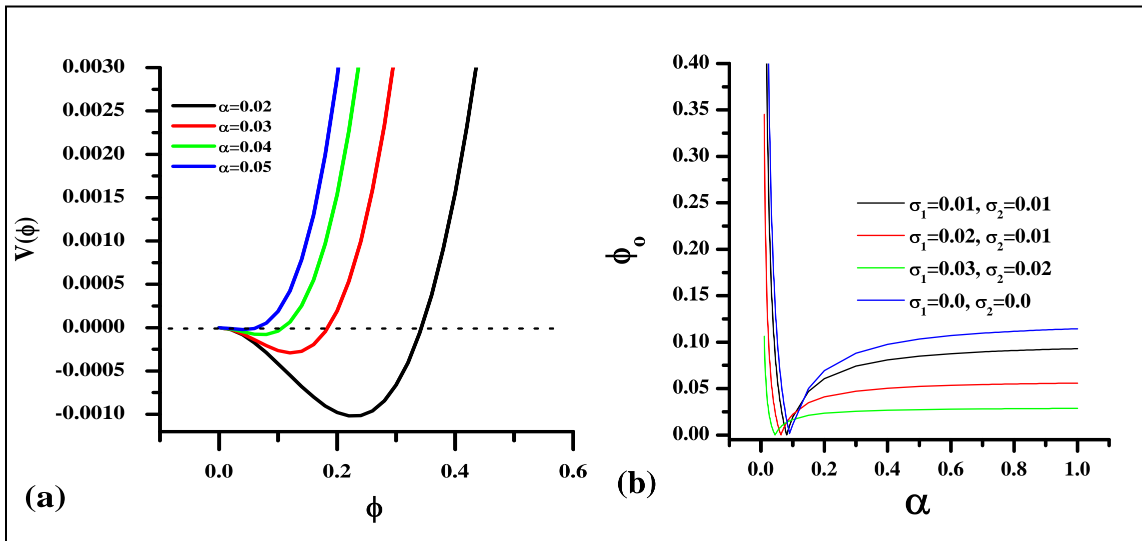

Figure 7.2 (a)The effect of α on the Sagdeev potential curves for σ_1 = 0.02, σ_2 = 0.01. Mach number is fixed at M= 1.5. (b) Variation of solitons amplitude with α for different set of values of σ_i .

The striking feature is the abrupt reduction of the solitons amplitude due to small concentration of light ion. At this stage, one would have thought that further addition of light ion inhibits solitary wave solution. But, since it is reported in the literature that solitary wave solution exists for higher value of α [8] we continued increasing α further. It is discovered that after reaching a minimum value (8.34×10^{-2} per cent of maximum amplitude for cold ion plasma with $\sigma_i = 0$), the amplitude of the soliton further increases

slightly with increasing α . This trend is found to be consistent for different set of values for (σ_1, σ_2) . It is also clear from the **Fig. 7.2(b)** that with the increase in σ_i the minimum value of amplitude is reached at comparatively lower value of α .

Fig. 7.3 shows the pseudo potential curves for different set of values (σ_1, σ_2) . It is reasonable to assume higher value of ion temperature for lighter ions (σ_1) than the heavier ions (σ_2) under the same sorts of plasma conditions. The depth of the pseudo potential curve represents the amplitude of soliton. It is seen that the general effect of ion temperature is to reduce the amplitude of soliton for a fixed value of the Mach number (M) and the parameter α . It is due to the fact that with increase of ion temperature, the non-linearity increases or alternatively dispersive effect decreases that results a decrease of solitons amplitude [20]. For cold ions ($\sigma_i = 0$) the largest amplitude is obtained and increasing the set of values (σ_1, σ_2) we observe that the amplitude of the solitary wave decreases. It gives us indication that there exists an upper bound for σ_i at fixed values of M and α beyond which the solitary wave solution is not possible. From Eq. (7.47), the condition can be written $M^2 \rangle 3\mu\sigma_1$. The observation regarding the **Fig. 7.3** shows that increase in ion temperature values gradually inhibits an otherwise stable cold ion solitary wave. In the next step, we propose a procedure to determine the type of ion temperature that can play a decisive role for the formation of soliton. In this procedure, keeping $\sigma_2 (= 0.01)$ constant, the effect of variation of σ_1 from (0.01 to 0.06) on the amplitude of soliton is first studied. It is then followed by the similar variation of σ_2 from (0.01 to 0.06) keeping $\sigma_1 (= 0.06)$ constant.

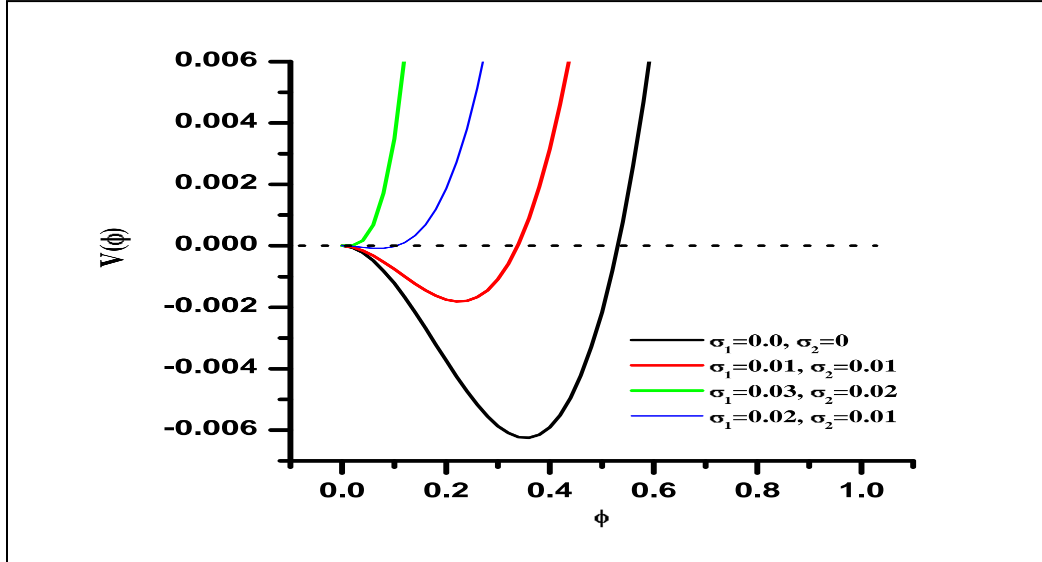

Figure 7.3 The effect of σ_i on the Sagdeev potential curves for α = 0.02, Mach number (M) =1.5.

It is noticed (**Fig.7.4**) that the variation of σ_1 decreases the amplitude more sharply than the corresponding variation of σ_2. Similar pattern of variation of ϕ_0 with σ has been reported by many researchers [17, 21]. It shows that the role of lighter ions is more significant on the formation of soliton. In this study, we have used the value of Mach number for parametric variation above the minimum value obtained by solving Eq. (7.52). It would be interesting to find out the upper limit of Mach numbers. An attempt is made to find out the maximum allowed values of Mach number as a function of α and σ_i. Sagdeev [19] had previously shown the upper limit of M (<1.6) for such solitary wave in the cold ion plasma. In our present investigation with inclusion of finite ion temperature and a much wider range of α, we could obtain solitary wave with much larger Mach numbers. The maximum allowed values of Mach number as a function of α and σ_i are found following the procedure as already mentioned in the section 7.2.

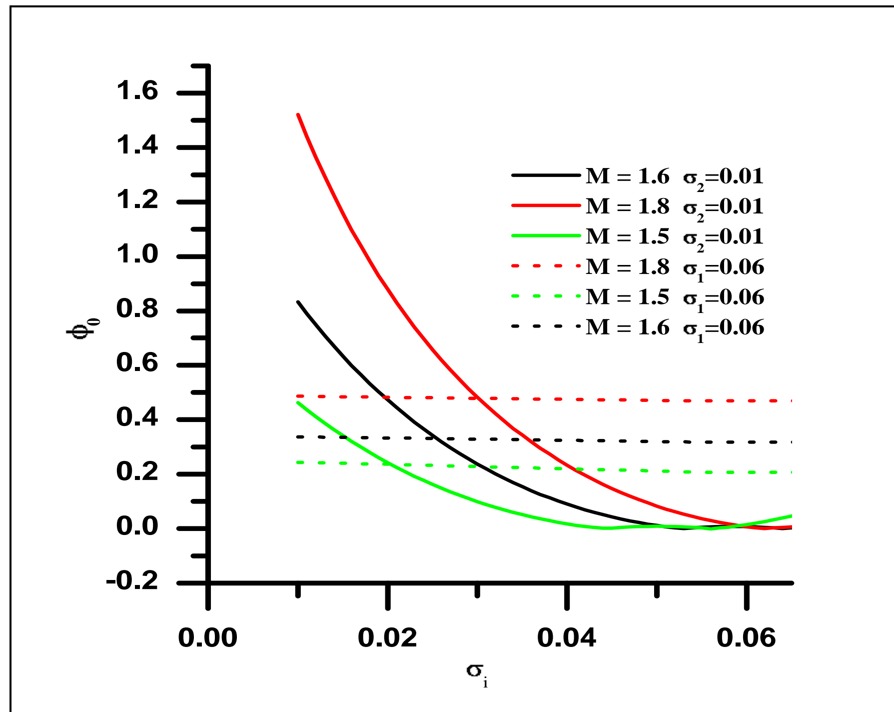

Figure 7.4 Variation of solitons amplitude with σ_i at different values of Mach number. The Mach number is varied from 1.5 to 1.8. For each Mach number in one set σ_1 is varied keeping $\sigma_2 = 0.01$ constant and in another set σ_2 is varied keeping $\sigma_1 = 0.06$ constant.

The **Fig. 7.5** shows the variation of maximum and minimum values of Mach number as a function of α at fixed values of σ_i. It is clear from the figure that the Mach number of solitons increases with increasing value of α .The observed trend of increasing soliton velocity with α is due to the fact that with introduction of hydrogen in the argon discharge, the density of electron decreases. This leads to the decrease of electrons resistance to the positive ion momentum and as such, the phase velocity increases leading to a gradual increase of Mach number [22]**.** Also, an increase of Mach number with σ_i can be easily noted from the **Fig. 7.5**.

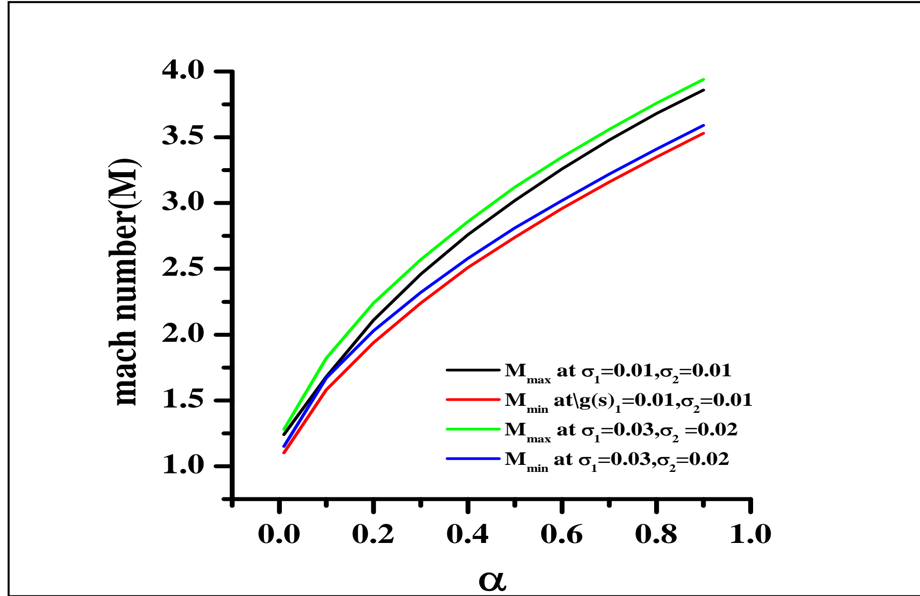

Figure 7.5 The variation of maximum and minimum values of Mach number as a function of α at different set of values for σ_i.

7.3.2 Width variation and potential profile

Using the eq. (7.51) the typical hill shaped potential profile is obtained for ion acoustic solitary wave in the **Fig. 7.6(a)** and **Fig. 7.6(b)**. It represents that with low α, it follows almost a hill shaped structure but changes to a rather flat toped profile with increase in α. Similar change in slope of the potential profile with increasing σ_i can be seen. The change in the potential pattern signifies the variation in the width of solitary wave as a function of the mentioned parameters. For small amplitude soliton, comparing Eq. (7.51) with the standard equation of the form,

$$\phi = \phi_0 \sec h^2\left(\frac{\xi}{W}\right) \qquad (7.54)$$

where W is the width of the soliton. In the realm of present investigation W can be written as $W = \sqrt{\frac{-24}{Y\phi_o}}$. **Fig. 7.7** represents the variation of W with α at different set of values for σ.

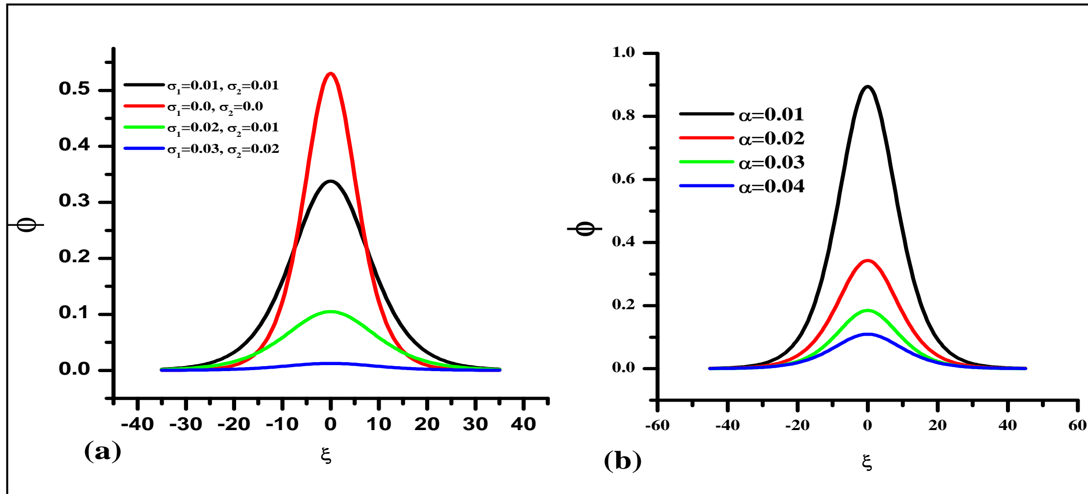

Figure 7.6(a) Influence of σ_i on the potential profiles of solitary wave solution. Here, M =1.5 and α = 0.02. (b) Influence of α on the potential profiles for solitary solution. Here M = 1.5 and σ_1 = 0.02, σ_2 = 0.01.

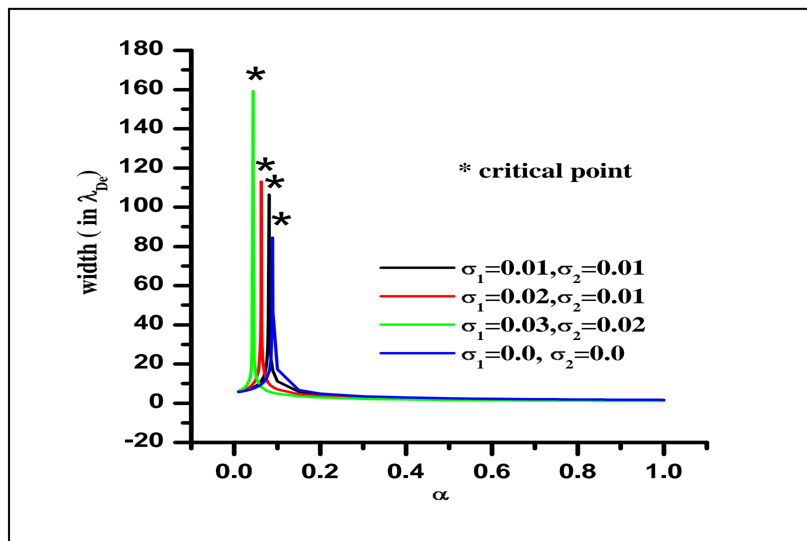

Figure 7.7 Variation of solitons width with α .The parameter considered here is σ_i .

It is seen that the width of soliton increases with α initially, reaches the maximum abruptly at critical values and then decreases slowly with further increase in it. The critical point is shifted towards the lower value of α (0.09 to 0.04) with gradual increase in the set of values for σ_i. Comparing it with the **Fig. 7.2(b)**, it is observed that with increasing α the variation of width of soliton is opposite to that of the amplitude variation. The definitive characteristic of soliton [7] is thus established in present investigation.

7.4 Conclusion

In this chapter we have presented the properties of soliton for a wide range of parameters in the hydrogen additive argon plasma. It enables us to explain qualitatively some of the experimental results of soliton in such plasma. It is observed that introduction of hydrogen in the argon plasma reduces the amplitude of soliton abruptly to a minimum and shows a tendency of slight increase with further addition of hydrogen. Inclusion of the ion temperature seemed to reduce the amplitude of soliton. Also it is found that increasing the set of values for (σ_1, σ_2) reduces the critical value of α. Our analysis also shows that the lighter ions play the dominant role in the reduction of amplitude and such as, the formation of solitary wave. From the Sagdeev pseudo potential method, we obtained the analytical condition for the maximum and minimum values of Mach numbers (M) for soliton. This reduces exactly to the Sagdeevs condition for cold ion plasma. The maximum and minimum values of Mach number are found to increase with the hydrogen enrichment in the discharge. Solitary waves with large Mach numbers (M>1.6) are obtained. However, the inverse relation of solitons width and amplitude is found to be consistent within the entire range of α and σ_i values considered.

References

[1] D. J. Kortweg and G. de Vries, Philos. Mag. **39**, 433 (1895).

[2] N. J. Zabusky and M. D. Kruskal, Phys. Rev. Lett. **15**, 240 (1965).

[3] H. Washimi and T. Taniuti, Phys. Rev. Lett. **17**, 996 (1966).

[4] N. J. Zabusky and M. D. Kruskal Phys. Rev. Lett. **15,** 240 (1965).

[5] H. Ikezi, R. J. Taylor, and D. R. Baker, Phys. Rev. Lett. **25**, 11 (1970).

[6] K. B. Gylfason, J. Alami, U. Helmersson and J. T. Gudmundsson, J. Phys. D: Appl. Phys. **38,** 3417 (2005).

[7] S. K. Sharma, K. Devi, N. C. Adhikari and H. Bailung, Phys. Plasmas. **15,** 082111 (2008).

[8] M. Q. Tran, Phys. Scripta **20,** 317 (1979).

[9] W. D. Jones, A. Lee, S. N. Gleeman, and H. J. Doucet, Phys. Rev. Lett. **35**, 1349 (1975).

[10] B. N. Goswami and B. Buti, Phys. Lett. A **57**, 149 (1976).

[11] B. Buti, Phys. Lett. A **76**, 251 (1980).

[12] K. Nishihara and M. Tajiri, J. Phys. Soc. Jpn. **50**, 4047 (1981).

[13] A. Bogaerts, and R. Gijbels, Spectrochimica. Acta Part B **57,** 1071(2002).

[14] R. F. G. Meulenbroeks, A. J. van Beek, A. J. G. van Helvoort, M. C. M. van de Sanden, and D. C. Schram, Phys. Rev. E **49**, 4397 (1994).

[15] R. S. Mason, P. D. Miller, and I. P. Mortimer, Phys. Rev. E **55**, 7462 (1997).

[16] N. Hershkowitz and Y-C. Ghim, Plasma Sources Sci. Technol. **18** (2009) 014018.

[17] S. S. Ghosh, K. K. Ghosh, and A. N. Sekar Iyengar, Phys. Plasmas. **3**, 3939 (1996).

[18] H. H. Kuehl and K. Imen, IEEE Trans. Plasma Sci. **PS-13**, 37 (1985).

[19] R. Z. Sagdeev, in *Reviews of Plasma Physics*, edited by M. A. Leontovich Consultants Bureau, New York, 1966), Vol. 4, p. 23.

[20] S. G. Tagare, Plasma Physics, **15,** 1247 (1973).

[21] S. Baboolal, R. Bharuthram, and M. A. Hellberg, J. Plasma Phys. **44**, 1 (1990).

[22] J. L. Cooney, D. W. Aossey, J. E. William, M. T. Gavin, H. S. Kim, Y. C. Hsu, A. Scheller, and K. E. Lonngremi, Plasma Sources Sci. Technol. **2**, 73 (1993).

CHAPTER 8

Summary and Future Scope

Summary of the present investigation has been presented in this chapter. In DC planar magnetron sputtering a planar material target is used as the cathode of the system while argon is used as the sputtering gas. Molecular gases like nitrogen and oxygen are used as the reactive gases and presence of hydrogen is always beneficial for quality thin film growth. The study on DC planar magnetron glow discharge plasma was aimed to understand the modulation of plasma parameters as a function of deposition conditions as it is very important to optimize the growth of the deposited thin film. Also, a search for novel plasma diagnostic was one of the motivations of the ongoing work. In this respect, the thesis presented the following important results that can throw lights in the field of reactive sputtering.

8.1 Summary of Investigation

The general criterion necessary for the deposition of thin films by magnetron sputtering such as the necessary base pressure, required pumping speed to attain the base pressure, gas flow rates to maintain the operating pressure were achieved. In reactive sputtering due to the addition of the molecular gases to the sputtering gas (argon), the process becomes complex and non-linear that involves many interdependent parameters. The complex discharge behavior of the molecular gases believes to play an important role during evaluation of plasma parameters in such discharge. The plasma parameters were measured near the substrate plane (at a distance of 10 mm above the substrate) using the Langmuir probe. The light collecting system of the optical emission spectrometer (LCSF) was focused in the substrate vicinity. As the working pressure and input power are two most important parameters for optimization of quality deposition, both of them were addressed in this thesis work. Working pressure was varied by adding reactive gases

such as Nitrogen (N_2), Oxygen (O_2) and Hydrogen (H_2) to the sputtering gas (Ar). The addition of molecular gas showed the decreasing trend of electron and ion density at a fixed value of sputtering gas partial pressure. The trend of density modulation is explained on the basis of the various chemical reactions that takes place in the magnetron discharge plasma with various reaction coefficients. In hydrogen added argon plasma the advent of 'hydrogen-like' ions creates additional loss channels for electrons and ions. On the other hand, in oxygen added argon plasma owing to the presence of volume created negative oxygen ions, a decreasing trend of electron and positive ion density as a function of oxygen addition was noticed. The recombination reactions of nitrogen like ions were found to determine the fate of electron and ion density in nitrogen added argon plasma. The variation of input power at a fixed working pressure was done to achieve the I-V characteristics of the target in DC planar magnetron. The steepness of the square root of the discharge current against voltage plot qualitatively indicates the impedance and therefore, the density of the plasma and it followed the trends of density modulation evaluated by the Langmuir probe and Optical Emission Spectroscopy. Deposition rate measurement for hydrogen added argon plasma and nitrogen added argon plasma revealed the important results that the decreasing ion and electron density tends to reduce the sputter yield of the magnetron, resulting a gradual decrease in deposition rate.

The effect of magnetron target on the bulk plasma properties in the substrate vicinity region was obvious from the higher value of electron and ion density as well as the degree of ionization of Chromium (Cr) target than that of Copper (Cu) target. The plasma parameters for Cr and Cu target differ because the ion induced secondary coefficient of Cr was more than that of Cu.

In the material aspect of the investigation, the observed plasma parameters of the nitrogen added argon plasma were correlated with the preferred orientation (structural growth) of the titanium

nitride (TiN) thin films. Lesser degree of ion bombardment at higher working pressure conditions favors the growth of more open planes of poly crystalline TiN film such as the TiN(200) and TiN(220). Other than the plasma parameters, the substrate also influenced the growth of TiN thin films. The substrate induced effects were observed during the growth of TiN on pre-plasma nitrided substrate: a treatment known as duplex process that aimed the commercial viability of the Physical Vapor Deposition process. The similarity of the inter-atomic spacing of TiN(200) plane with γ'-Fe_4N(111) plane of plasma nitrided substrate was found to be the factor responsible for preferential growth along (200) plane.

In the search for accurate plasma diagnostic, oxygen added argon plasma was probed by exciting ion acoustic wave in the substrate vicinity of the magnetron. This technique of wave excitation is known as tone burst technique and the measurement of relative density of negative oxygen ion (O^-) was done in such a discharge. The higher value of reactive rate coefficient of the dissociative attachment of oxygen molecule (main production channel for O^- ion) compared to that of O^- ion recombination reaction (chief O^- loss channel) was found to be a factor responsible for gradual increase of O^- density as a function of oxygen addition. Also, electron and Ar^+ ion density scales inversely with oxygen addition and this factor also favors the enhancement of O^- ions. The obtained value of relative negative ion density was compared with the values of the Langmuir probe diagnostics and both of the techniques show good agreement.

It is worthwhile to mention that in the experiment of probing magnetron discharge plasma with ion acoustic wave, it was noticed that while propagating through plasma, the IAW was transformed into ion acoustic soliton. But inclusion of light ion impurity such as hydrogen-like ions tends to inhibit its formation. A detailed theoretical investigation of this phenomenon revealed the important result that inclusion of warm light ion impurity increases the non-linearity

or alternatively decreases the dispersive effects that results a decrease in solitons width. The maximum and minimum values of the Mach numbers of the soliton were found to increase with hydrogen addition. However, the inverse relation between the solitons width and amplitude was found to be consistent.

Thus, the investigation has achieved its aim that was to investigate the parameters in the magnetron plasma which was necessary to optimize the quality deposition and established iona acoustic wave as a novel diagnostic of the plasma.

8.2 FUTURE SCOPE

The present investigation opens up a few important aspects of magnetron discharge which could be continued as future investigation.

1. The variation of working pressure and input power was considered in this investigation. As the reactive sputtering involves many independent parameters such as the substrate biasing, magnetic field of the magnetron, substrate temperature, the impact of these parameters on the plasma properties could be attempted for future investigation.

2. The ion acoustic wave seems to be a very efficient diagnostic tool for magnetron discharge. The relative density of positive ions in hydrogen and nitrogen added argon plasma using IAW could be incorporated in the future investigation.

3. The texture coefficient measured for the coatings of TiN was found to dependent on the plasma parameters. In the reactive sputtering of titanium target using oxygen as reactive gas, the variation of relative oxygen negative ion concentration with oxygen partial pressure could be correlated with the texture growth of the deposited titanium di-oxide (TiO_2) coatings. The control over the growth of TiO_2 could open up versatile industrial application.

4. The electron energy distribution function (EEDF) obtained from the Langmuir probe is bi Maxwellian in nature, characterized by the presence of two distinct energetic electron groups in magnetron discharge plasma. The effect of the bi Maxellian electrons on the propagation of the ion acoustic wave could be further investigated.

5. The existing planar magnetron set up offers opportunities to expand the study further to other materials and coatings.